Cell

Characterizing and targeting glioblastoma neuron-tumor networks with retrograde tracing

Graphical abstract

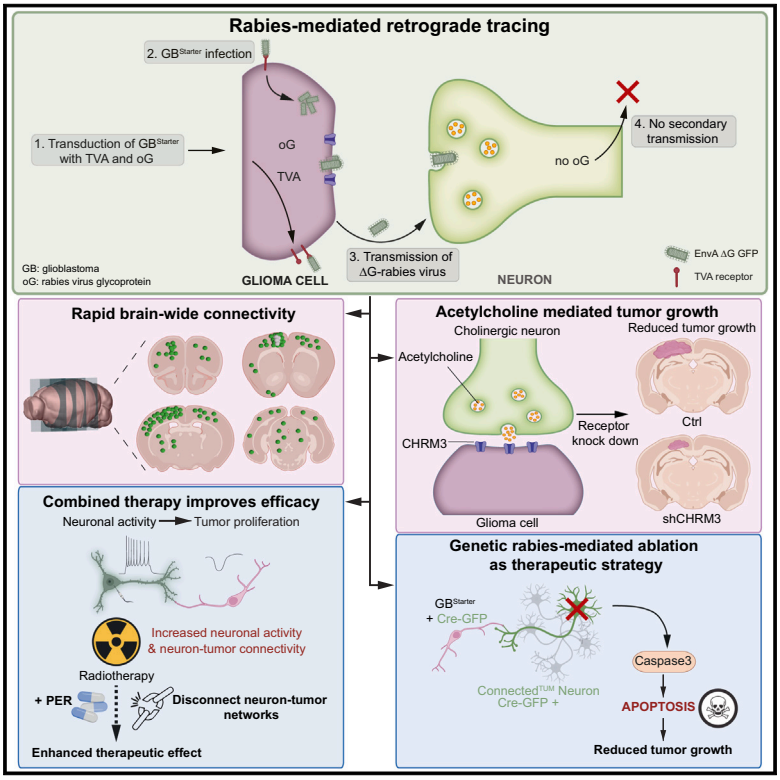

Highlights

- Rabies-based retrograde tracing maps brain-wide neuronal connectome of glioblastoma
- Rapid neuronal integration of glioblastoma precedes neuronal dysfunction
- Radiotherapy and perampanel show additive effects by disrupting neuron-tumor networks
- Rabies-mediated genetic ablation of neurons halts glioblastoma progression

Authors

Svenja K. Tetzlaff, Ekin Reyhan, Nikolas Layer, ..., Franz L. Ricklefs, Dieter Henrik Heiland, Varun Venkataramani

Correspondence

varun.venkataramani@med.uni-heidelberg.de

In brief

Rapid integration of glioblastoma into neuronal circuits promotes glioblastoma invasion and growth, as shown by rabies-based retrograde tracing. Targeting of neuron-tumor networks with pharmacological or rabies-mediated disconnection offers therapeutic potential.

Tetzlaff et al., 2025, Cell *188*, 390–411
January 23, 2025
https://doi.org/10.1016/j.cell.2024.11.002

CellPress

CellPress
OPEN ACCESS

Cell

Article

Characterizing and targeting glioblastoma neuron-tumor networks with retrograde tracing

Svenja K. Tetzlaff,[1,2,3,29] Ekin Reyhan,[1,2,29] Nikolas Layer,[1] C. Peter Bengtson,[4] Alina Heuer,[1] Julian Schroers,[1,5] Anton J. Faymonville,[1] Atefeh Pourkhalili Langeroudi,[1] Nina Drewa,[1] Elijah Keifert,[1] Julia Wagner,[1,3] Stella J. Soyka,[1,3] Marc C. Schubert,[1,3] Nirosan Sivapalan,[1] Rangel L. Pramatarov,[1,3] Verena Buchert,[1] Tim Wageringel,[1] Elena Grabis,[6,7] Niklas Wißmann,[1,3] Obada T. Alhalabi,[8] Michael Botz,[1,3] Jovana Bojcevski,[9] Joaquín Campos,[10] Berin Boztepe,[11,12]

(Author list continued on next page)

[1]Neurology Clinic and National Center for Tumor Diseases, University Hospital Heidelberg, Heidelberg, Germany
[2]Clinical Cooperation Unit Neurooncology, German Cancer Consortium (DKTK), German Cancer Research Center (DKFZ), Heidelberg, Germany
[3]Department of Functional Neuroanatomy, Institute for Anatomy and Cell Biology, Heidelberg University, Heidelberg, Germany
[4]Department of Neurobiology, Interdisciplinary Centre for Neurosciences (IZN), Heidelberg University, Heidelberg, Germany
[5]Division of Radiology, German Cancer Research Center (DKFZ), Heidelberg, Germany
[6]Translational Neurosurgery, Friedrich-Alexander University Erlangen Nuremberg, Erlangen, Germany
[7]Department of Neurosurgery, Medical Center – University of Freiburg, Freiburg, Germany
[8]Department of Neurosurgery, Heidelberg University Hospital, Heidelberg, Germany
[9]Clinical Cooperation Unit Translational Radiation Oncology, German Cancer Research Center (DKFZ), Heidelberg, Germany

(Affiliations continued on next page)

SUMMARY

Glioblastomas are invasive brain tumors with high therapeutic resistance. Neuron-to-glioma synapses have been shown to promote glioblastoma progression. However, a characterization of tumor-connected neurons has been hampered by a lack of technologies. Here, we adapted retrograde tracing using rabies viruses to investigate and manipulate neuron-tumor networks. Glioblastoma rapidly integrated into neural circuits across the brain, engaging in widespread functional communication, with cholinergic neurons driving glioblastoma invasion. We uncovered patient-specific and tumor-cell-state-dependent differences in synaptogenic gene expression associated with neuron-tumor connectivity and subsequent invasiveness. Importantly, radiotherapy enhanced neuron-tumor connectivity by increased neuronal activity. In turn, simultaneous neuronal activity inhibition and radiotherapy showed increased therapeutic effects, indicative of a role for neuron-to-glioma synapses in contributing to therapeutic resistance. Lastly, rabies-mediated genetic ablation of tumor-connected neurons halted glioblastoma progression, offering a viral strategy to tackle glioblastoma. Together, this study provides a framework to comprehensively characterize neuron-tumor networks and target glioblastoma.

INTRODUCTION

Glioblastoma, the most prevalent primary brain cancer in adults, presents a formidable challenge in neuro-oncology.[1,2] Effective treatments remain elusive, largely due to cellular heterogeneity, the invasive nature of glioblastoma, and resistance to standard-of-care therapies, including surgery, radiotherapy, and chemotherapy.[1,3–11] A burgeoning area of interest is the exploration of the intricate relationships between glioblastoma cells and neural networks of the brain.[12–15] The interplay between tumor cells and neuronal circuits, particularly synaptic neuron-tumor communication, has emerged as a critical factor in tumor progression and invasion.[12,16–25] Although neuronal molecular signatures have been described in paired primary and recurrent glioblastoma,[4,7] it is unclear whether and how neuron-glioma synaptic communication contributes to therapeutic resistance. Synaptic inputs onto adult glioblastoma cells have so far been identified as local, glutamatergic projections, leaving the circuit architecture interacting with glioma largely unexplored.[8,16–18] Moreover, the dynamics of how tumor cells synaptically integrate into neuronal networks and, in turn, change neuronal structure and function are yet unclear. The cellular, molecular, and functional heterogeneity of glioblastoma has been increasingly investigated,[5,8–10,26] but how these layers relate to neuronal connectivity is yet unknown.

Although tracing neuronal circuits is an important field of research in neuroscience,[27–29] the neuronal connectome of brain tumors remains poorly understood.[12,13] Among tracing approaches, retrograde monosynaptic tracing using modified rabies virus stands out as a pivotal technique for investigating

CellPress
OPEN ACCESS

Jonas G. Scheck,[9,11] Sascha Henry Conic,[13,14] Maria C. Puschhof,[15] Giulia Villa,[6] Richard Drexler,[16] Yahya Zghaibeh,[17] Fabian Hausmann,[18,19] Sonja Hänzelmann,[18,19,20] Matthia A. Karreman,[2] Felix T. Kurz,[5,21] Manuel Schröter,[22] Marc Thier,[1,13,14] Abigail K. Suwala,[23,24] Karin Forsberg-Nilsson,[25] Claudio Acuna,[10] Julio Saez-Rodriguez,[15] Amir Abdollahi,[9] Felix Sahm,[23,24] Michael O. Breckwoldt,[11,12] Bogdana Suchorska,[8] Franz L. Ricklefs,[17] Dieter Henrik Heiland,[6,7,26,27,28] and Varun Venkataramani[1,2,3,30,*]

[10]Chica and Heinz Schaller Foundation, Institute of Anatomy and Cell Biology, Heidelberg University, Heidelberg, Germany
[11]Neuroradiology Department, University Hospital Heidelberg, Heidelberg, Germany
[12]Clinical Cooperation Unit Neuroimmunology and Brain Tumor Immunology, German Cancer Consortium (DKTK), German Cancer Research Center (DKFZ), Heidelberg, Germany
[13]Division of Stem Cells and Cancer, German Cancer Research Center (DKFZ) and DKFZ-ZMBH Alliance, Heidelberg, Germany
[14]Heidelberg Institute for Stem Cell Technology and Experimental Medicine (HI-STEM gGmbH), Heidelberg, Germany
[15]Faculty of Medicine, Heidelberg University, and Institute for Computational Biomedicine, Heidelberg University Hospital, Heidelberg, Germany
[16]Department of Neurology and Neurological Sciences, Stanford University, Stanford, CA, USA
[17]Department of Neurosurgery, University Medical Center Hamburg-Eppendorf, Hamburg, Germany
[18]Center for Biomedical AI, University Medical Center Hamburg-Eppendorf, Hamburg, Germany
[19]Institute of Medical Systems Biology, University Medical Center Hamburg-Eppendorf, Hamburg, Germany
[20]Department of Medicine, University Medical Center Hamburg-Eppendorf, Hamburg, Germany
[21]Division of Neuroradiology, University Hospital Geneva, Geneva, Switzerland
[22]ETH Zurich, Department of Biosystems Science and Engineering, Basel, Switzerland
[23]Department of Neuropathology, University Hospital Heidelberg, Heidelberg, Germany
[24]Clinical Cooperation Unit Neuropathology (B300), German Cancer Consortium (DKTK), German Cancer Research Center (DKFZ), Heidelberg, Germany
[25]Department of Immunology, Genetics and Pathology, Science for Life Laboratory, Uppsala University, 75185 Uppsala, Sweden
[26]Department of Neurosurgery, University Hospital Erlangen, Friedrich-Alexander University Erlangen Nuremberg, Erlangen, Germany
[27]Department of Neurological Surgery, Northwestern University Feinberg School of Medicine, Chicago, IL, USA
[28]German Cancer Consortium (DKTK), partner site Freiburg, Freiburg, Germany
[29]These authors contributed equally
[30]Lead contact
*Correspondence: varun.venkataramani@med.uni-heidelberg.de
https://doi.org/10.1016/j.cell.2024.11.002

neural network connectivity.[30–33] Previous studies have applied this methodology to neurons and oligodendrocyte precursor cells, both receiving synaptic input[34,35] to map their neuronal connectome.[33,36–44]

This paper introduces a modified rabies-virus-based retrograde tracing methodology platform for the multimodal, neuronal connectome characterization of glioblastoma, applicable across model systems. This approach revealed that the majority of glioblastoma cells and neurons in certain patient-derived models were functionally connected in early glioblastoma colonization, contrasting previous data from us and others,[16,17] where technologies to comprehensively assess functional connectivity were lacking. Molecular and functional analyses of tumor-connected (connected^{TUM}) and tumor-unconnected (unconnected^{TUM}) neurons did not show significant differences in early stages of colonization, implying that synaptic integration of tumor cells into neural circuits precedes neuronal dysfunction and hyperexcitability, described in later stages of the disease.[45–49] Moreover, we found brain-wide recruitment of diverse neuronal populations, including neuromodulatory circuits forming neuron-tumor networks. Both cholinergic and glutamatergic neurons were able to drive glioblastoma progression. Further, invasive patient-derived tumors and glioblastoma cell states were associated with synaptogenic gene expression signatures and subsequent larger neuron-tumor connectivity. Radiotherapy in the presence of glioblastoma promoted neuron-tumor connectivity by boosting neuronal activity, and combined neuronal activity inhibition and radiotherapy showed an increased therapeutic effect, providing evidence for the role of neuron-to-glioma synaptic communication in therapeutic resistance. Lastly, we provided proof-of-concept data of how modified rabies viruses could be used to selectively ablate connected^{TUM} neurons and thereby inhibit glioblastoma progression.

These insights offer a valuable framework, highlighting the pivotal role of characterizing the neuronal connectome of glioblastoma to develop advanced therapeutic strategies.

RESULTS

Rabies-based retrograde tracing enables versatile neuron-tumor network characterization

We took advantage of a rabies-virus-based retrograde tracing system for characterizing neuron-tumor networks using patient-derived glioblastoma spheroid cultures (Figure 1A).[8,9,50,51] First, we stably transduced glioblastoma spheroids (n = 14 patient-derived models; Figure 1B; Table S1) with a lentivirus containing the EnvA receptor TVA (cellular receptor for subgroup A avian leukosis viruses) for rabies entry, the rabies virus glycoprotein (oG) for trans-complementation as well as spread, and the cytosolically expressed fluorophore mCherry (STAR Methods). Second, we performed fluorescence-activated cell sorting (FACS) for mCherry to isolate glioblastoma cells expressing TVA and oG. Subsequently, these cells were transduced with two EnvA-pseudotyped G-protein-deleted (ΔG) rabies virus strains[31,33] expressing cytosolic GFP that could only infect glioblastoma cells containing the TVA receptor. Upon entry and trans-complementation with the rabies-oG protein, starter

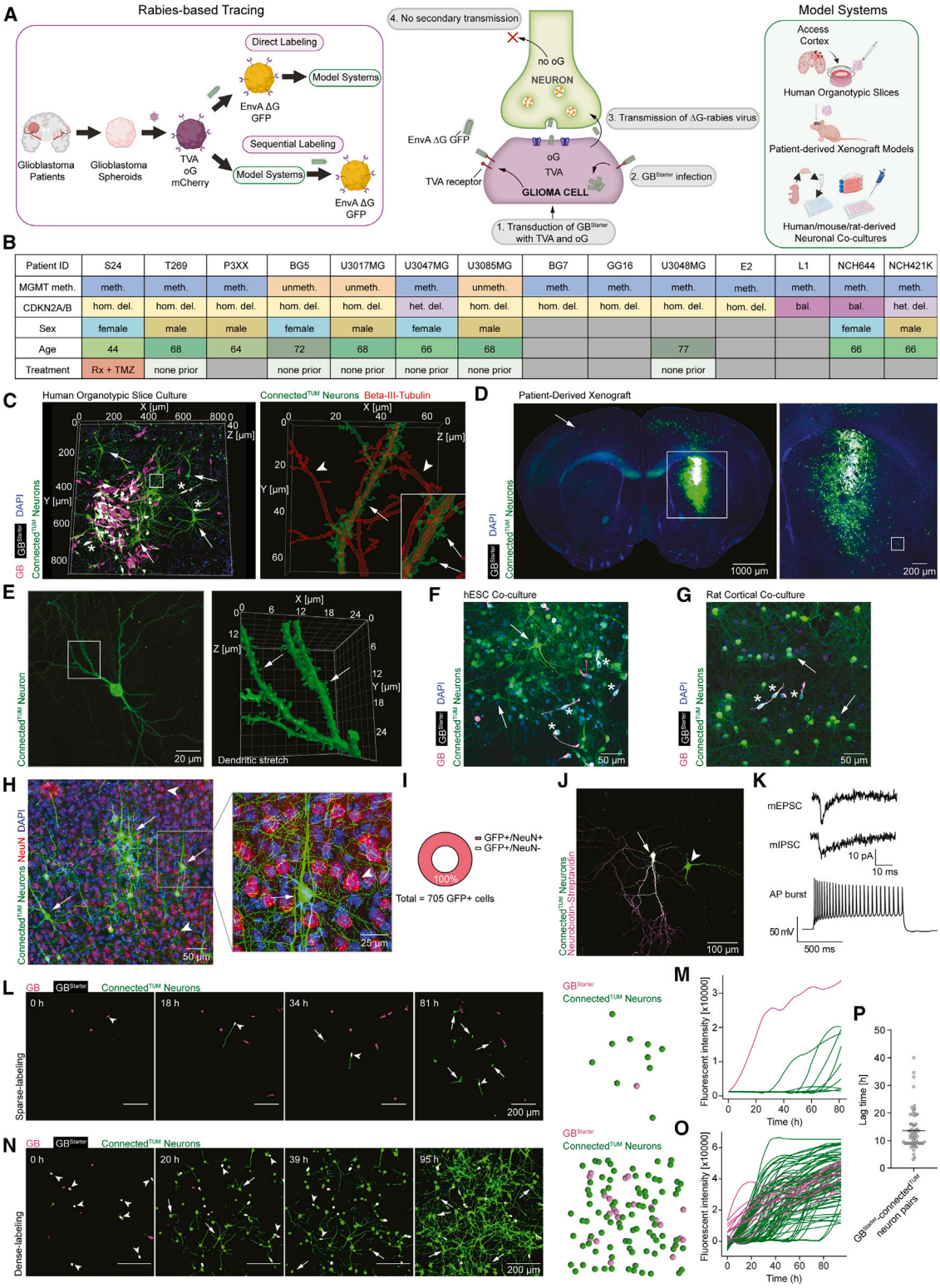

Patient ID	S24	T269	P3XX	BG5	U3017MG	U3047MG	U3085MG	BG7	GG16	U3048MG	E2	L1	NCH644	NCH421K
MGMT meth.	meth.	meth.	meth.	unmeth.	unmeth.	meth.	unmeth.	meth.	meth.	meth.	meth.	meth.	meth.	meth.
CDKN2A/B	hom. del.	hom. del.	hom. del.	hom. del.	hom. del.	het. del.	hom. del.	hom. del.	hom. del.	hom. del.	hom. del.	bal.	bal.	het. del.
Sex	female	male	male	female	male	female	male						female	male
Age	44	68	64	72	68	66	68			77			66	66
Treatment	Rx + TMZ	none prior		none prior	none prior	none prior	none prior			none prior				

Figure 1. Rabies-based tracing of glioblastoma neuron-tumor networks across model systems

(A) Retrograde tracing workflow in patient-derived glioblastoma (GB) models.

(B) Overview of patient-derived GB models used in this study. Meth., methylated; unmeth., unmethylated; hom. del., homozygous deletion; het. del., heterozygous deletion; bal., balanced; Rx + TMZ, radiotherapy + temozolomide.

(legend continued on next page)

glioblastoma cells (GB^{Starter}) are expected to label tumor-connected (connected^{TUM}) neurons via monosynaptic, retrograde propagation.[31] Connected^{TUM} neurons could be identified by expressing GFP, whereas patient-derived GB^{Starter} cells expressed both mCherry and GFP. Further, as connected^{TUM} neurons did not express oG, no further transmission was possible, ensuring a high specificity of this approach to label directly connected neuron-tumor networks (Figure 1A).

FACS of GB^{Starter} spheroids enabled a direct, dense labeling of all tumor cells before engrafting these tumor cells. In contrast, implanting or seeding glioblastoma cells before (ΔG) rabies virus transduction with a titration of the ΔG rabies virus led to sequential, sparse labeling to trace the neuronal connectome of single glioblastoma cells (STAR Methods). Further, genetic modification of the rabies virus expressing functional proteins such as the Cre recombinase[52] enabled a precise manipulation of connected^{TUM} neurons to investigate its effect on glioblastoma biology (Figures 1A and S1A).

We assessed this approach across model systems. To establish an all-in-human tissue model system, we adapted an organotypic slice culture using human access cortex tissue removed during surgery[53] (n = 9 patients; Figure 1C) and transplanted GB^{Starter} cells to label human connected^{TUM} neurons. This model system was complemented by patient-derived xenograft (PDX) and neuronal co-culture models (Figures 1C–1I, S1B, S1C, and S1E–S1H; STAR Methods).[54]

Specifically, retrograde tracing in the presence of GB^{Starter} cells selectively labeled connected^{TUM} neurons across all patient-derived model systems (Figures 1C–1G).

This approach allowed ultrastructural characterization of connected^{TUM} neurons, including different classes of dendritic spines,[55] employing high- and super-resolution light microscopy (Figures 1C, 1E, and S1D). Importantly, connected^{TUM} neurons maintained their characteristic electrophysiological properties (Figures 1J, 1K, and S1I). Importantly, this technology was specific, as close to no labeling occurred when labeling with lysed GB^{Starter} cells in co-cultures or PDX models nor when media from neuron-GB^{Starter} co-cultures was added to neuronal cultures (Figures S1J–S1L).

Last, we evaluated the toxicity of two strains of rabies virus, CVS-N2c$^{\Delta G}$-eGFP(EnvA) and SAD-B19$^{\Delta G}$-eGFP(EnvA).[30,33] Further, we did not observe increased cell death in rabies-infected tumor or neuronal cells in our observation period (Figures S1M–S1O; Table S1).

Rapid and dynamic integration of glioblastoma into neuron-tumor networks

Live-cell imaging in PDX and co-culture models over time revealed the fast and dynamically increasing neuronal integration of glioblastoma cells. Sparse labeling of GB^{Starter} cells enabled tracking their individual recruitment of connected^{TUM} neurons in near real time, with neuronal connectivity increasing over time (Figures 1L and 1M; Video S1). Employing dense labeling to mark the entire tumor permits a comprehensive examination of the whole neuronal connectome (Figures 1N and 1O; Video S1). Remarkably, connected^{TUM} neuronal labeling occurred within hours after GB^{Starter} cells became GFP-positive in co-cultures (Figures 1P and S1P; STAR Methods) and between 1 and 3 days in PDX models (Figure S1Q), demonstrating the rapid formation of neuron-tumor connections. These findings were complemented by neuronal-activity-driven excitatory postsynaptic currents and slow inward currents (SICs), demonstrating functional connections between neurons and glioblastoma cells after a brief interaction period (Figure S1R).[8,16–18]

Widespread functional neuron-tumor network communication in glioblastoma

Unexpectedly, in certain patient-derived models in early glioblastoma colonization, the majority of tumor cell clusters labeled

(C) 3D rendering of human organotypic slice injected with S24 GB^{Starter} cells (left, white, asterisks), connected^{TUM} neurons (CVS-N2c$^{\Delta G}$-eGFP(EnvA), green, arrows). Inset (right): beta-III-tubulin (red) expressing connected^{TUM} neuron, only beta-III-tubulin expressing, unconnected^{TUM} neurons (arrowheads). Zoom-in: dendritic spines of connected^{TUM} neuron (arrows).
(D) Retrograde tracing in a PDX model. Exemplary brain section with S24 GB^{Starter} cells (white) and connected^{TUM} neurons (SAD-B19$^{\Delta G}$-eGFP(EnvA), green). Distant, contralateral connected^{TUM} neurons (arrow). Inset: zoom-in on tumor site (dashed white circle).
(E) Exemplary connected^{TUM} neuron from the brain slice from (D) (left). 3D rendering of dendritic stretches (right) with visible dendritic spines (arrows).
(F) Retrograde tracing in co-culture of human embryonic stem cell-induced neurons with human S24 GB^{Starter} cells (white, asterisks). Connected^{TUM} neurons (CVS-N2c$^{\Delta G}$-eGFP(EnvA), green, arrows).
(G) As in (F) but in co-culture of rat cortical neurons.
(H) Confocal imaging of connected^{TUM} neurons (CVS-N2c$^{\Delta G}$-eGFP(EnvA), green) in S24 PDX stained with neuronal marker NeuN (red). Connected^{TUM} neurons (arrows), only NeuN-positive, unconnected^{TUM} neurons (arrowheads).
(I) Portion of NeuN-positive cells among connected^{TUM} neurons (n = 705 eGFP-positive cells in co-cultures of n = 10 patient-derived GB models).
(J) Confocal imaging of a patched connected^{TUM} neuron (CVS-N2c$^{\Delta G}$-eGFP(EnvA), green) with neurobiotin filling and streptavidin 647 staining (white, arrow). Non-filled connected^{TUM} neuron (arrowhead).
(K) Representative examples of mEPSC (top), mIPSC (middle), and AP bursts after current injection (bottom) of a connected^{TUM} neuron.
(L) Probability maps (PMs) of time-lapse imaging demonstrating sparse labeling. S24 GB cells (magenta), a GB^{Starter} cell (white, arrowheads), and connected^{TUM} neurons (CVS-N2c$^{\Delta G}$-eGFP(EnvA), green, arrows). Rendered manual segmentation representing the last imaging time point (far right). Each dot: one cell.
(M) Line plot indicating the change of (CVS-N2c$^{\Delta G}$)-eGFP fluorescence intensities of the GB^{Starter} cell (magenta) and its connected^{TUM} neurons (green) as shown in (L).
(N) As in (L) but showing dense labeling.
(O) As in (M) but as shown in (N).
(P) Lag time with which (SAD-B19$^{\Delta G}$/CVS-N2c$^{\Delta G}$)-eGFP fluorescence is observed in connected^{TUM} neurons after rabies-infection of their respective GB^{Starter} cells (n = 65 GB^{Starter}-connected^{TUM} neuron pairs).
See also Figure S1, Table S1, and Video S1.

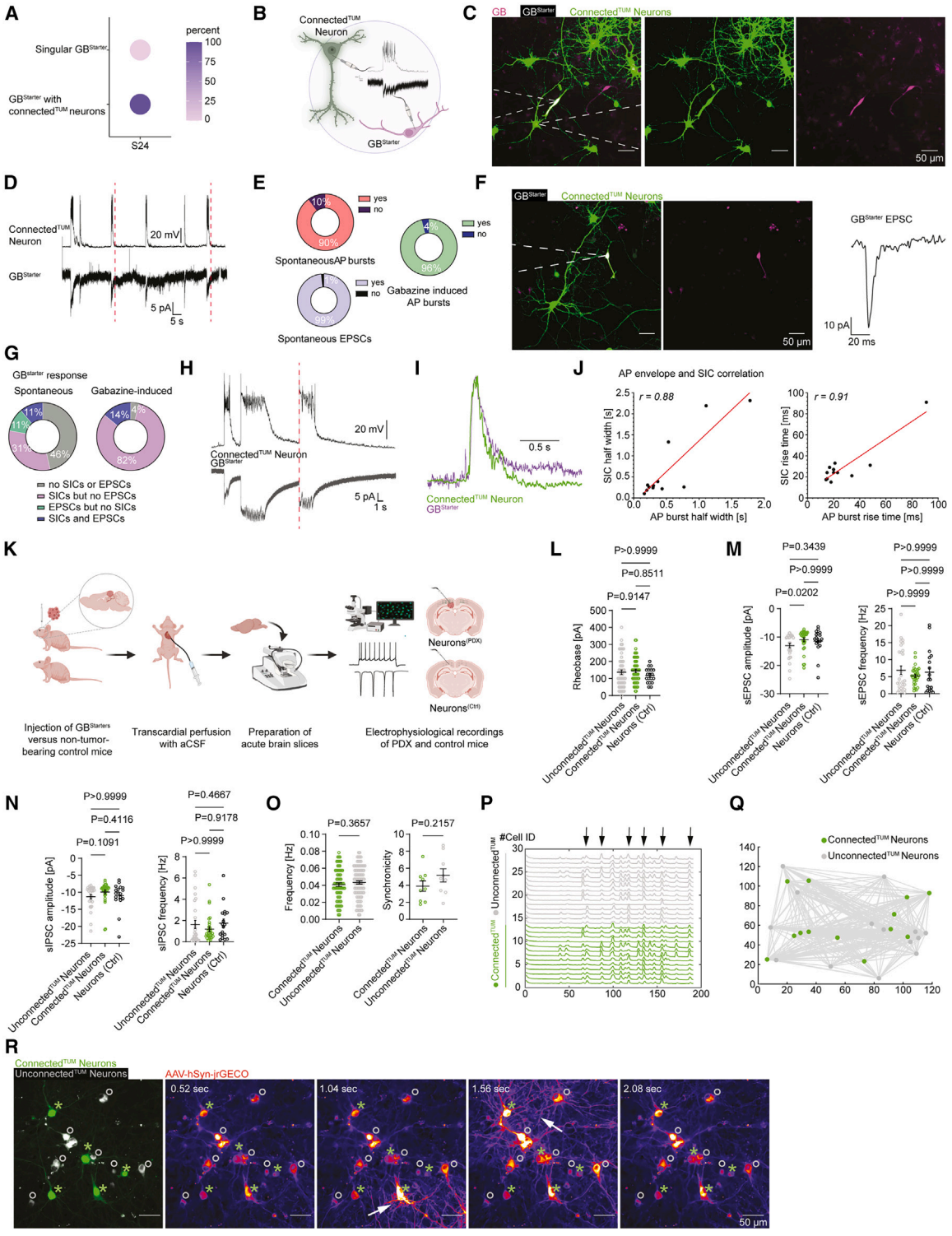

Figure 2. Functional investigation of neuron-tumor networks

(A) GB^{Starter} cell connectivity in co-cultures (n = 2,529 GB^{Starter} cells in 10 samples).

(B) Schematic of paired whole-cell patch-clamp electrophysiology of connected^{TUM} neurons and GB^{Starter} cells.

(C) Representative image of a S24 GB^{Starter} cell (white) and connected^{TUM} neurons (CVS-N2c$^{\Delta G}$-eGFP(EnvA), green) in co-culture. Dashed white lines: patch pipettes.

(D) Exemplary electrophysiological traces of a connected^{TUM} neuron (top) and its respective S24 GB^{Starter} cell (bottom). Red dashed lines: synchronized events.

(legend continued on next page)

connected^{TUM} neurons, indicating a high level of structural neuron-tumor connectivity (Figure 2A).

We performed paired whole-cell patch-clamp electrophysiology of putatively connected^{TUM} neurons and glioblastoma cells in co-culture (Figure 2B) to examine their functional connectivity (Figures 2C–2E). Action potentials of connected^{TUM} neurons correlated with either excitatory postsynaptic currents (EPSCs) or SICs in glioma cells (Figures 2F and 2G),[16,17] indicating functional connectivity between connected^{TUM} neurons and their corresponding GB^{Starter} cells.

Interestingly, the GABA receptor inhibitor gabazine triggered epileptiform activity of connected^{TUM} neurons in co-cultures with GB^{Starter} cells, revealing that a significant proportion of tumor cells (exceeding 96%) engaged in functional neuron-tumor networks in this patient-derived model (Figure 2G). Characterizing functional connectivity within these networks may require strong stimulation as in the case of neuronal hyperexcitability, occurring in later disease stages of glioblastoma[13,14,56] and highlighting the complex relationship between structural connectivity and functional communication. We also found a strong correlation in neuronal action potential burst slopes of connected^{TUM} neurons and the GB^{Starter} response as SIC half width, rise time, and decay time, indicating a sensitive functional connection (Figures 2H–2J and S2A).

Neuron-tumor network formation precedes neuronal dysfunction

We wanted to understand whether this neuron-tumor connectivity influences neuronal function. We found no differences between connected^{TUM} and unconnected^{TUM} neurons in their electrophysiological properties in *ex vivo* PDX and co-culture models. We found only minor differences in neurons of tumor-bearing mice compared with those of non-tumor-bearing mice (Figures 2K and S2B–S2E; Table S1; STAR Methods). Our analysis did not reveal variations in action potential firing patterns or neuronal excitability in both PDX models and co-cultures at very early stages of glioblastoma colonization (Figures 2L and S2F–S2M; Table S1; STAR Methods). In addition, multielectrode array recordings in neuronal cultures with tumor cells showed similar action potential burst rates and firing rates and did not differ in their synchronicity to neuronal cultures without tumor (Figures S2N and S2O). There was little difference in synaptic connectivity between connected^{TUM} and unconnected^{TUM} neurons or control neurons from non-tumor-bearing mice, demonstrated by the analysis of miniature or spontaneous excitatory (mEPSC/sEPSC) or inhibitory (mIPSC/sIPSC) postsynaptic currents (Figures 2M, 2N, and S3A–S3F; Table S1; STAR Methods). Functional calcium imaging demonstrated that connected^{TUM} and unconnected^{TUM} neurons exhibited similar somatic calcium transient frequencies and synchronicity (Figure 2O). Both neuronal populations showed co-active calcium transient patterns (Figures 2P–2R; Video S2). This observation expands the concept of the neuron-tumor connectome, suggesting that connected^{TUM} neurons maintain their integration within broader neural circuits.

Influence of neuron-tumor connectivity on neuronal plasticity and behavior

To investigate whether neuronal plasticity of connected^{TUM} neurons is affected by neuron-tumor networks, we employed intravital longitudinal multiphoton microscopy of PDX models to examine dendritic spine dynamics. Interestingly, we found dynamics comparable to physiological dendritic plasticity as previously described (Figures 3A and 3B; Video S3).[57–60]

Importantly, no difference in dendritic spine density or morphologies between connected^{TUM} and unconnected^{TUM} neurons could be observed across patient-derived models (Figures 3C and S4A–S4D).

Complementing this functional investigation, we performed spatial transcriptomics of purely human organotypic slices and single-cell RNA sequencing of co-cultures, where we investigated the distribution of connected^{TUM} and unconnected^{TUM} neuronal subpopulations (Figures 3D–3G and S4E–S4H; STAR Methods). This approach identified a consistent ratio of

(E) Spontaneous AP bursts (top left, $n = 59$ cells), spontaneous EPSCs (bottom left, $n = 59$ cells), and gabazine-induced AP bursts (right, $n = 25$ cells) of connected^{TUM} neurons.
(F) Representative image of patched S24 GB^{Starter} cell (white, CVS-N2c$^{\Delta G}$-eGFP(EnvA)) and corresponding EPSC trace. Dashed white lines: patch pipette.
(G) Electrophysiological GB^{Starter} response as no response, only EPSCs, only SICs, or both, under baseline condition (left, $n = 63$ pairs) and after stimulation with gabazine (right, $n = 28$ pairs).
(H) Representative traces of paired-patched connected^{TUM} neuron (top) and GB^{Starter} cell (bottom) showing neuronal AP bursts and responsive SICs. Red dashed line: synchronized traces.
(I) Exemplary overlay of AP burst slope and GB^{Starter} SIC.
(J) Correlation of AP envelopes and SICs. SIC half width and AP burst half width (left), $n = 12$ pairs, Pearson's r = 0.88, ANOVA F (df) = 33.8 (11), $p = 0.0017$. SIC rise time and AP burst rise time (right), Pearson's r = 0.91, ANOVA F (df) = 49.8 (11), $p = 0.00035$.
(K) Schematic workflow for comparing electrophysiological properties of neurons in tumor-bearing (connected^{TUM} and unconnected^{TUM} neurons) and control mice.
(L) Neuronal rheobase in patched neurons from PDX and control mice ($n = 55$ unconnected^{TUM}, 53 connected^{TUM}, 19 control neurons, Kruskal-Wallis test).
(M) sEPSC amplitude and frequency in neurons from PDX and control mice ($n = 28$ unconnected^{TUM}, 31 connected^{TUM}, 18 control neurons, Kruskal-Wallis test).
(N) As in (M) but for sIPSCs ($n = 28$ unconnected^{TUM}, 31 connected^{TUM}, and 18 control neurons, Kruskal-Wallis test).
(O) Calcium transient frequency and synchronicity of connected^{TUM} and unconnected^{TUM} neurons ($n = 75$ connected^{TUM} and 95 unconnected^{TUM} neurons in 9 fields of view [FoVs], Mann-Whitney test [frequency] and unpaired t test [synchronicity]).
(P) Representative individual calcium traces of connected^{TUM} and unconnected^{TUM} neurons. Exemplary synchronized events (arrows).
(Q) Exemplary connected^{TUM} and unconnected^{TUM} calcium coactivity map.
(R) Dual-color calcium imaging of unconnected^{TUM} (gray, circles) and connected^{TUM} (CVS-N2c$^{\Delta G}$-eGFP(EnvA), green, asterisks) neurons using AAV-hSyn-jrGECO (fire) in co-culture.
See also Figures S2 and S3, Table S1, and Video S2.

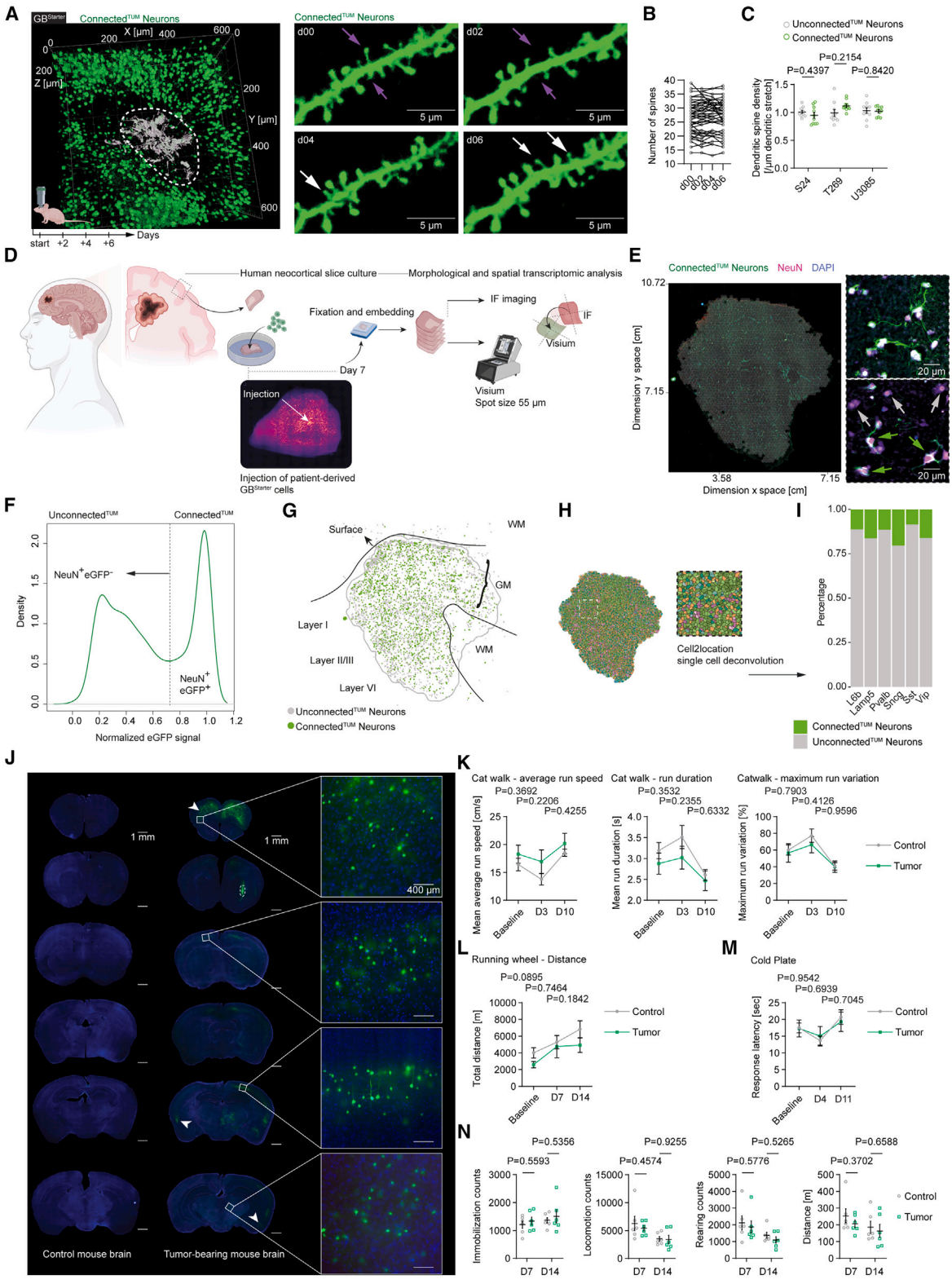

(legend on next page)

connected^{TUM} to unconnected^{TUM} neurons across all neuronal clusters, suggesting a widespread integration of tumor cells within neural networks irrespective of neuronal subpopulation (Figures 3H and 3I).

In agreement with clinical data showing first neurological deficits occurring at substantial MRI-positive tumor volumes,[63] we did not observe behavioral deficits related to developing glioblastoma at early stages (Figures 3J–3N and S4I–S4L; Video S3; STAR Methods).

Neuron-tumor connectivity is patient- and cell-state-dependent

As patient-specific and tumor-cell-state-driven heterogeneity is one hallmark of glioblastoma,[5,7,8] we investigated tumor-intrinsic mechanisms driving neuron-tumor connectivity. We integrated analyses of neuron-tumor connectivity via retrograde tracing, histological tumor growth patterns of PDX, and single-cell RNA sequencing data from glioblastoma patients and PDX models to examine the functional connectivity of these models.

To assess the capacity of cells from different patient-derived models to form synaptic networks, we used genes associated with the Gene Ontology (GO) term for synaptogenesis[64,65] to calculate a synaptogenic module score on single-cell RNA sequencing data (STAR Methods). Additionally, we used a single-cell RNA sequencing-based invasivity score associated with invasive growth across glioblastoma patients and patient-derived models (Figures 4A and 4B).[8] Interestingly, models with a high synaptogenic score also showed a high invasivity score (Figures 4C and 4D).[8] In line with these data, patient-derived models with high synaptogenic and invasivity scores showed a significantly higher mean somatokinetic speed than ones with a lower synaptogenic and invasivity scores (Figures 4E and 4F). Tumor models with a higher propensity for invasion also exhibited greater neuronal connectivity. We determined the average number of connected^{TUM} neurons per GB^{Starter} cell, referred to as the input-to-starter ratio. The highly invasive patient-derived models S24 and BG7 showed a higher mean input-to-starter ratio than the less-invasive patient-derived model P3XX (Figures 4G, 4H, and S5A–S5C). The invasion speed and input-to-starter ratios across 12 patient-derived models were positively correlated in highly connected patient-derived models (Figure 4I). Furthermore, the distance distribution of connected^{TUM} neurons to GB^{Starter} cells was significantly higher in invasive patient-derived models (Figures S5D and S5E), suggesting a broader connectivity across larger distances. Patient-dependent differences could further be seen in the percentage of single glioblastoma cells receiving neuronal input per model (Figure S5F). Additionally, the invasivity score[8] correlated with a recently described epigenetic neural signature of glioblastoma indicative of synaptic connectivity[61] (Figures S5G–S5K). The invasivity score, similar to the epigenetic neural score,[61] was associated with worse survival in a glioblastoma patient cohort (Figures S5L and S5M).

These results raised the question how much invasive and stationary glioblastoma cell states receive synaptic input. Combining live-cell imaging and retrograde tracing, we observed that invasive tumor microregions showed higher neuron-tumor connectivity (Figures 4J–4L). In line with this, a significantly higher invasivity and synaptogenic score in the tumor rim was seen as compared with the core within each patient, also matching the correlation of the invasivity and synaptogenic scores per patient (Figures 4M, 4N, and S5N).

Further, we observed new infections occurring around invading GB^{Starter} cells that may label connected^{TUM} neurons *en passant* via transient synaptic contacts (Figure 4O; Video S4).

These findings collectively underscore the association between a tumor cell's synaptogenic potential at the RNA expression level with neuron-tumor connectivity and its invasiveness.

Figure 3. Neuronal plasticity and behavioral effects of neuron-to-tumor networks

(A) 3D rendering of longitudinal *in vivo* two-photon microscopy (IV2PM) of S24 GB^{Starter} cells (white) and connected^{TUM} neurons (CVS-N2c$^{\Delta G}$-eGFP(EnvA), green). Tumor overview (left), main tumor mass (dashed white circle). IV2PM time-lapse of a dendritic stretch over 6 days (right). New spines (white arrows), retracted spines (purple arrows).

(B) Dendritic turnover in connected^{TUM} neurons *in vivo* (n = 1,352 dendritic spines over time in n = 3 mice).

(C) Dendritic spine density of connected^{TUM} and unconnected^{TUM} neurons in PDX models S24, T269, and U3085 (n = 10 FoVs per condition per model, multiple t tests).

(D) Workflow of spatial transcriptomics in retrogradely traced human organotypic slices injected with a patient-derived GB model.

(E) Aligned immunostaining and spatial transcriptomics dataset. Overview of one analyzed section (left). Spatial transcriptomics spots as overlay (opacity = 10%). Zoom-ins (right) with connected^{TUM} neurons (green arrows) and unconnected^{TUM} neurons (gray arrows).

(F) (CVS-N2c$^{\Delta G}$)-eGFP signal in analyzed neurons. Connected^{TUM} and unconnected^{TUM} neurons segmented based on eGFP signal.

(G) 2D surface plot depicting the spatial distribution of connected^{TUM} and unconnected^{TUM} neurons, showing no defined spatial pattern (spatial autocorrelation Moran's I, p = 0.243).

(H) Cellular phenotype exploration by Cell2location deconvolution using the extended GBMap reference dataset[61,62] to explore distinct cellular phenotypes of connected^{TUM} versus unconnected^{TUM} neurons.

(I) Distribution of connected^{TUM} and unconnected^{TUM} neurons across neuronal subclasses. 15%–20% of each neuronal subclass consists of connected^{TUM} neurons, no significant enrichment in any subclass was observed (ANOVA, $p > 0.05$).

(J) Representative brain sections of S24 PDX tumor-bearing mice (middle) and control mice (left). Tumor area (dashed white circle), distant connected^{TUM} neurons (CVS-N2c$^{\Delta G}$-eGFP(EnvA), green, arrowheads). Zoom-ins on marked regions of interest (right).

(K) Average run speed, run duration, and maximum run variation of tumor versus control mice (n = 6 mice each, two-way ANOVA with post hoc Tukey test).

(L) Total distance in a voluntary wheel running test over 24 h of tumor versus control mice (n = 6 mice each, two-way ANOVA with post hoc Tukey test).

(M) Response latency of tumor versus control mice when exposed to a 2°C cold plate (n = 6 mice each, two-way ANOVA with post hoc Tukey test).

(N) Counts for immobilization, locomotion, rearing, and distance in meters as observed in a laboratory animal behavior observation registration and analysis system (LABORAS) cage over 24 h in tumor versus control mice (n = 6 mice each, two-way ANOVA with Fisher's least significant difference [LSD] test).

See also Figure S4 and Video S3.

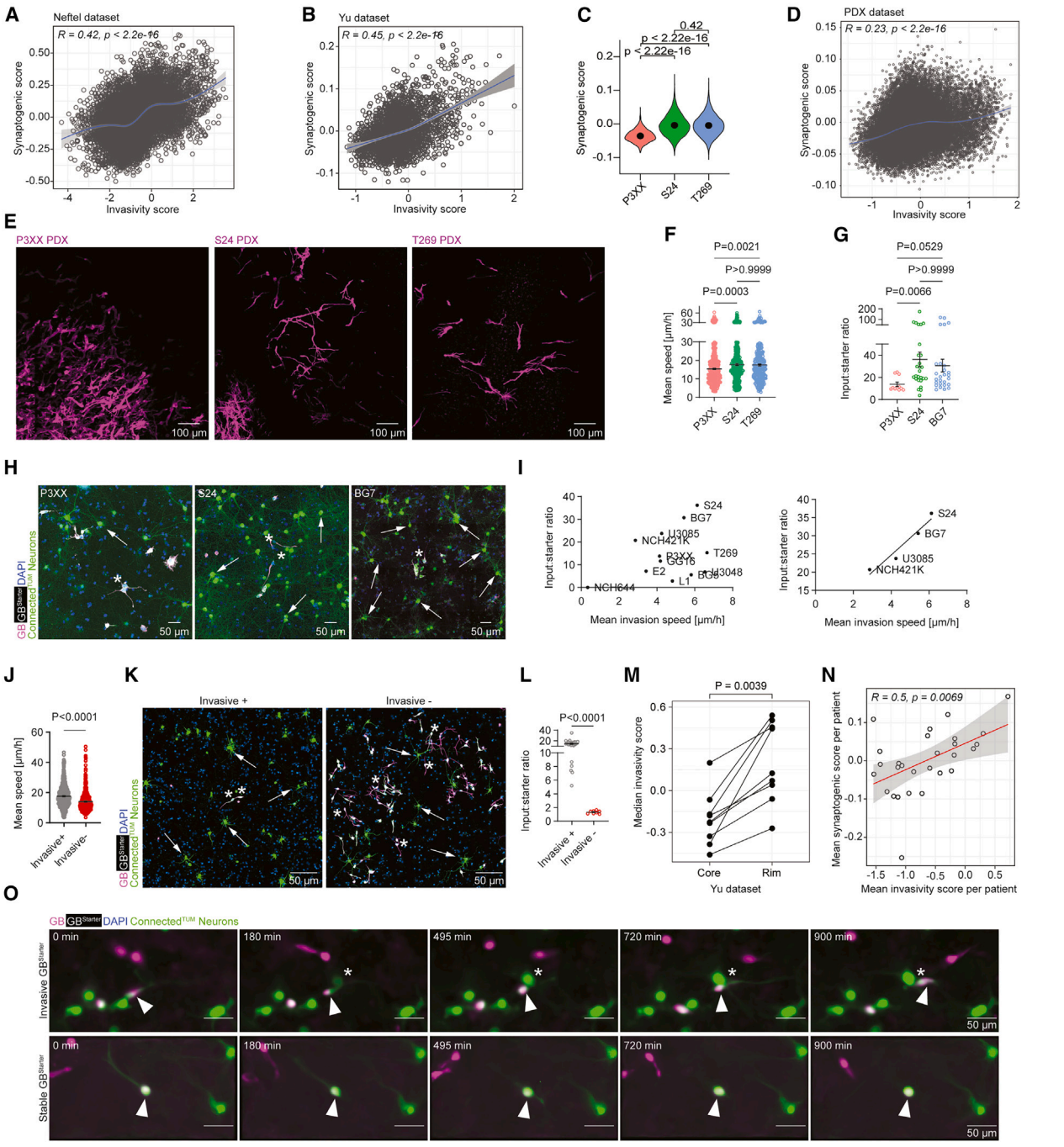

Figure 4. Influences of patient- and cell-state-specific factors on neuron-tumor connectivity

(A) Correlation of synaptogenic and invasivity score in Neftel dataset[5] (n = 7,929 cells, Pearson's test).

(B) As in (A) but in Yu dataset[66] (n = 2,795 cells, Pearson's test).

(C) Synaptogenic score compared in PDX models P3XX, S24, and T269 (n = 27,293 cells, Wilcoxon test).

(D) As in (A) but in PDX models P3XX, S24, and T269 (n = 27,293 cells, Pearson's test).

(E) IV2PM of three PDX models (P3XX [left], S24 [middle], and T269 [right]) showing the invasive tumor front. Post processed with denoise.ai.

(F) Mean somatokinetic speed of three patient-derived models in co-culture (n = 392 [P3XX], n = 435 [S24], n = 332 [T269] cells, Kruskal-Wallis test).

(G) Input-to-starter ratio comparison of three patient-derived models in co-culture (n = 27 [S24], n = 11 [P3XX], n = 27 [BG7] samples, Kruskal-Wallis test).

(H) Retrograde tracing in patient-derived models P3XX (left), S24 (middle), and BG7 (right). $GB^{Starter}$ cells (white, asterisks), $connected^{TUM}$ neurons (CVS-N2c$^{\Delta G}$-eGFP(EnvA), green, arrows).

(legend continued on next page)

Brain-wide recruitment of neuronal circuits by glioblastoma

To examine the role of brain-tumor-bearing regions on the formation of neuron-tumor networks,[25] we implanted patient-derived GB^{Starter} cells into the cortex and striatum of mice, both brain regions that are affected in glioblastoma patients.[67] Investigation of PDX models at early stages of glioblastoma colonization (Figure S6A) revealed long-range projections throughout the brain, including the contralateral hemisphere,[25] as well as proximal connected^{TUM} neurons (Figure S6B). In line with previous data,[8] neuronal activity of glutamatergic neurons drove glioblastoma invasion when optogenetically stimulating neurons in the proximity of tumor-bearing regions (Figures S6C and S6D).

Long-range projections could be delineated both in PDX and co-culture models (Figures S6E–S6G). Specifically, cortical tumors exhibited more dispersed connectivity throughout the brain than striatal tumors (Figures 5A–5C and S6F). Although cortical glioblastoma showed 50% of distal-connected^{TUM} neurons (defined here as neuronal somata more than 1 mm away from the nearest GB^{Starter} cell), striatal tumors had 33% on average. Overall, approximately 9% and 14% of connected^{TUM} neurons were contralateral in PDX of cortical and striatal tumors, respectively, highlighting the role of long-range neuron-tumor networks contributing to the glioblastoma connectome (Table S1).

The proportion of distal neuron-tumor connections significantly increased over time, indicating a more dispersed brain-wide recruitment of neuronal circuits as the tumor progresses (Figures 5D–5F and S6H). The distribution of connected^{TUM} neuronal subtypes remained stable over time in PDX models, indicating a homogeneous increase in neuron-to-tumor connectivity in early glioblastoma infiltration, with most connected^{TUM} neurons being glutamatergic and GABAergic (Figures S6I and S6J).

Both cortical and striatal tumors primarily received neuronal input from the cortex, basal ganglia, and thalamus (Figure 5H).[42,68–71] Although cortical tumors received input mainly from the ipsilateral and contralateral isocortex, striatal tumors received most neuronal input from the basal ganglia, reflecting strong regional neuronal connectivity.[42,68–70,72] Despite early-stage glioblastoma forming wide-ranging connections to distant primary cortical somatosensory and motor areas, mouse behavior was not affected (Figures 3J–3N, S4I–S4L, and S6K–S6M). The brainstem was recruited as a pathophysiologically important region (Figure S6N).[73] Although the degree of neuron-tumor connectivity varied between tumor-bearing regions, the overall pattern of brain-wide distribution was comparable between cortical and striatal brain tumors. This illustrates the conserved recruitment from glioblastoma of neural circuits (Figures 5I and S6O).

To investigate the capacity of glioblastoma to communicate with different neuronal subpopulations, we compared co-cultures with GB^{Starter} cells and neurons from the hippocampus, basal forebrain, and cortex. Interestingly, the input-to-starter ratio was not significantly different (Figure S6P). Consistent with these data, we observed extensive recruitment of both glutamatergic and cholinergic excitatory as well as GABAergic inhibitory neurons in PDX and co-culture models (Figures S6Q–S6S), highlighting the tumor's capability to integrate with various neurotransmitter systems across the brain. An unbiased analysis of publicly available single-cell sequencing data[5] showed that glioblastoma cells from human patients express genes from a broad variety of neurotransmitter receptor classes (Figures 5J and S6T; Table S1). Focusing on strongly expressed acetylcholine receptors, we investigated putative structural cholinergic synapses via combined immunohistochemistry of pre- and postsynaptic proteins together with a tumor marker and confocal Airyscan microscopy (STAR Methods). Putative cholinergic synapses were identified on glioblastoma cells in both human glioblastoma tissue and PDX models (Figures 5K–5M), with a higher density observed in human tissue (Figure 5N).

Functional cholinergic neuron-tumor communication

Based on the diverse neuronal subpopulations recruited by glioblastoma and neurotransmitter receptor gene expression profiles, we investigated whether different neurotransmitters elicit a functional response in glioblastoma cells using a functional neurotransmitter receptor screening (Figure 6A; STAR Methods). Correlated calcium events within glioblastoma cells,[8] triggered by a localized, time-resolved application of high-concentration neurotransmitters, served as a measure of functional neurotransmitter receptor expression. Interestingly, acetylcholine, ATP, glutamate, and dopamine led to high degrees of responsiveness in two patient-derived models, in line with the recruitment of neuromodulatory circuits by glioblastoma across PDX models. The event areas of calcium transients after neurotransmitter response were larger than those observed spontaneously (Figures 6B–6D and S7A; Video S5). In contrast, GABA, serotonin, and glycine showed

(I) Correlation of mean input-to-starter values per patient-derived model with the respective mean invasion speed of all analyzed models in co-culture (simple linear regression, Pearson's r = 0.3475, p = 0.2683, left) and of models with high neuronal connectivity (Pearson's r = 0.9679, p = 0.0321, right).
(J) Mean somatokinetic speed shown in highly invasive microregions (div5–7) versus more stable regions (div12 and 13) in S24 co-cultures (n = 630 cells in invasive+, n = 631 cells in invasive− regions, Mann-Whitney test).
(K) Exemplary images of highly invasive (left) and less-invasive regions (right). S24 GB^{Starter} cells (white, asterisks), connected^{TUM} neurons (CVS-N2c$^{\Delta G}$-eGFP(EnvA), green, arrows).
(L) Input-to-starter ratio of highly invasive (div5 infection) versus more stable microregions (div11 infection) in S24 co-cultures (n = 23 invasive+, n = 8 invasive− regions, Mann-Whitney test).
(M) Median invasivity score in tumor rim versus core from different patients in Yu dataset[66] (n = 2,795 cells from 9 patients, Wilcoxon test).
(N) Mean invasivity score correlated with mean synaptogenic score per patient in Neftel dataset[5] (n = 7,929 cells from 28 patients, Pearson's test).
(O) *In vitro* live-cell time-lapse imaging portraying an invasive S24 GB^{Starter} cell (white, arrowhead) and newly infected connected^{TUM} neurons (CVS-N2c$^{\Delta G}$-eGFP(EnvA), green, asterisk, top), and a stable S24 GB^{Starter} cell (white, arrowheads) and connected^{TUM} neurons (CVS-N2c$^{\Delta G}$-eGFP(EnvA), green, bottom). Post processed with denoise.ai.
See also Figure S5 and Video S4.

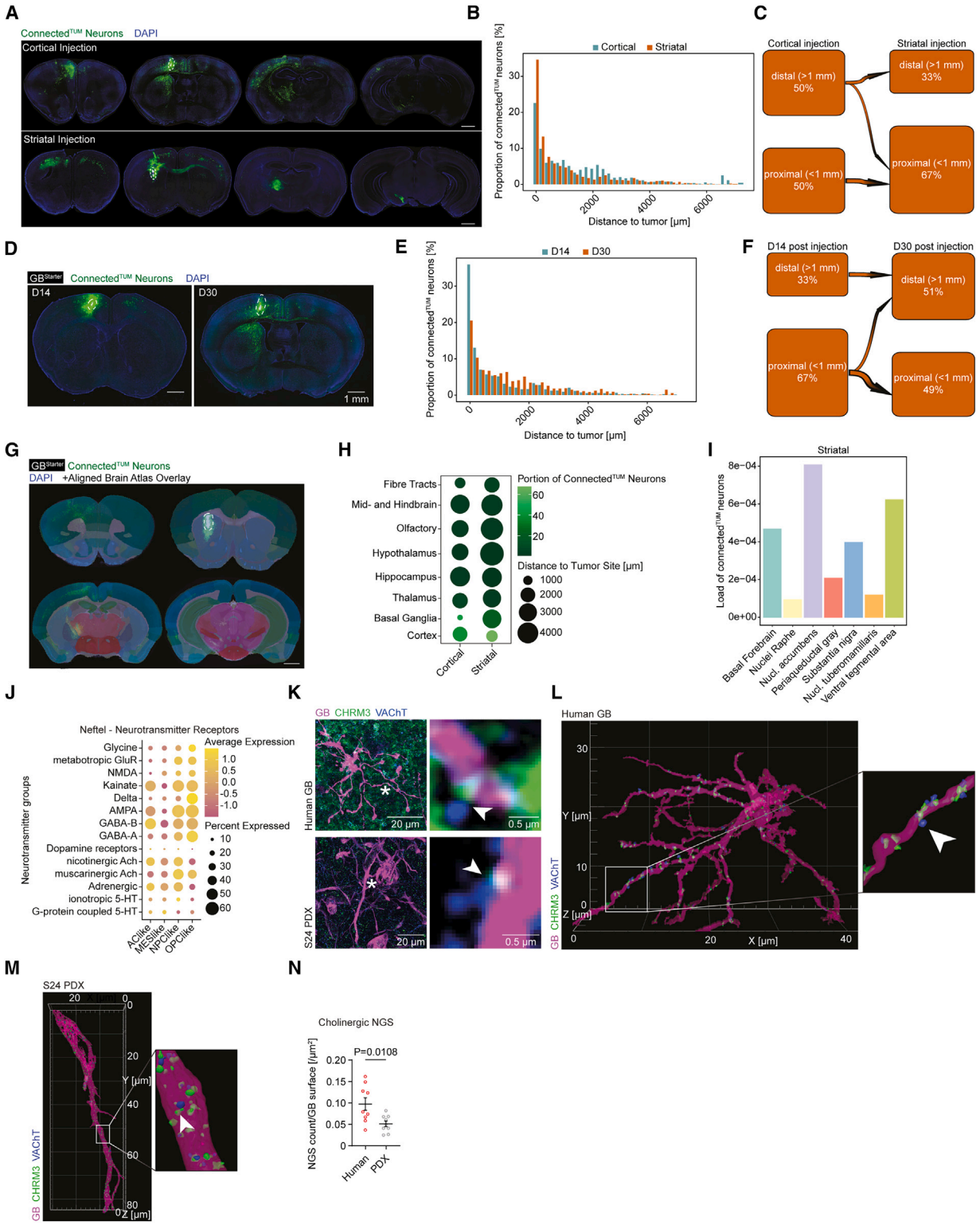

Figure 5. Brain-tumor-bearing, region-dependent formation of neuron-tumor networks

(A) Exemplary *ex vivo* brain overviews of cortical (top, SAD-B19$^{\Delta G}$-eGFP(EnvA)) and striatal (bottom, CVS-N2c$^{\Delta G}$-eGFP(EnvA)) tumors in PDX model S24. Tumor localization (dashed white circles), scale bar, 1 mm.

(legend continued on next page)

low responsiveness of glioblastoma in both patient-derived models.

Thus, we further characterized the functional acetylcholine receptor expression in glioblastoma cells. The muscarinic acetylcholine receptor antagonist atropine blocked acetylcholine-induced calcium events (Figures 6E, S7B, and S7C), whereas blocking nicotinic receptors did not diminish acetylcholine-induced calcium transients (Figures S7D and S7E). Single-cell RNA sequencing datasets[5,66] revealed high expression of muscarinic acetylcholine receptor M3 (CHRM3) in glioblastoma (Figure S7F), which correlated with a higher invasivity score (Figure 6F) and was associated with a high-neural score[61] (Figure S7G). We could also identify cholinergic neurons in single-cell RNA sequencing data of human glioblastoma (Figure S7H).

Further, we investigated whether cholinergic neurons could promote glioblastoma somatokinesis. Neurons from the basal forebrain, with a higher density of cholinergic presynapses, promoted glioblastoma migration and proliferation compared with glioblastoma monocultures (Figures 6G and S7I–S7K).

We also found that the knockdown of the CHRM3 receptor in glioblastoma cells led to less cortical tumor growth in a PDX model (Figures 6H, 6I, S7L, and S7M).

Together, acetylcholine emerged as a key mediator in neuron-to-tumor communication and tumor growth.

Radiotherapy-driven remodeling of neuron-tumor networks

Sequencing data of matched primary and recurrent glioblastoma showed conflicting results regarding the role of the neural microenvironment and glioblastoma's intrinsic neural signatures for its therapeutic resistance.[4,11,74] Exploiting time-resolved retrograde tracing, we investigated the role of neuron-tumor networks in radiotherapy-induced therapeutic resistance in a co-culture model. Although radiotherapy reduced the glioblastoma cell number as expected (Figures S8A and S8B), the average number of connected^{TUM} neurons per glioblastoma cell significantly increased, overall increasing neuron-tumor connectivity (Figures 7A and 7B), whereas the fraction of recruited glutamatergic and GABAergic neurons did not change (Figures S8C–S8F). We hypothesized that the increased neuron-tumor connectivity is driven by neuronal-activity-dependent factors and performed whole-cell patch-clamp electrophysiology of connected^{TUM} neurons, with and without radiotherapy. Interestingly, we saw a significant increase in action potential bursting activity following radiotherapy, with a higher number of action potential bursts per minute and an increased area under the curve of action potential bursts (Figures 7C and 7D). In contrast, basic electrophysiological properties of connected^{TUM} neurons after radiation did not change (Figures S8G–S8K). Notably, irradiated neurons alone did not exhibit neuronal hyperexcitability (Figures S8L–S8U). The observation of increased action potential bursts after radiotherapy aligns with clinical observations of increased epileptic seizures among a subset of glioma patients following radiotherapy.[75]

We investigated whether neuron-tumor connectivity is driven by neuronal activity, similar to synaptogenesis in neuron-to-neuron synapses.[76,77] We employed the non-competitive AMPA-receptor (AMPAR) antagonist perampanel (PER), commonly used as antiepileptic drug to inhibit neuronal activity.[78] Consequently, neuron-tumor connectivity and tumor cell number significantly decreased, highlighting the role of neuronal activity in the formation of neuron-tumor networks (Figures 7E–7G and S8V).[8,16,17]

Next, we investigated whether simultaneous inhibition of neuronal activity and radiotherapy would decrease neuron-tumor network connectivity and increase therapeutic efficacy.

Neuron-tumor connectivity was significantly reduced after combined radiotherapy and AMPAR inhibition as compared with radiotherapy alone (Figures 7H and 7I). Consequently, glioblastoma progression was reduced by this therapy combination in co-cultures and a PDX model (Figures 7J–7O).

Rabies-virus-based ablation of tumor-connected neurons inhibits glioblastoma progression

To investigate whether retrograde tracing with the modified rabies virus itself could be used to specifically ablate connected^{TUM}

(B) Histogram showing the distribution of connected^{TUM} neurons in relation to the distance from the tumor site for cortical (blue) and striatal (orange) tumors (n = 8,839 connected^{TUM} neurons in 7 cortical, n = 30,528 connected^{TUM} neurons in 11 striatal tumors).
(C) River plot illustrating the distribution of distal and proximal neuron-to-tumor connections for cortical and striatal tumors (n = 8,839 connected^{TUM} neurons in 7 cortical, 30,528 connected^{TUM} neurons in 11 striatal tumors).
(D) Representative brain sections showing the progression of the tumor and its neuronal connectome between 14 and 30 days following tumor injection in PDX model S24 (SAD-B19$^{\Delta G}$-eGFP(EnvA)). Tumor localization (dashed white circle).
(E) As in (B) but 14 (blue) and 30 (orange) days following tumor injection (n = 26,419 connected^{TUM} neurons in 11 day 14, n = 12,948 connected^{TUM} neurons in 7 day 30 tumors).
(F) As in (C) but 14 and 30 days following tumor injection (n = 26,419 connected^{TUM} neurons in 11 day 14, n = 12,948 connected^{TUM} neurons in 7 day 30 tumors).
(G) Exemplary S24 PDX brain sections aligned to the Allen Brain Atlas using the QUINT workflow (STAR Methods). Connected^{TUM} neurons (CVS-N2c$^{\Delta G}$-eGFP(EnvA), green). Tumor localization (dashed white circle), scale bar, 1 mm.
(H) Dot plot showing the brain region affinity of connected^{TUM} neurons based on tumor site (n = 8,839 connected^{TUM} neurons in 7 cortical, n = 30,528 connected^{TUM} neurons in 11 striatal tumors).
(I) Bar plot showing the load of connected^{TUM} neurons in various neuromodulatory circuits (n = 30,528 connected^{TUM} neurons in 11 striatal tumors).
(J) Dot plot showing the expression of various neurotransmitter groups of different gene-based cell states in Neftel dataset[5] (n = 7,929 cells).
(K) Representative maximum intensity projection Airyscan microscopy of cholinergic neuron-glioma synapses (NGSs) in human GB (top left) and S24 PDX (bottom left). Zoom-ins (right) on regions of interest (asterisks) depicting cholinergic NGS (arrowheads).
(L) 3D rendering of cholinergic NGS (arrowhead) on a human GB cell.
(M) 3D rendering of cholinergic NGS (arrowhead) on a S24 PDX cell.
(N) Density comparison of cholinergic NGS on human GB versus PDX tissue (n = 9 cells each, unpaired t test).
See also Figure S6 and Table S1.

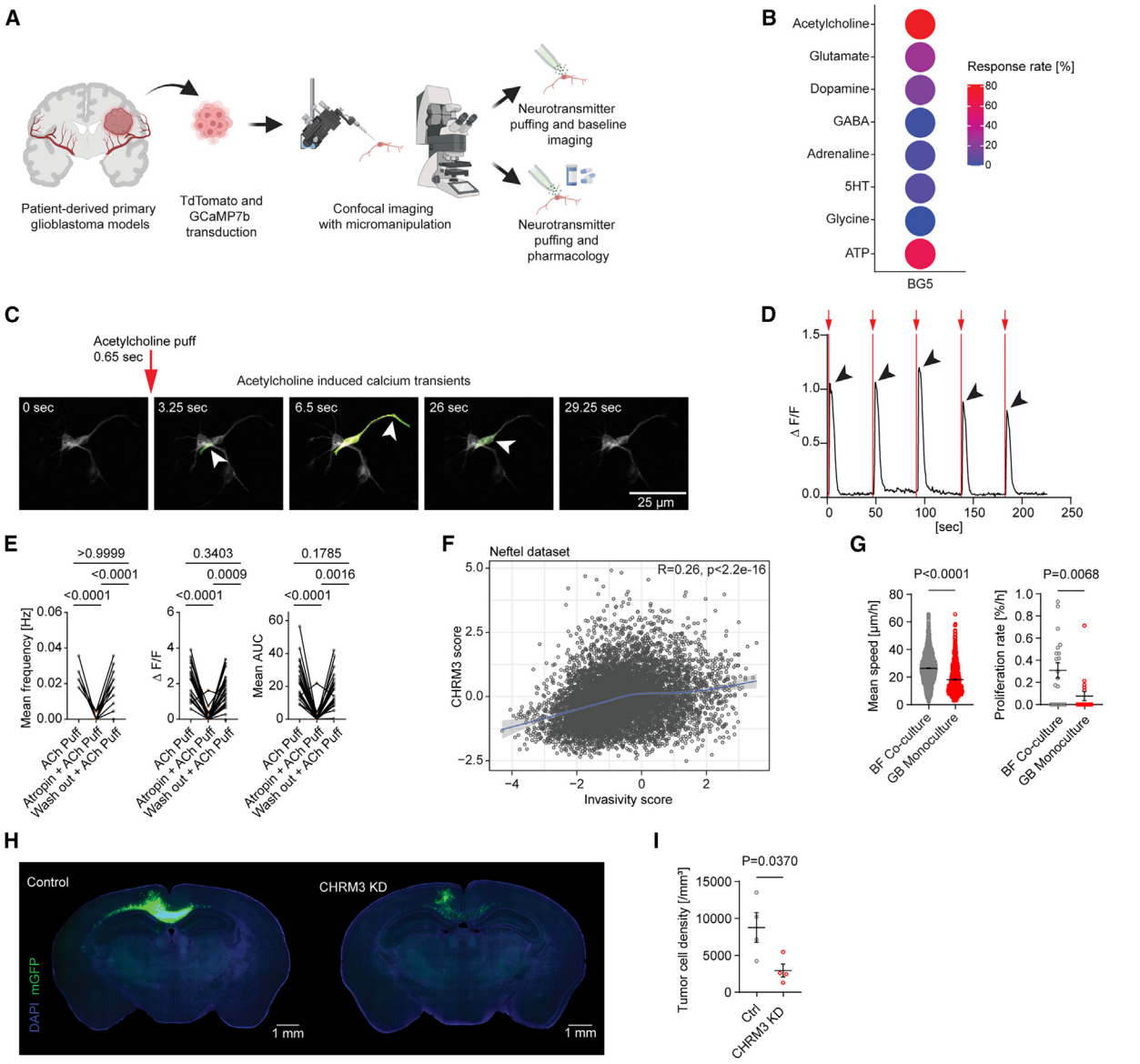

Figure 6. Effects of cholinergic input on glioblastoma biology

(A) Schematic workflow of the functional neurotransmitter screening in co-culture.

(B) Dot plot indicating the calcium event response rate to stimulation with different neurotransmitters (n = 78 cells from patient-derived model BG5).

(C) Time-lapse imaging showing an exemplary acetylcholine puff and following acetylcholine-induced calcium events (arrowheads) in a BG5 GB cell.

(D) Calcium imaging trace of GB cell showing acetylcholine stimulation (arrows) and the following calcium event (arrowheads).

(E) Mean calcium event frequency, ΔF over F, and area under the curve of calcium transients in response to acetylcholine puffing, blocking through atropine, and after wash-out in S24 (n = 22 cells, Friedman test).

(F) Correlation of CHRM3 expression and invasivity score in Neftel[5] dataset (n = 7,929 cells, Pearson's test).

(G) Mean somatokinetic speed of S24 GB cells co-cultured with basal forebrain (BF) neurons compared with a GB monoculture (n = 1,633 [BF co-culture], n = 1,052 [GB monoculture] cells, Mann-Whitney test, left). Proliferation rate per hour of S24 GB cells in BF co-culture compared with GB monoculture (n = 20 [BF co-culture], n = 18 [GB monoculture] FoVs, Mann-Whitney test, right).

(H) Representative S24 PDX brain slices of control (left) versus CHRM3 knockdown mice (right).

(I) Tumor cell density in the ipsilateral retrosplenial cortex in control versus CHRM3 knockdown mice (n = 4 mice each, unpaired t test).

See also Figure S7 and Video S5.

neurons to inhibit glioblastoma progression, we implemented a Cre-*loxP* strategy to specifically ablate connected^{TUM} neurons in a co-culture model by infecting the neural tumor microenvironment with an adeno-associated virus (AAV) expressing a Cre-dependent, genetically engineered designer caspase 3 whose expression led to cell apoptosis. Hereby, we could specifically

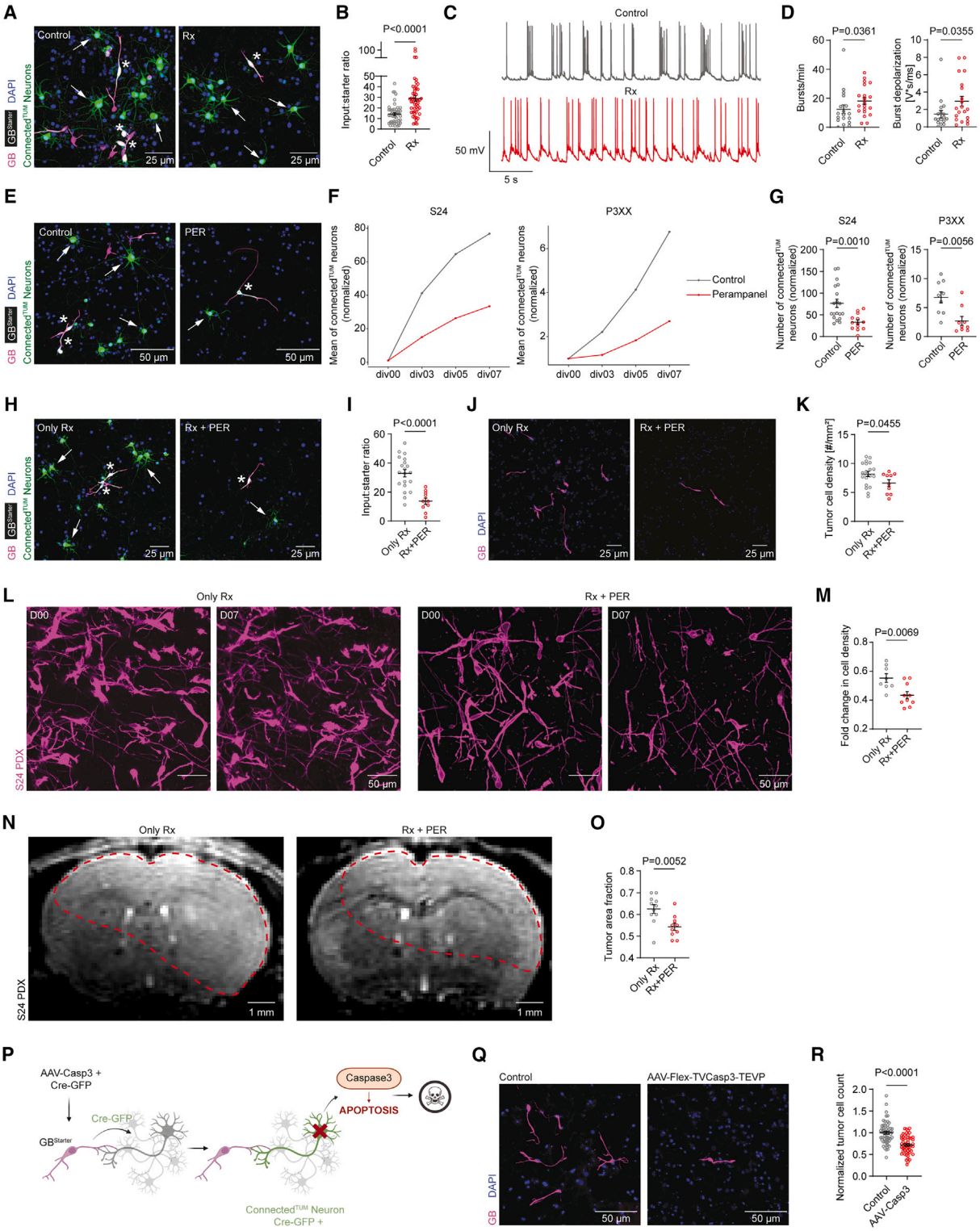

Figure 7. Tackling glioblastoma by disrupting neuron-tumor networks

(A) PMs of S24 GB^{Starter} cells (white, asterisks) and connected^{TUM} neurons (CVS-N2c$^{\Delta G}$-eGFP(EnvA), green, arrows) in co-culture under control (left) versus radiotherapy conditions (right).

(B) Input-to-starter ratio under control versus radiotherapy conditions (n = 46 control, n = 48 irradiated samples, Mann-Whitney test).

(legend continued on next page)

kill connected^{TUM} neurons and investigate its effect on tumor cells (Figure 7P).[79,80] The eradication of connected^{TUM} neurons resulted in a significant reduction in tumor cells (Figures 7Q and 7R). Additional inhibition of neuronal excitability and AMPAergic synaptic transmission did not show an additive effect to the ablation of connected^{TUM} neurons, whereas Adam10 inhibition, leading to reduced shedding of Neuroligin 3, a paracrine molecule promoting glioma growth,[81,82] added to the effect of neuronal ablation of connected^{TUM} neurons alone (Figures S8W and S8X).

DISCUSSION

It is becoming increasingly clear that synaptic neuron-tumor networks are an important hallmark of yet incurable glioblastomas.[12,13] Our research introduces a comprehensive and reproducible methodology platform capable of investigating the neuronal connectome of glioblastoma across a range of model systems. Technologies such as monosynaptic retrograde tracing are important in highly invasive tumors, contrasting with dye injection techniques precluding cellular specificity of the labeled connectome.[29] Importantly, the ability to investigate the neuronal connectome of patient-derived models in a human tissue context opens up the potential for personalized therapeutic approaches.

By integrating longitudinal imaging, electrophysiology, molecular characterization, and functional tumor biological assays, we gained insights into the malignant circuitry's evolution. A nuanced picture has emerged, revealing the bidirectional mechanisms that underpin neuron-tumor connectivity: tumor cells are able to establish transient, functional connections with neurons regardless of their molecular or functional properties. Concurrently, the functional neuron-tumor connectivity can be significantly increased by neuronal activity.

The impact of known glioma-induced alterations in neural circuits[17,24,46,49,83] on brain function and their contribution to disease progression warranted further investigation. We found that the formation of neuron-tumor networks precedes the onset of neuronal dysfunction, such as hyperexcitability, and consequent neurological deficits. This aligns with clinical findings where epileptic seizures occur in later disease stages where curable surgical resection of glioblastoma is no longer feasible.[56,63]

Functional imaging revealed that connected^{TUM} neurons are well integrated into neural circuits of unconnected^{TUM} neurons. With neuronal activity being able to elicit calcium transients in glioblastoma cells, this suggests the concept of a primary, directly connected, and secondary, indirectly connected, neuronal connectome. These data also make it unlikely that connected^{TUM} neurons are created via neurogenesis, a phenomenon previously described in prostate cancer,[84] as neurons derived from neurogenesis presumably need several weeks of integrating into neuronal networks.[85] These complex networks highlight the importance of investigating bidirectional interactions between glioblastoma and the central nervous system, including distant and even non-tumor-connected brain regions. The influence of specific neuronal types and neurotransmitters on various cancer types requires further investigation.

Importantly, early synaptic connections to brainstem neurons hinted at a strategy for glioblastoma invasion along axonal white matter tracts into the brainstem, a critical factor in the disease's lethality.[73] This observation suggests that initial synaptic connections potentially prompt glioblastoma's migration along axonal structures.

In addition to the molecular and functional characterization of neuron-tumor networks, retrograde tracing in the context of glioblastoma enabled the investigation of how neuron-tumor

(C) Representative whole-cell current-clamp recordings of spontaneous burst firing in connected^{TUM} neurons under control conditions (top) versus after radiotherapy (bottom).
(D) Bursts per minute (left) and normalized burst area (right) in control versus radiotherapy conditions (n = 18 control, n = 20 irradiated neurons, Mann-Whitney test).
(E) As in (A) but under control condition (left) versus perampanel treatment (right).
(F) Normalized mean count of connected^{TUM} neurons in patient-derived GB models S24 (left) and P3XX (right) over 7 days under control and perampanel-treated conditions (n = 19 control, n = 13 perampanel-treated samples [S24], n = 9 control, n = 9 perampanel-treated samples [P3XX]).
(G) Normalized mean count of connected^{TUM} neurons in S24 (left) and P3XX (right) on day 7 of treatment (n = 19 control, n = 13 perampanel-treated samples [S24], n = 9 control, n = 9 perampanel-treated samples [P3XX], Mann-Whitney test).
(H) As in (A) but in only irradiated (left) versus irradiated and perampanel-treated (right) conditions.
(I) Input-to-starter ratio in only irradiated versus irradiated and perampanel-treated conditions (n = 20 only irradiated, n = 10 irradiated and perampanel-treated samples, unpaired t test).
(J) Representative images of tumor regions in only irradiated (left) versus irradiated and perampanel-treated (right) conditions in S24 co-culture.
(K) Tumor cell density under only irradiated versus irradiated and perampanel-treated condition in co-culture (n = 20 only irradiated, n = 10 irradiated and perampanel-treated samples, unpaired t test).
(L) IV2PM of tumor regions on days 0 and 7 of only irradiation versus irradiation following perampanel treatment.
(M) Fold change in cell density in 7 days in only irradiated mice versus mice treated with perampanel 2 weeks prior to irradiation (n = 8 FoVs from 5 mice for only irradiated, n = 10 FoVs from 5 mice for perampanel and irradiated).
(N) T2-weighted *in vivo* MRI images of only irradiated mice versus mice treated with perampanel 2 weeks prior to irradiation. Segmented tumor areas (dashed red circles).
(O) Tumor area fraction in only irradiated mice versus mice treated with perampanel 2 weeks prior to irradiation (n = 11 mice for only irradiated, n = 10 mice for perampanel and irradiated, unpaired t test).
(P) Schematic of experimental paradigm for genetic ablation of connected^{TUM} neurons.
(Q) Representative images of *in vitro* S24 GB cells under control conditions (left) versus genetic ablation of connected^{TUM} neurons (right) in co-culture.
(R) Tumor cell density under control conditions versus genetic ablation of connected^{TUM} neurons in co-culture (n = 56 control, n = 54 caspase-treated samples, unpaired t test).
See also Figure S8.

networks are formed and therapeutically exploited. Interestingly, we could see how neuronal-activity-dependent formation of neuron-tumor networks parallels similar establishments of physiological synaptic connections during development.[76,77] Furthermore, elevated neuronal activity through radiotherapy increased neuron-tumor connectivity and showed that an inhibition of AMPA receptors in combination with standard-of-care radiotherapy yielded additive therapeutic effects. This demonstrates an additional role of neuron-glioma synaptic communication in therapeutic resistance, explaining a potential role of neuronal gene expression signatures of glioblastoma in the recurrent setting.[4]

Using our rabies-based tracing approach, our proof-of-concept investigation demonstrated how further modification of the rabies virus could be directly used to induce apoptosis of connected^{TUM} neurons, thereby decreasing tumor progression and offering a potential therapeutic strategy.

Taken together, we established a framework to investigate the neuronal connectome of glioblastoma that can be translated to study not only other brain tumors but also cancers outside the brain. We furthered our understanding about the organization, formation, and therapeutic opportunities yielded by neuron-tumor networks.

Limitations of the study

The study primarily focuses on the early stages of neuron-tumor network formation, highlighting a need for further exploration across various stages of tumor development to fully understand how these interactions evolve and impact disease progression and therapeutic responses over time.

One limitation is the neurotoxic potential associated with the use of rabies virus for retrograde tracing over time.[86–88] This underscores the importance of utilizing and further adapting less-toxic labeling strategies for glioblastoma[87,88] to enable longer observation periods without adverse effects on neuron and tumor cell health. In addition, the effects of rabies virus strains and constructs on tumor cells across patient-derived models will need further investigation *in vitro* and *in vivo* over time. Further, rabies-mediated retrograde tracing did not label all synaptic inputs in previous work, illustrating a potential underestimation of the entire neuronal connectome of glioblastoma.[89,90] Additionally, although a high level of neuron-tumor connectivity is observed, the precise mechanisms underpinning the functional interactions between neurons and glioma cells remain unclear and require further elucidation. Further investigation of cholinergic neurotransmission and the effects of other neuronal subpopulations on glioblastoma are needed.

The feasibility of using a modified rabies virus to specifically ablate connected^{TUM} neurons also poses a significant opportunity. Although the study provides a proof-of-concept, further research is necessary to determine how these viral constructs can be adapted for efficacy and safety in both PDX models and a clinical-translational context without the need for genetically modifying neurons via AAVs. Lastly, investigating neuron-tumor interactions across different malignancies could enhance our understanding of these complex networks and pave the way for future therapeutic strategies.

RESOURCE AVAILABILITY

Lead contact

Further information and requests for resources should be directed to and will be fulfilled by the lead contact, Varun Venkataramani (varun.venkataramani@med.uni-heidelberg.de).

Materials availability

This study did not generate new unique reagents.

Data and code availability

- Sequencing data can be found at https://doi.org/10.5281/zenodo.13956432 (Zenodo: 13956432) and https://doi.org/10.5281/zenodo.13958300 (Zenodo: 13958300).
- Code used for analysis is available at https://github.com/venkataramani-lab/ and https://github.com/theMILOlab/SPATAData.
- Any additional information required to reanalyze the data reported in this paper is available from the lead contact upon request.

ACKNOWLEDGMENTS

The work was supported by the Deutsche Forschungsgemeinschaft (DFG, German Research Foundation), SFB 1389, UNITE Glioblastoma, project ID 404521405 (addressed to V.V., S.K.T., E.R., N.L., A.P.L, J.B., M.A.K., A.A., F.S., and M.O.B.) and project number VE1373/2-1516 (addressed to V.V.), Heidelberg University and Research Seed Capital (RiSC) from the Ministry of Science, Research and the Arts, Baden Württemberg (MWK) (addressed to V.V.). S.K.T., E.R., J.S., M.C.S., and E.G. were supported by the Deutsche Krebshilfe/German Cancer Aid (Mildred Scheel scholarship for MD students). C.P.B. was supported by the DFG (BE7081/2-1). We thank Hilmar Bading, Department of Neurobiology and Interdisciplinary Center for Neurosciences, Heidelberg University for the opportunity to carry out electrophysiological experiments in his laboratory. S.H. received funding from BMBF grant 01GM2202A and STOP-FSGS and DFG CRC1192. C.A. is supported by the Chica and Heinz Schaller Foundation, the Brain and Behavior Research Foundation (Young Investigator award, 2019), the DFG (SFB1158-SO2), and the Fritz Thyssen Foundation (grant 10.21.0.019MN). J.C. is supported by a DAAD/ANID fellowship (57451854/62180003). A.K.S. was supported by the Emmy Noether Programme (DFG) and is a fellow of the Hertie Network of Excellence in Clinical Neuroscience. V.V. and M.K. were supported by the EZN (Europäisches Zentrum für Neuroonkologie). V.V. was supported by the Schwiete Stiftung. We thank the data storage service SDS@hd, supported by the MWK. This publication was supported through state funds approved by the State Parliament of Baden-Württemberg for the Innovation Campus Health + Life Science Alliance Heidelberg/Mannheim. Rabies viruses for the initial experiments were a gift from Karl-Klaus Conzelmann. We thank the Viral Core Facility Charité for supplying viral constructs used in this study. We thank M. Kaiser, M. Schmitt, F. Gleiche, S. Wendler, and K. Eghbalian for technical assistance and K. Becker, K. Dell, A. Riedasch, and B. Böck for support in animal care and animal experiments. We thank the Light Microscopy and Flow Cytometry Core Facilities of the German Cancer Research Center (DKFZ), U. Engel, and C. Ackermann; the Nikon Imaging Center of the Heidelberg University; the Single-Cell Open Lab of the DKFZ and C. Pitzer; and the Interdisciplinary Neurobehavioral Core; Preclinical Trial Unit at the DKFZ, S. Hamelmann, D. Haag, and M. Fischer. Results shown here are partly based upon data generated by the TCGA Research Network (https://www.cancer.gov/tcga).

AUTHOR CONTRIBUTIONS

Supervision, V.V.; conceptualization, S.K.T., E.R., and V.V.; methodology, S.K.T., E.R., N.L., C.P.B., J.S., M.C.S., R.P.L., N.W., and V.V.; project administration, S.K.T., E.R., and V.V.; investigation, S.K.T., E.R., N.L., C.P.B., A.H., J.S., A.J.F., A.P.L., N.D., E.K., J.W., S.J.S., M.C.S., N.S., R.L.P., V.B., T.W., E.G., N.W., O.T.A., M.B., J.B., J.C., B.B., J.G.S., S.H.C., M.C.P., G.V., R.D., Y.Z., F.H., S.H., A.K.S., M.S., F.S., and V.V.; formal analysis, S.K.T., E.R.,

N.L., C.P.B., J.S., A.J.F., A.P.L., N.D., E.K., J.W., S.J.S., M.C.S., N.S., R.L.P., T.W., E.G., B.B., J.G.S., M.C.P., R.D., Y.Z., F.H., S.H., F.T.K., M.S., F.S., M.O.B., F.L.R., D.H.H., and V.V.; resources, O.T.A., J.C., S.H.C., G.V., M.A.K., F.T.K., M.T., A.K.S., K.F.-N., C.A., J.S.-R., A.A., F.S., M.O.B., B.S., F.L.R., D.H.H., and V.V.; visualization, S.K.T., E.R., N.L., C.P.B., A.H., J.S., A.J.F., A.P.L., E.K., J.W., S.J.S., M.C.S., N.S., R.L.P., T.W., E.G., N.W., B.B., J.G.S., M.C.P., R.D., Y.Z., F.H., S.H., M.O.B., F.L.R., D.H.H., and V.V.; writing – original draft, V.V.; writing – review and editing, S.K.T., E.R., N.L., C.P.B., A.H., J.S., A.P.L., E.K., J.W., S.J.S., M.C.S., N.S., R.L.P., T.W., E.G., N.W., B.B., J.G.S., M.C.P., G.V., R.D., Y.Z., F.H., S.H., M.A.K., M.S., K.F.-N., C.A., J.S.-R., M.O.B., F.L.R., D.H.H., and V.V.; funding acquisition, V.V.

DECLARATION OF INTERESTS

J.S.-R. reports funding from GSK, Pfizer, and Sanofi and fees/honoraria from Travere Therapeutics, Stadapharm, Astex, Owkin, Pfizer, and Grunenthal.

STAR★METHODS

Detailed methods are provided in the online version of this paper and include the following:

- KEY RESOURCES TABLE
- EXPERIMENTAL MODEL AND STUDY PARTICIPANT DETAILS
- METHOD DETAILS
  - Lentiviral vector and plasmid generation of pFU-TVA-2A-mCherry-2A-oGlycoprotein
  - Packaging of CVS-N2c$^{\Delta G}$ and SAD-B19$^{\Delta G}$
  - Patient-derived glioblastoma cultures
  - 850k methylation array analysis
  - Harvesting cortical tissue from human patients
  - Human organotypic slice cultures
  - Spatial Transcriptomics
  - Surgical procedures
  - Intravital microscopy
  - Intravital microscopy analysis of dendritic plasticity
  - Airyscan microscopy and analysis of dendrites in *ex vivo* brain slices
  - Assessment of mouse behavior
  - Stereotactic AAV- injection
  - Optogenetic stimulation and consecutive time-lapse imaging
  - Analysis of tumor area and density of CHRM3 knockdown mice
  - Combined irradiation and perampanel therapy *in vivo*
  - Radiotherapy of non-tumor-bearing mice prior to tumor implantation
  - Sample preparation, immunohistochemistry, and confocal microscopy
  - Immunohistochemistry of FFPE human sections
  - Airyscan microscopy of putative cholinergic synapses in *ex vivo* PDX brain slices and FFPE human sections
  - Mouse and rat cortical, hippocampal and basal forebrain cultures
  - Quantification of VAChT signal in basal forebrain cultures using Airyscan microscopy
  - Human iPSC- and ESC-derived neurons
  - Cell viability assays
  - Evaluation of rabies-induced toxicity
  - Single-cell apoptosis-related genes expression analysis
  - Direct and sequential labeling of glioblastoma cells for retrograde tracing
  - Sparse and dense sequential retrograde labeling
  - *In vitro* live-cell time-lapse imaging of retrograde labeling
  - *In vitro* live-cell time-lapse imaging of neuron-tumor co-cultures
  - Somatokinetic speed analysis with TrackMate
  - Infection lag time analysis
  - Drug treatment and radiotherapy in co-cultures
  - Rabies virus-based genetic ablation of connected^{TUM} neurons
  - Single-cell RNA sequencing
  - Sequencing pre-processing and analysis
  - Invasivity module score for single-cell RNA sequencing analyses
  - Synaptogenic module score for single-cell RNA sequencing analyses
  - DNA methylation profiling of a clinical patient cohort
  - Survival analysis
  - Single-cell neurotransmitter genes expression analysis
  - Analysis of publicly available singe-cell RNA sequencing data
  - TCGA multi-omic data analysis
  - Determination of input-to-starter ratios
  - *Ex vivo* input-to-starter ratio analysis
  - Cell type analysis of connected^{TUM} neurons
  - Expansion microscopy
  - Tissue clearing
  - Light-sheet microscopy
  - Calcium imaging of connected^{TUM} and unconnected^{TUM} neurons
  - Calcium analysis of connected^{TUM} and unconnected^{TUM} neurons
  - Functional neurotransmitter receptor screening
  - Calcium imaging analysis
  - Acute brain slice preparation
  - Whole-cell patch-clamp electrophysiology
  - Patch-clamp analysis
  - Electrophysiological characterization with high-density microelectrode arrays
  - Cluster analysis of connected^{TUM} neurons over time
  - Whole brain atlas mapping of tumor cells and connected^{TUM} neurons
  - Stochastic neurotransmitter and cell class determination of connected^{TUM} neurons
  - *Ex vivo* magnet resonance imaging
  - General image processing and visualization
- QUANTIFICATION AND STATISTICAL ANALYSIS

SUPPLEMENTAL INFORMATION

Supplemental information can be found online at https://doi.org/10.1016/j.cell.2024.11.002.

Received: March 18, 2024
Revised: September 16, 2024
Accepted: November 4, 2024
Published: December 6, 2024

REFERENCES

1. Weller, M., Wick, W., Aldape, K., Brada, M., Berger, M., Pfister, S.M., Nishikawa, R., Rosenthal, M., Wen, P.Y., Stupp, R., et al. (2015). Glioma. Nat. Rev. Dis. Primers *1*, 15017. https://doi.org/10.1038/nrdp.2015.17.
2. Ostrom, Q.T., Price, M., Neff, C., Cioffi, G., Waite, K.A., Kruchko, C., and Barnholtz-Sloan, J.S. (2022). CBTRUS Statistical Report: Primary Brain and Other Central Nervous System Tumors Diagnosed in the United States in 2015-2019. Neuro. Oncol *24* (*Suppl 5*), v1–v95. https://doi.org/10.1093/neuonc/noac202.
3. Weller, M., van den Bent, M., Preusser, M., Le Rhun, E., Tonn, J.C., Minniti, G., Bendszus, M., Balana, C., Chinot, O., Dirven, L., et al. (2021). EANO guidelines on the diagnosis and treatment of diffuse gliomas of adulthood. Nat. Rev. Clin. Oncol. *18*, 170–186. https://doi.org/10.1038/s41571-020-00447-z.
4. Varn, F.S., Johnson, K.C., Martinek, J., Huse, J.T., Nasrallah, M.P., Wesseling, P., Cooper, L.A.D., Malta, T.M., Wade, T.E., Sabedot, T.S., et al. (2022). Glioma progression is shaped by genetic evolution and microenvironment interactions. Cell *185*, 2184–2199.e16. https://doi.org/10.1016/j.cell.2022.04.038.
5. Neftel, C., Laffy, J., Filbin, M.G., Hara, T., Shore, M.E., Rahme, G.J., Richman, A.R., Silverbush, D., Shaw, M.L., Hebert, C.M., et al. (2019). An Integrative Model of Cellular States, Plasticity, and Genetics for Glioblastoma. Cell *178*, 835–849.e21. https://doi.org/10.1016/j.cell.2019.06.024.

6. Patel, A.P., Tirosh, I., Trombetta, J.J., Shalek, A.K., Gillespie, S.M., Wakimoto, H., Cahill, D.P., Nahed, B.V., Curry, W.T., Martuza, R.L., et al. (2014). Single-cell RNA-seq highlights intratumoral heterogeneity in primary glioblastoma. Science *344*, 1396–1401. https://doi.org/10.1126/science.1254257.

7. Garofano, L., Migliozzi, S., Oh, Y.T., D'Angelo, F., Najac, R.D., Ko, A., Frangaj, B., Caruso, F.P., Yu, K., Yuan, J., et al. (2021). Pathway-based classification of glioblastoma uncovers a mitochondrial subtype with therapeutic vulnerabilities. Nat. Cancer *2*, 141–156. https://doi.org/10.1038/s43018-020-00159-4.

8. Venkataramani, V., Yang, Y., Schubert, M.C., Reyhan, E., Tetzlaff, S.K., Wißmann, N., Botz, M., Soyka, S.J., Beretta, C.A., Pramatarov, R.L., et al. (2022). Glioblastoma hijacks neuronal mechanisms for brain invasion. Cell *185*, 2899–2917.e31. https://doi.org/10.1016/j.cell.2022.06.054.

9. Osswald, M., Jung, E., Sahm, F., Solecki, G., Venkataramani, V., Blaes, J., Weil, S., Horstmann, H., Wiestler, B., Syed, M., et al. (2015). Brain tumour cells interconnect to a functional and resistant network. Nature *528*, 93–98. https://doi.org/10.1038/nature16071.

10. Verhaak, R.G.W., Hoadley, K.A., Purdom, E., Wang, V., Qi, Y., Wilkerson, M.D., Miller, C.R., Ding, L., Golub, T., Mesirov, J.P., et al. (2010). Integrated genomic analysis identifies clinically relevant subtypes of glioblastoma characterized by abnormalities in PDGFRA, IDH1, EGFR, and NF1. Cancer Cell *17*, 98–110. https://doi.org/10.1016/j.ccr.2009.12.020.

11. Hoogstrate, Y., Draaisma, K., Ghisai, S.A., van Hijfte, L., Barin, N., de Heer, I., Coppieters, W., van den Bosch, T.P.P., Bolleboom, A., Gao, Z., et al. (2023). Transcriptome analysis reveals tumor microenvironment changes in glioblastoma. Cancer Cell *41*, 678–692.e7. https://doi.org/10.1016/j.ccell.2023.02.019.

12. Winkler, F., Venkatesh, H.S., Amit, M., Batchelor, T., Demir, I.E., Deneen, B., Gutmann, D.H., Hervey-Jumper, S., Kuner, T., Mabbott, D., et al. (2023). Cancer neuroscience: State of the field, emerging directions. Cell *186*, 1689–1707. https://doi.org/10.1016/j.cell.2023.02.002.

13. Venkataramani, V., Schneider, M., Giordano, F.A., Kuner, T., Wick, W., Herrlinger, U., and Winkler, F. (2022). Disconnecting multicellular networks in brain tumours. Nat. Rev. Cancer *22*, 481–491. https://doi.org/10.1038/s41568-022-00475-0.

14. Venkataramani, V., Tanev, D.I., Kuner, T., Wick, W., and Winkler, F. (2021). Synaptic Input to Brain Tumors: Clinical Implications. Neuro. Oncol *23*, 23–33. https://doi.org/10.1093/neuonc/noaa158.

15. Monje, M., Borniger, J.C., D'Silva, N.J., Deneen, B., Dirks, P.B., Fattahi, F., Frenette, P.S., Garzia, L., Gutmann, D.H., Hanahan, D., et al. (2020). Roadmap for the Emerging Field of Cancer Neuroscience. Cell *181*, 219–222. https://doi.org/10.1016/j.cell.2020.03.034.

16. Venkataramani, V., Tanev, D.I., Strahle, C., Studier-Fischer, A., Fankhauser, L., Kessler, T., Körber, C., Kardorff, M., Ratliff, M., Xie, R., et al. (2019). Glutamatergic synaptic input to glioma cells drives brain tumour progression. Nature *573*, 532–538. https://doi.org/10.1038/s41586-019-1564-x.

17. Venkatesh, H.S., Morishita, W., Geraghty, A.C., Silverbush, D., Gillespie, S.M., Arzt, M., Tam, L.T., Espenel, C., Ponnuswami, A., Ni, L., et al. (2019). Electrical and synaptic integration of glioma into neural circuits. Nature *573*, 539–545. https://doi.org/10.1038/s41586-019-1563-y.

18. Taylor, K.R., Barron, T., Hui, A., Spitzer, A., Yalçin, B., Ivec, A.E., Geraghty, A.C., Hartmann, G.G., Arzt, M., Gillespie, S.M., et al. (2023). Glioma synapses recruit mechanisms of adaptive plasticity. Nature *623*, 366–374. https://doi.org/10.1038/s41586-023-06678-1.

19. Barron, T., Yalçın, B., Mochizuki, A., Cantor, E., Shamardani, K., Tlais, D., Franson, A., Lyons, S., Mehta, V., Jahan, S.M., et al. (2022). GABAergic neuron-to-glioma synapses in diffuse midline gliomas. Preprint at bioRxiv.

20. Pan, Y., Hysinger, J.D., Barron, T., Schindler, N.F., Cobb, O., Guo, X., Yalçın, B., Anastasaki, C., Mulinyawe, S.B., Ponnuswami, A., et al. (2021). NF1 mutation drives neuronal activity-dependent initiation of optic glioma. Nature *594*, 277–282. https://doi.org/10.1038/s41586-021-03580-6.

21. Schubert, M.C., Soyka, S.J., Tamimi, A., Maus, E., Denninger, R., Wissmann, N., Reyhan, E., Tetzlaff, S.K., Beretta, C., Drumm, M., et al. (2024). Deep intravital brain tumor imaging enabled by tailored three-photon microscopy and analysis. Nat. Commun. *15*, 7383. https://doi.org/10.1038/s41467-024-51432-4.

22. Chen, P., Wang, W., Liu, R., Lyu, J., Zhang, L., Li, B., Qiu, B., Tian, A., Jiang, W., Ying, H., et al. (2022). Olfactory sensory experience regulates gliomagenesis via neuronal IGF1. Nature *606*, 550–556.

23. Curry, R.N., Aiba, I., Meyer, J., Lozzi, B., Ko, Y., McDonald, M.F., Rosenbaum, A., Cervantes, A., Huang-Hobbs, E., Cocito, C., et al. (2023). Glioma epileptiform activity and progression are driven by IGSF3-mediated potassium dysregulation. Neuron *111*, 682–695.e9. https://doi.org/10.1016/j.neuron.2023.01.013.

24. Krishna, S., Choudhury, A., Keough, M.B., Seo, K., Ni, L., Kakaizada, S., Lee, A., Aabedi, A., Popova, G., Lipkin, B., et al. (2023). Glioblastoma remodelling of human neural circuits decreases survival. Nature *617*, 599–607. https://doi.org/10.1038/s41586-023-06036-1.

25. Huang-Hobbs, E., Cheng, Y.T., Ko, Y., Luna-Figueroa, E., Lozzi, B., Taylor, K.R., McDonald, M., He, P., Chen, H.C., Yang, Y., et al. (2023). Remote neuronal activity drives glioma progression through SEMA4F. Nature *619*, 844–850. https://doi.org/10.1038/s41586-023-06267-2.

26. Hara, T., Chanoch-Myers, R., Mathewson, N.D., Myskiw, C., Atta, L., Bussema, L., Eichhorn, S.W., Greenwald, A.C., Kinker, G.S., Rodman, C., et al. (2021). Interactions between cancer cells and immune cells drive transitions to mesenchymal-like states in glioblastoma. Cancer Cell *39*, 779–792.e11. https://doi.org/10.1016/j.ccell.2021.05.002.

27. Luo, L.Q., Callaway, E.M., and Svoboda, K. (2018). Genetic Dissection of Neural Circuits: A Decade of Progress. Neuron *98*, 256–281. https://doi.org/10.1016/j.neuron.2018.03.040.

28. Saleeba, C., Dempsey, B., Le, S., Goodchild, A., and McMullan, S. (2019). A Student's Guide to Neural Circuit Tracing. Front Neurosci. *13*, 897. https://doi.org/10.3389/fnins.2019.00897.

29. Xu, X.M., Holmes, T.C., Luo, M.H., Beier, K.T., Horwitz, G.D., Zhao, F., Zeng, W.B., Hui, M., Semler, B.L., and Sandri-Goldin, R.M. (2020). Viral Vectors for Neural Circuit Mapping and Recent Advances in Trans-synaptic Anterograde Tracers. Neuron *107*, 1029–1047. https://doi.org/10.1016/j.neuron.2020.07.010.

30. Wickersham, I.R., Lyon, D.C., Barnard, R.J.O., Mori, T., Finke, S., Conzelmann, K.K., Young, J.A.T., and Callaway, E.M. (2007). Monosynaptic restriction of transsynaptic tracing from single, genetically targeted neurons. Neuron *53*, 639–647. https://doi.org/10.1016/j.neuron.2007.01.033.

31. Wickersham, I.R., Finke, S., Conzelmann, K.K., and Callaway, E.M. (2007). Retrograde neuronal tracing with a deletion-mutant rabies virus. Nat. Methods *4*, 47–49. https://doi.org/10.1038/Nmeth999.

32. Sun, Y., Nguyen, A.Q., Nguyen, J.P., Le, L., Saur, D., Choi, J., Callaway, E.M., and Xu, X. (2014). Cell-type-specific circuit connectivity of hippocampal CA1 revealed through Cre-dependent rabies tracing. Cell Rep. *7*, 269–280. https://doi.org/10.1016/j.celrep.2014.02.030.

33. Reardon, T.R., Murray, A.J., Turi, G.F., Wirblich, C., Croce, K.R., Schnell, M.J., Jessell, T.M., and Losonczy, A. (2016). Rabies Virus CVS-N2c$^{\Delta G}$ Strain Enhances Retrograde Synaptic Transfer and Neuronal Viability. Neuron *89*, 711–724. https://doi.org/10.1016/j.neuron.2016.01.004.

34. Südhof, T.C., and Malenka, R.C. (2008). Understanding synapses: past, present, and future. Neuron *60*, 469–476. https://doi.org/10.1016/j.neuron.2008.10.011.

35. Bergles, D.E., Roberts, J.D.B., Somogyi, P., and Jahr, C.E. (2000). Glutamatergic synapses on oligodendrocyte precursor cells in the hippocampus. Nature *405*, 187–191. https://doi.org/10.1038/35012083.

36. Miyamichi, K., Amat, F., Moussavi, F., Wang, C., Wickersham, I., Wall, N.R., Taniguchi, H., Tasic, B., Huang, Z.J., He, Z.G., et al. (2011). Cortical

representations of olfactory input by trans-synaptic tracing. Nature *472*, 191–196. https://doi.org/10.1038/nature09714.

37. Schwarz, L.A., Miyamichi, K., Gao, X.J.J., Beier, K.T., Weissbourd, B., DeLoach, K.E., Ren, J., Ibanes, S., Malenka, R.C., Kremer, E.J., et al. (2015). Viral-genetic tracing of the input-output organization of a central noradrenaline circuit. Nature *524*, 88–92. https://doi.org/10.1038/nature14600.
38. Stephenson-Jones, M., Yu, K., Ahrens, S., Tucciarone, J.M., van Huijstee, A.N., Mejia, L.A., Penzo, M.A., Tai, L.H., Wilbrecht, L., and Li, B. (2016). A basal ganglia circuit for evaluating action outcomes. Nature *539*, 289–293. https://doi.org/10.1038/nature19845.
39. Wu, X.T., Morishita, W., Beier, K.T., Heifets, B.D., and Malenka, R.C. (2021). 5-HT modulation of a medial septal circuit tunes social memory stability. Nature *599*, 96–101. https://doi.org/10.1038/s41586-021-03956-8.
40. Siu, C., Balsor, J., Merlin, S., Federer, F., and Angelucci, A. (2021). A direct interareal feedback-to-feedforward circuit in primate visual cortex. Nat. Commun. *12*, 4911. https://doi.org/10.1038/s41467-021-24928-6.
41. Foster, N.N., Barry, J., Korobkova, L., Garcia, L., Gao, L., Becerra, M., Sherafat, Y., Peng, B., Li, X.N., Choi, J.H., et al. (2021). The mouse cortico-basal ganglia-thalamic network. Nature *598*, 188–194. https://doi.org/10.1038/s41586-021-03993-3.
42. Yao, S.Q., Wang, Q.X., Hirokawa, K.E., Ouellette, B., Ahmed, R., Bomben, J., Brouner, K., Casal, L., Caldejon, S., Cho, A., et al. (2023). A whole-brain monosynaptic input connectome to neuron classes in mouse visual cortex. Nat. Neurosci. *26*, 350–364. https://doi.org/10.1038/s41593-022-01219-x.
43. Wertz, A., Trenholm, S., Yonehara, K., Hillier, D., Raics, Z., Leinweber, M., Szalay, G., Ghanem, A., Keller, G., Rózsa, B., et al. (2015). PRESYNAPTIC NETWORKS. Single-cell-initiated monosynaptic tracing reveals layer-specific cortical network modules. Science *349*, 70–74. https://doi.org/10.1126/science.aab1687.
44. Mount, C.W., Yalçın, B., Cunliffe-Koehler, K., Sundaresh, S., and Monje, M. (2019). Monosynaptic tracing maps brain-wide afferent oligodendrocyte precursor cell connectivity. eLife *8*, e49291. https://doi.org/10.7554/eLife.49291.
45. John Lin, C.C., Yu, K., Hatcher, A., Huang, T.W., Lee, H.K., Carlson, J., Weston, M.C., Chen, F., Zhang, Y., Zhu, W., et al. (2017). Identification of diverse astrocyte populations and their malignant analogs. Nat. Neurosci. *20*, 396–405. https://doi.org/10.1038/nn.4493.
46. Buckingham, S.C., Campbell, S.L., Haas, B.R., Montana, V., Robel, S., Ogunrinu, T., and Sontheimer, H. (2011). Glutamate release by primary brain tumors induces epileptic activity. Nat. Med. *17*, 1269–1274. https://doi.org/10.1038/nm.2453.
47. Hatcher, A., Yu, K., Meyer, J., Aiba, I., Deneen, B., and Noebels, J.L. (2020). Pathogenesis of peritumoral hyperexcitability in an immunocompetent CRISPR-based glioblastoma model. J. Clin. Invest. *130*, 2286–2300. https://doi.org/10.1172/JCI133316.
48. Campbell, S.L., Robel, S., Cuddapah, V.A., Robert, S., Buckingham, S.C., Kahle, K.T., and Sontheimer, H. (2015). GABAergic disinhibition and impaired KCC2 cotransporter activity underlie tumor-associated epilepsy. Glia *63*, 23–36. https://doi.org/10.1002/glia.22730.
49. Yu, K., Lin, C.J., Hatcher, A., Lozzi, B., Kong, K., Huang-Hobbs, E., Cheng, Y.T., Beechar, V.B., Zhu, W., Zhang, Y., et al. (2020). PIK3CA variants selectively initiate brain hyperactivity during gliomagenesis. Nature *578*, 166–171. https://doi.org/10.1038/s41586-020-1952-2.
50. Lemke, D., Weiler, M., Blaes, J., Wiestler, B., Jestaedt, L., Klein, A.C., Löw, S., Eisele, G., Radlwimmer, B., Capper, D., et al. (2014). Primary glioblastoma cultures: can profiling of stem cell markers predict radiotherapy sensitivity? J. Neurochem. *131*, 251–264. https://doi.org/10.1111/jnc.12802.
51. Xie, Y., Bergström, T., Jiang, Y., Johansson, P., Marinescu, V.D., Lindberg, N., Segerman, A., Wicher, G., Niklasson, M., Baskaran, S., et al. (2015). The Human Glioblastoma Cell Culture Resource: Validated Cell Models Representing All Molecular Subtypes. EBioMedicine *2*, 1351–1363. https://doi.org/10.1016/j.ebiom.2015.08.026.
52. Abremski, K., and Hoess, R. (1984). Bacteriophage P1 site-specific recombination. Purification and properties of the Cre recombinase protein. J. Biol. Chem. *259*, 1509–1514.
53. Ravi, V.M., Joseph, K., Wurm, J., Behringer, S., Garrelfs, N., d'Errico, P., Naseri, Y., Franco, P., Meyer-Luehmann, M., Sankowski, R., et al. (2019). Human organotypic brain slice culture: a novel framework for environmental research in neuro-oncology. Life Sci. Alliance *2*, e201900305. https://doi.org/10.26508/lsa.201900305.
54. Zhang, Y., Pak, C., Han, Y., Ahlenius, H., Zhang, Z., Chanda, S., Marro, S., Patzke, C., Acuna, C., Covy, J., et al. (2013). Rapid single-step induction of functional neurons from human pluripotent stem cells. Neuron *78*, 785–798. https://doi.org/10.1016/j.neuron.2013.05.029.
55. Yuste, R., and Bonhoeffer, T. (2001). Morphological changes in dendritic spines associated with long-term synaptic plasticity. Annu. Rev. Neurosci. *24*, 1071–1089. https://doi.org/10.1146/annurev.neuro.24.1.1071.
56. Vecht, C.J., Kerkhof, M., and Duran-Pena, A. (2014). Seizure prognosis in brain tumors: new insights and evidence-based management. Oncologist *19*, 751–759. https://doi.org/10.1634/theoncologist.2014-0060.
57. Grutzendler, J., Kasthuri, N., and Gan, W.B. (2002). Long-term dendritic spine stability in the adult cortex. Nature *420*, 812–816. https://doi.org/10.1038/nature01276.
58. Majewska, A.K., Newton, J.R., and Sur, M. (2006). Remodeling of synaptic structure in sensory cortical areas in vivo. J. Neurosci. *26*, 3021–3029. https://doi.org/10.1523/JNEUROSCI.4454-05.2006.
59. Holtmaat, A.J.G.D., Trachtenberg, J.T., Wilbrecht, L., Shepherd, G.M., Zhang, X., Knott, G.W., and Svoboda, K. (2005). Transient and persistent dendritic spines in the neocortex in vivo. Neuron *45*, 279–291. https://doi.org/10.1016/j.neuron.2005.01.003.
60. Zuo, Y., Lin, A., Chang, P., and Gan, W.B. (2005). Development of long-term dendritic spine stability in diverse regions of cerebral cortex. Neuron *46*, 181–189. https://doi.org/10.1016/j.neuron.2005.04.001.
61. Drexler, R., Khatri, R., Sauvigny, T., Mohme, M., Maire, C.L., Ryba, A., Zghaibeh, Y., Dührsen, L., Salviano-Silva, A., Lamszus, K., et al. (2024). A prognostic neural epigenetic signature in high-grade glioma. Nat. Med. *30*, 1622–1635. https://doi.org/10.1038/s41591-024-02969-w.
62. Ruiz-Moreno, C., Salas, S.M., Samuelsson, E., Brandner, S., Kranendonk, M.E.G., Nilsson, M., and Stunnenberg, H.G. (2022). Harmonized single-cell landscape, intercellular crosstalk and tumor architecture of glioblastoma. Preprint at bioRxiv. https://doi.org/10.1101/2022.08.27.505439.
63. Karschnia, P., Young, J.S., Dono, A., Häni, L., Sciortino, T., Bruno, F., Juenger, S.T., Teske, N., Morshed, R.A., Haddad, A.F., et al. (2023). Prognostic validation of a new classification system for extent of resection in glioblastoma: A report of the RANO resect group. Neuro. Oncol *25*, 940–954. https://doi.org/10.1093/neuonc/noac193.
64. Ashburner, M., Ball, C.A., Blake, J.A., Botstein, D., Butler, H., Cherry, J.M., Davis, A.P., Dolinski, K., Dwight, S.S., Eppig, J.T., et al. (2000). Gene ontology: tool for the unification of biology. The Gene Ontology Consortium. Nat. Genet. *25*, 25–29. https://doi.org/10.1038/75556.
65. Gene Ontology Consortium, Aleksander, S.A., Balhoff, J., Carbon, S., Cherry, J.M., Drabkin, H.J., Ebert, D., Feuermann, M., Gaudet, P., Harris, N.L., et al. (2023). The Gene Ontology knowledgebase in 2023. Genetics *224*, iyad031. https://doi.org/10.1093/genetics/iyad031.
66. Yu, K., Hu, Y.Q., Wu, F., Guo, Q.F., Qian, Z.H., Hu, W.E., Chen, J., Wang, K.Y., Fan, X.Y., Wu, X.L., et al. (2020). Surveying brain tumor heterogeneity by single-cell RNA-sequencing of multi-sector biopsies. Natl. Sci. Rev. *7*, 1306–1318. https://doi.org/10.1093/nsr/nwaa099.
67. Larjavaara, S., Mäntylä, R., Salminen, T., Haapasalo, H., Raitanen, J., Jääskeläinen, J., and Auvinen, A. (2007). Incidence of gliomas by

anatomic location. Neuro. Oncol *9*, 319–325. https://doi.org/10.1215/15228517-2007-016.

68. Lanciego, J.L., Luquin, N., and Obeso, J.A. (2012). Functional neuroanatomy of the basal ganglia. Cold Spring Harb. Perspect. Med. *2*, a009621. https://doi.org/10.1101/cshperspect.a009621.
69. Muñoz-Castañeda, R., Zingg, B., Matho, K.S., Chen, X., Wang, Q., Foster, N.N., Li, A., Narasimhan, A., Hirokawa, K.E., Huo, B., et al. (2021). Cellular anatomy of the mouse primary motor cortex. Nature *598*, 159–166. https://doi.org/10.1038/s41586-021-03970-w.
70. Luo, P., Li, A., Zheng, Y., Han, Y., Tian, J., Xu, Z., Gong, H., and Li, X. (2019). Whole Brain Mapping of Long-Range Direct Input to Glutamatergic and GABAergic Neurons in Motor Cortex. Front. Neuroanat. *13*, 44. https://doi.org/10.3389/fnana.2019.00044.
71. Johansson, Y., and Silberberg, G. (2020). The Functional Organization of Cortical and Thalamic Inputs onto Five Types of Striatal Neurons Is Determined by Source and Target Cell Identities. Cell Rep. *30*, 1178–1194.e3. https://doi.org/10.1016/j.celrep.2019.12.095.
72. Harris, J.A., Mihalas, S., Hirokawa, K.E., Whitesell, J.D., Choi, H., Bernard, A., Bohn, P., Caldejon, S., Casal, L., Cho, A., et al. (2019). Hierarchical organization of cortical and thalamic connectivity. Nature *575*, 195–202. https://doi.org/10.1038/s41586-019-1716-z.
73. Drumm, M.R., Dixit, K.S., Grimm, S., Kumthekar, P., Lukas, R.V., Raizer, J.J., Stupp, R., Chheda, M.G., Kam, K.L., McCord, M., et al. (2020). Extensive brainstem infiltration, not mass effect, is a common feature of end-stage cerebral glioblastomas. Neuro. Oncol *22*, 470–479. https://doi.org/10.1093/neuonc/noz216.
74. Wang, L., Jung, J., Babikir, H., Shamardani, K., Jain, S., Feng, X., Gupta, N., Rosi, S., Chang, S., Raleigh, D., et al. (2022). A single-cell atlas of glioblastoma evolution under therapy reveals cell-intrinsic and cell-extrinsic therapeutic targets. Nat. Cancer *3*, 1534–1552. https://doi.org/10.1038/s43018-022-00475-x.
75. Rades, D., Witteler, J., Trillenberg, P., Olbrich, D., Schild, S.E., Tvilsted, S., and Kjaer, T.W. (2022). Increasing Seizure Activity During Radiation Treatment for High-grade Gliomas - Final Results of a Prospective Interventional Study. In Vivo *36*, 2308–2313. https://doi.org/10.21873/invivo.12961.
76. Bouwman, J., Maia, A.S., Camoletto, P.G., Posthuma, G., Roubos, E.W., Oorschot, V.M., Klumperman, J., and Verhage, M. (2004). Quantification of synapse formation and maintenance in vivo in the absence of synaptic release. Neuroscience *126*, 115–126. https://doi.org/10.1016/j.neuroscience.2004.03.027.
77. Katz, L.C., and Shatz, C.J. (1996). Synaptic activity and the construction of cortical circuits. Science *274*, 1133–1138. https://doi.org/10.1126/science.274.5290.1133.
78. Rogawski, M.A., and Hanada, T. (2013). Preclinical pharmacology of perampanel, a selective non-competitive AMPA receptor antagonist. Acta Neurol. Scand. Suppl. *197*, 19–24. https://doi.org/10.1111/ane.12100.
79. Gray, D.C., Mahrus, S., and Wells, J.A. (2010). Activation of specific apoptotic caspases with an engineered small-molecule-activated protease. Cell *142*, 637–646. https://doi.org/10.1016/j.cell.2010.07.014.
80. Yang, C.F., Chiang, M.C., Gray, D.C., Prabhakaran, M., Alvarado, M., Juntti, S.A., Unger, E.K., Wells, J.A., and Shah, N.M. (2013). Sexually dimorphic neurons in the ventromedial hypothalamus govern mating in both sexes and aggression in males. Cell *153*, 896–909. https://doi.org/10.1016/j.cell.2013.04.017.
81. Venkatesh, H.S., Johung, T.B., Caretti, V., Noll, A., Tang, Y.J., Nagaraja, S., Gibson, E.M., Mount, C.W., Polepalli, J., Mitra, S.S., et al. (2015). Neuronal Activity Promotes Glioma Growth through Neuroligin-3 Secretion. Cell *161*, 803–816. https://doi.org/10.1016/j.cell.2015.04.012.
82. Venkatesh, H.S., Tam, L.T., Woo, P.J., Lennon, J., Nagaraja, S., Gillespie, S.M., Ni, J., Duveau, D.Y., Morris, P.J., Zhao, J.J., et al. (2017). Targeting neuronal activity-regulated neuroligin-3 dependency in high-grade glioma. Nature *549*, 533–537. https://doi.org/10.1038/nature24014.
83. Aabedi, A.A., Lipkin, B., Kaur, J., Kakaizada, S., Valdivia, C., Reihl, S., Young, J.S., Lee, A.T., Krishna, S., Berger, M.S., et al. (2021). Functional alterations in cortical processing of speech in glioma-infiltrated cortex. Proc. Natl. Acad. Sci. USA *118*, e2108959118. https://doi.org/10.1073/pnas.2108959118.
84. Mauffrey, P., Tchitchek, N., Barroca, V., Bemelmans, A.P., Firlej, V., Allory, Y., Roméo, P.H., and Magnon, C. (2019). Progenitors from the central nervous system drive neurogenesis in cancer. Nature *569*, 672–678. https://doi.org/10.1038/s41586-019-1219-y.
85. Zhao, C., Teng, E.M., Summers, R.G., Jr., Ming, G.L., and Gage, F.H. (2006). Distinct morphological stages of dentate granule neuron maturation in the adult mouse hippocampus. J. Neurosci. *26*, 3–11. https://doi.org/10.1523/JNEUROSCI.3648-05.2006.
86. Huang, K.W., and Sabatini, B.L. (2020). Single-Cell Analysis of Neuroinflammatory Responses Following Intracranial Injection of G-Deleted Rabies Viruses. Front. Cell. Neurosci. *14*, 65. https://doi.org/10.3389/fncel.2020.00065.
87. Jin, L., Sullivan, H.A., Zhu, M., Lavin, T.K., Matsuyama, M., Fu, X., Lea, N.E., Xu, R., Hou, Y., Rutigliani, L., et al. (2024). Long-term labeling and imaging of synaptically connected neuronal networks in vivo using double-deletion-mutant rabies viruses. Nat. Neurosci. *27*, 373–383. https://doi.org/10.1038/s41593-023-01545-8.
88. Jin, L., Sullivan, H.A., Zhu, M., Lea, N.E., Lavin, T.K., Fu, X., Matsuyama, M., Hou, Y., Feng, G., and Wickersham, I.R. (2023). Third-generation rabies viral vectors allow nontoxic retrograde targeting of projection neurons with greatly increased efficiency. Cell Rep. Methods *3*, 100644. https://doi.org/10.1016/j.crmeth.2023.100644.
89. Callaway, E.M., and Luo, L. (2015). Monosynaptic Circuit Tracing with Glycoprotein-Deleted Rabies Viruses. J. Neurosci. *35*, 8979–8985. https://doi.org/10.1523/JNEUROSCI.0409-15.2015.
90. Rogers, A., and Beier, K.T. (2021). Can transsynaptic viral strategies be used to reveal functional aspects of neural circuitry? J. Neurosci. Methods *348*, 109005. https://doi.org/10.1016/j.jneumeth.2020.109005.
91. De Paola, V., Arber, S., and Caroni, P. (2003). AMPA receptors regulate dynamic equilibrium of presynaptic terminals in mature hippocampal networks. Nat. Neurosci. *6*, 491–500. https://doi.org/10.1038/nn1046.
92. Dondzillo, A., Sätzler, K., Horstmann, H., Altrock, W.D., Gundelfinger, E.D., and Kuner, T. (2010). Targeted three-dimensional immunohistochemistry reveals localization of presynaptic proteins Bassoon and Piccolo in the rat calyx of Held before and after the onset of hearing. J. Comp. Neurol. *518*, 1008–1029. https://doi.org/10.1002/cne.22260.
93. Dana, H., Sun, Y., Mohar, B., Hulse, B.K., Kerlin, A.M., Hasseman, J.P., Tsegaye, G., Tsang, A., Wong, A., Patel, R., et al. (2019). High-performance calcium sensors for imaging activity in neuronal populations and microcompartments. Nat. Methods *16*, 649–657. https://doi.org/10.1038/s41592-019-0435-6.
94. Sun, Y., Wang, X., Zhang, D.Y., Zhang, Z., Bhattarai, J.P., Wang, Y., Dong, W., Zhang, F., Park, K.H., Galanaugh, J., et al. (2024). Brain-wide neuronal circuit connectome of human glioblastoma. Preprint at bioRxiv. https://doi.org/10.1101/2024.03.01.583047.
95. Schindelin, J., Arganda-Carreras, I., Frise, E., Kaynig, V., Longair, M., Pietzsch, T., Preibisch, S., Rueden, C., Saalfeld, S., Schmid, B., et al. (2012). Fiji: an open-source platform for biological-image analysis. Nat. Methods *9*, 676–682. https://doi.org/10.1038/nmeth.2019.
96. R Core Team (2023). R: A Language and Environment for Statistical Computing (R Foundation for Statistical Computing).
97. Berg, S., Kutra, D., Kroeger, T., Straehle, C.N., Kausler, B.X., Haubold, C., Schiegg, M., Ales, J., Beier, T., Rudy, M., et al. (2019). ilastik: interactive machine learning for (bio)image analysis. Nat. Methods *16*, 1226–1232. https://doi.org/10.1038/s41592-019-0582-9.
98. Wang, Y., DelRosso, N.V., Vaidyanathan, T.V., Cahill, M.K., Reitman, M.E., Pittolo, S., Mi, X., Yu, G., and Poskanzer, K.E. (2019). Accurate quantification of astrocyte and neurotransmitter fluorescence dynamics

for single-cell and population-level physiology. Nat. Neurosci. *22*, 1936–1944. https://doi.org/10.1038/s41593-019-0492-2.

99. Ershov, D., Phan, M.S., Pylvänäinen, J.W., Rigaud, S.U., Le Blanc, L., Charles-Orszag, A., Conway, J.R.W., Laine, R.F., Roy, N.H., Bonazzi, D., et al. (2022). TrackMate 7: integrating state-of-the-art segmentation algorithms into tracking pipelines. Nat. Methods *19*, 829–832. https://doi.org/10.1038/s41592-022-01507-1.
100. Kueckelhaus, J., Frerich, S., Kada-Benotmane, J., Koupourtidou, C., Ninkovic, J., Dichgans, M., Beck, J., Schnell, O., and Heiland, D.H. (2024). Inferring histology-associated gene expression gradients in spatial transcriptomic studies. Nat. Commun. *15*, 7280. https://doi.org/10.1038/s41467-024-50904-x.
101. Hai, L., Hoffmann, D.C., Wagener, R.J., Azorin, D.D., Hausmann, D., Xie, R., Huppertz, M.-C., Hiblot, J., Sievers, P., Heuer, S., et al. (2024). A clinically applicable connectivity signature for glioblastoma includes the tumor network driver CHI3L1. Nat Commun *15*, 968. https://doi.org/10.1038/s41467-024-45067-8.
102. Yin, L., Geng, Y., Osakada, F., Sharma, R., Cetin, A.H., Callaway, E.M., Williams, D.R., and Merigan, W.H. (2013). Imaging light responses of retinal ganglion cells in the living mouse eye. J. Neurophysiol. *109*, 2415–2421. https://doi.org/10.1152/jn.01043.2012.
103. Weil, S., Osswald, M., Solecki, G., Grosch, J., Jung, E., Lemke, D., Ratliff, M., Hänggi, D., Wick, W., and Winkler, F. (2017). Tumor microtubes convey resistance to surgical lesions and chemotherapy in gliomas. Neuro. Oncol *19*, 1316–1326. https://doi.org/10.1093/neuonc/nox070.
104. Osswald, M. (2015). Nanotechnology and Oral Implants: An Update. Int. J. Oral Maxillofac. Implants *30*, 995–997.
105. Dondzillo, A., Sätzler, K., Horstmann, H., Altrock, W.D., Gundelfinger, E.D., and Kuner, T. (2010). Targeted three-dimensional immunohistochemistry reveals localization of presynaptic proteins Bassoon and Piccolo in the rat calyx of Held before and after the onset of hearing. J. Comp. Neurol. *518*, 1008–1029. https://doi.org/10.1002/cne.22260.
106. Capper, D., Jones, D.T.W., Sill, M., Hovestadt, V., Schrimpf, D., Sturm, D., Koelsche, C., Sahm, F., Chavez, L., Reuss, D.E., et al. (2018). DNA methylation-based classification of central nervous system tumours. Nature *555*, 469–474. https://doi.org/10.1038/nature26000.
107. Straehle, J., Ravi, V.M., Heiland, D.H., Galanis, C., Lenz, M., Zhang, J., Neidert, N.N., El Rahal, A., Vasilikos, I., Kellmeyer, P., et al. (2023). Technical report: surgical preparation of human brain tissue for clinical and basic research. Acta Neurochir. (Wien) *165*, 1461–1471. https://doi.org/10.1007/s00701-023-05611-9.
108. Neidert, N., Straehle, J., Erny, D., Sacalean, V., El Rahal, A., Steybe, D., Schmelzeisen, R., Vlachos, A., Reinacher, P.C., Coenen, V.A., et al. (2022). Stimulated Raman histology in the neurosurgical workflow of a major European neurosurgical center - part A. Neurosurg. Rev. *45*, 1731–1739. https://doi.org/10.1007/s10143-021-01712-0.
109. Ravi, V.M., Will, P., Kueckelhaus, J., Sun, N., Joseph, K., Salié, H., Vollmer, L., Kuliesiute, U., von Ehr, J., Benotmane, J.K., et al. (2022). Spatially resolved multi-omics deciphers bidirectional tumor-host interdependence in glioblastoma. Cancer Cell *40*, 639–655.e13. https://doi.org/10.1016/j.ccell.2022.05.009.
110. Ravi, V.M., Neidert, N., Will, P., Joseph, K., Maier, J.P., Kückelhaus, J., Vollmer, L., Goeldner, J.M., Behringer, S.P., Scherer, F., et al. (2022). T-cell dysfunction in the glioblastoma microenvironment is mediated by myeloid cells releasing interleukin-10. Nat. Commun. *13*, 925. https://doi.org/10.1038/s41467-022-28523-1.
111. Kuliesiute, U., Joseph, K., Straehle, J., Madapusi Ravi, V., Kueckelhaus, J., Kada Benotmane, J., Zhang, J., Vlachos, A., Beck, J., Schnell, O., et al. (2023). Sialic acid metabolism orchestrates transcellular connectivity and signaling in glioblastoma. Neuro. Oncol *25*, 1963–1975. https://doi.org/10.1093/neuonc/noad101.
112. Schneider, M., Vollmer, L., Potthoff, A.L., Ravi, V.M., Evert, B.O., Rahman, M.A., Sarowar, S., Kueckelhaus, J., Will, P., Zurhorst, D., et al. (2021). Meclofenamate causes loss of cellular tethering and decoupling of functional networks in glioblastoma. Neuro. Oncol *23*, 1885–1897. https://doi.org/10.1093/neuonc/noab092.
113. Carpenter, A.E., Jones, T.R., Lamprecht, M.R., Clarke, C., Kang, I.H., Friman, O., Guertin, D.A., Chang, J.H., Lindquist, R.A., Moffat, J., et al. (2006). CellProfiler: image analysis software for identifying and quantifying cell phenotypes. Genome Biol. *7*, R100. https://doi.org/10.1186/gb-2006-7-10-r100.
114. Kleshchevnikov, V., Shmatko, A., Dann, E., Aivazidis, A., King, H.W., Li, T., Elmentaite, R., Lomakin, A., Kedlian, V., Gayoso, A., et al. (2022). Cell2location maps fine-grained cell types in spatial transcriptomics. Nat. Biotechnol. *40*, 661–671. https://doi.org/10.1038/s41587-021-01139-4.
115. Huff, J. (2015). The Airyscan detector from ZEISS: confocal imaging with improved signal-to-noise ratio and super-resolution. Nat. Methods *12*. i-ii. https://doi.org/10.1038/nmeth.f.388.
116. Wu, X., and Hammer, J.A. (2021). ZEISS Airyscan: Optimizing Usage for Fast, Gentle, Super-Resolution Imaging. Methods Mol. Biol. *2304*, 111–130. https://doi.org/10.1007/978-1-0716-1402-0_5.
117. Maiti, P., Manna, J., Ilavazhagan, G., Rossignol, J., and Dunbar, G.L. (2015). Molecular regulation of dendritic spine dynamics and their potential impact on synaptic plasticity and neurological diseases. Neurosci. Biobehav. Rev. *59*, 208–237. https://doi.org/10.1016/j.neubiorev.2015.09.020.
118. Pitzer, C., Kurpiers, B., and Eltokhi, A. (2021). Gait performance of adolescent mice assessed by the CatWalk XT depends on age, strain and sex and correlates with speed and body weight. Sci. Rep. *11*, 21372. https://doi.org/10.1038/s41598-021-00625-8.
119. Pitzer, C., Kuner, R., and Tappe-Theodor, A. (2016). Voluntary and evoked behavioral correlates in inflammatory pain conditions under different social housing conditions. PAIN Rep. *1*, e564. https://doi.org/10.1097/PR9.0000000000000564.
120. Eltokhi, A., Kurpiers, B., and Pitzer, C. (2020). Behavioral tests assessing neuropsychiatric phenotypes in adolescent mice reveal strain- and sex-specific effects. Sci. Rep. *10*, 11263. https://doi.org/10.1038/s41598-020-67758-0.
121. Schnitzler, A.C., Lopez-Coviella, I., and Blusztajn, J.K. (2008). Purification and culture of nerve growth factor receptor (p75)-expressing basal forebrain cholinergic neurons. Nat. Protoc. *3*, 34–40. https://doi.org/10.1038/nprot.2007.477.
122. Patzke, C., Brockmann, M.M., Dai, J., Gan, K.J., Grauel, M.K., Fenske, P., Liu, Y., Acuna, C., Rosenmund, C., and Südhof, T.C. (2019). Neuromodulator Signaling Bidirectionally Controls Vesicle Numbers in Human Synapses. Cell *179*, 498–513.e22. https://doi.org/10.1016/j.cell.2019.09.011.
123. Stringer, C., Wang, T., Michaelos, M., and Pachitariu, M. (2021). Cellpose: a generalist algorithm for cellular segmentation. Nat. Methods *18*, 100–106. https://doi.org/10.1038/s41592-020-01018-x.
124. Pachitariu, M., and Stringer, C. (2022). Cellpose 2.0: how to train your own model. Nat. Methods *19*, 1634–1641. https://doi.org/10.1038/s41592-022-01663-4.
125. Stringer, C., and Pachitariu, M. (2024). Cellpose3: one-click image restoration for improved cellular segmentation. Preprint at bioRxiv. https://doi.org/10.1101/2024.02.10.579780.
126. Kreshuk, A., and Zhang, C. (2019). Machine Learning: Advanced Image Segmentation Using ilastik. Methods Mol. Biol. *2040*, 449–463. https://doi.org/10.1007/978-1-4939-9686-5_21.
127. Tu, Z., and Bai, X. (2010). Auto-context and its application to high-level vision tasks and 3D brain image segmentation. IEEE Trans. Pattern Anal. Mach. Intell. *32*, 1744–1757. https://doi.org/10.1109/TPAMI.2009.186.
128. Osakada, F., Mori, T., Cetin, A.H., Marshel, J.H., Virgen, B., and Callaway, E.M. (2011). New rabies virus variants for monitoring and

manipulating activity and gene expression in defined neural circuits. Neuron *71*, 617–631. https://doi.org/10.1016/j.neuron.2011.07.005.

129. Hao, Y., Stuart, T., Kowalski, M.H., Choudhary, S., Hoffman, P., Hartman, A., Srivastava, A., Molla, G., Madad, S., Fernandez-Granda, C., et al. (2024). Dictionary learning for integrative, multimodal and scalable single-cell analysis. Nat. Biotechnol. *42*, 293–304. https://doi.org/10.1038/s41587-023-01767-y.

130. Cox, D.R. (1972). Regression Models and Life-Tables. J. R. Stat. Soc. Series B Stat. Methodol. *34*, 187–202. https://doi.org/10.1111/j.2517-6161.1972.tb00899.x.

131. Brennan, C.W., Verhaak, R.G.W., McKenna, A., Campos, B., Noushmehr, H., Salama, S.R., Zheng, S., Chakravarty, D., Sanborn, J.Z., Berman, S.H., et al. (2013). The somatic genomic landscape of glioblastoma. Cell *155*, 462–477. https://doi.org/10.1016/j.cell.2013.09.034.

132. Chan, K.Y., Jang, M.J., Yoo, B.B., Greenbaum, A., Ravi, N., Wu, W.L., Sánchez-Guardado, L., Lois, C., Mazmanian, S.K., Deverman, B.E., et al. (2017). Engineered AAVs for efficient noninvasive gene delivery to the central and peripheral nervous systems. Nat. Neurosci. *20*, 1172–1179. https://doi.org/10.1038/nn.4593.

133. Asano, S.M., Gao, R., Wassie, A.T., Tillberg, P.W., Chen, F., and Boyden, E.S. (2018). Expansion Microscopy: Protocols for Imaging Proteins and RNA in Cells and Tissues. Curr. Protoc. Cell Biol. *80*, e56. https://doi.org/10.1002/cpcb.56.

134. Renier, N., Wu, Z., Simon, D.J., Yang, J., Ariel, P., and Tessier-Lavigne, M. (2014). iDISCO: a simple, rapid method to immunolabel large tissue samples for volume imaging. Cell *159*, 896–910. https://doi.org/10.1016/j.cell.2014.10.010.

135. Pan, C., Schoppe, O., Parra-Damas, A., Cai, R., Todorov, M.I., Gondi, G., von Neubeck, B., Böğürcü-Seidel, N., Seidel, S., Sleiman, K., et al. (2019). Deep Learning Reveals Cancer Metastasis and Therapeutic Antibody Targeting in the Entire Body. Cell *179*, 1661–1676.e19. https://doi.org/10.1016/j.cell.2019.11.013.

136. Dana, H., Mohar, B., Sun, Y., Narayan, S., Gordus, A., Hasseman, J.P., Tsegaye, G., Holt, G.T., Hu, A., Walpita, D., et al. (2016). Sensitive red protein calcium indicators for imaging neural activity. eLife *5*, e12727. https://doi.org/10.7554/eLife.12727.

137. Romanos, J., Benke, D., Saab, A.S., Zeilhofer, H.U., and Santello, M. (2019). Differences in glutamate uptake between cortical regions impact neuronal NMDA receptor activation. Commun. Biol. *2*, 127. https://doi.org/10.1038/s42003-019-0367-9.

138. Zhou, W.L., Gao, X.B., and Picciotto, M.R. (2015). Acetylcholine Acts through Nicotinic Receptors to Enhance the Firing Rate of a Subset of Hypocretin Neurons in the Mouse Hypothalamus through Distinct Presynaptic and Postsynaptic Mechanisms. eNeuro *2*, ENEURO.0052-14.2015. https://doi.org/10.1523/ENEURO.0052-14.2015.

139. Kirmse, K., Kummer, M., Kovalchuk, Y., Witte, O.W., Garaschuk, O., and Holthoff, K. (2015). GABA depolarizes immature neurons and inhibits network activity in the neonatal neocortex in vivo. Nat. Commun. *6*, 7750. https://doi.org/10.1038/ncomms8750.

140. Dou, Y., Wu, H.J., Li, H.Q., Qin, S., Wang, Y.E., Li, J., Lou, H.F., Chen, Z., Li, X.M., Luo, Q.M., et al. (2012). Microglial migration mediated by ATP-induced ATP release from lysosomes. Cell Res. *22*, 1022–1033. https://doi.org/10.1038/cr.2012.10.

141. Petersen, A.V., Jensen, C.S., Crépel, V., Falkerslev, M., and Perrier, J.F. (2017). Serotonin Regulates the Firing of Principal Cells of the Subiculum by Inhibiting a T-type Ca^{2+} Current. Front. Cell. Neurosci. *11*, 60. https://doi.org/10.3389/fncel.2017.00060.

142. Kim, Y., and Trussell, L.O. (2009). Negative shift in the glycine reversal potential mediated by a Ca2+- and pH-dependent mechanism in interneurons. J. Neurosci. *29*, 11495–11510. https://doi.org/10.1523/JNEUROSCI.1086-09.2009.

143. Zhou, W.L., and Antic, S.D. (2012). Rapid dopaminergic and GABAergic modulation of calcium and voltage transients in dendrites of prefrontal cortex pyramidal neurons. J. Physiol. *590*, 3891–3911. https://doi.org/10.1113/jphysiol.2011.227157.

144. Bakkum, D.J., Frey, U., Radivojevic, M., Russell, T.L., Müller, J., Fiscella, M., Takahashi, H., and Hierlemann, A. (2013). Tracking axonal action potential propagation on a high-density microelectrode array across hundreds of sites. Nat. Commun. *4*, 2181. https://doi.org/10.1038/ncomms3181.

145. Ester, M., Kriegel, H.-P., Sander, J., and Xu, X. (1996). A density-based algorithm for discovering clusters in large spatial databases with noise. In Proceedings of the Second International Conference on Knowledge Discovery and Data Mining (AAAI Press).

146. Yates, S.C., Groeneboom, N.E., Coello, C., Lichtenthaler, S.F., Kuhn, P.H., Demuth, H.U., Hartlage-Rübsamen, M., Roßner, S., Leergaard, T., Kreshuk, A., et al. (2019). QUINT: Workflow for Quantification and Spatial Analysis of Features in Histological Images From Rodent Brain. Front. Neuroinform. *13*, 75. https://doi.org/10.3389/fninf.2019.00075.

147. Wang, Q., Ding, S.L., Li, Y., Royall, J., Feng, D., Lesnar, P., Graddis, N., Naeemi, M., Facer, B., Ho, A., et al. (2020). The Allen Mouse Brain Common Coordinate Framework: A 3D Reference Atlas. Cell *181*, 936–953.e20. https://doi.org/10.1016/j.cell.2020.04.007.

148. Puchades, M.A., Csucs, G., Ledergerber, D., Leergaard, T.B., and Bjaalie, J.G. (2019). Spatial registration of serial microscopic brain images to three-dimensional reference atlases with the QuickNII tool. PLoS One *14*, e0216796. https://doi.org/10.1371/journal.pone.0216796.

149. Groeneboom, N.E., Yates, S.C., Puchades, M.A., and Bjaalie, J.G. (2020). Nutil: A Pre- and Post-processing Toolbox for Histological Rodent Brain Section Images. Front. Neuroinform. *14*, 37. https://doi.org/10.3389/fninf.2020.00037.

150. Zhang, M., Pan, X., Jung, W., Halpern, A.R., Eichhorn, S.W., Lei, Z., Cohen, L., Smith, K.A., Tasic, B., Yao, Z., et al. (2023). Molecularly defined and spatially resolved cell atlas of the whole mouse brain. Nature *624*, 343–354. https://doi.org/10.1038/s41586-023-06808-9.

STAR★METHODS

KEY RESOURCES TABLE

REAGENT or RESOURCE	SOURCE	IDENTIFIER
Antibodies		
Mouse monoclonal anti-beta-III-tubulin	Abcam	Cat#ab7751; RRID:AB_306045
Guinea pig polyclonal anti-NeuN	Synaptic Systems	Cat#266004; RRID:AB_2619988
Rabbit polyclonal anti-VAChT	Synaptic Systems	Cat#139103; RRID:AB_887864
Guinea pig polyclonal anti- VAChT	Synaptic Systems	Cat#139 105; RRID:AB_10893979
Chicken polyclonal anti-S100B	Synaptic Systems	Cat#287006; RRID:AB_2713986
Rat monoclonal anti-MBP	Novus Biologicals	Cat#NB600-717; RRID:AB_2139899
Rabbit polyclonal anti-Iba1	FUJIFILM Wako Pure Chemical Corporation	Cat# 019-19741; RRID:AB_839504
Mouse monoclonal anti-nestin	Abcam	Cat#ab22035; RRID:AB_446723
Chicken polyclonal anti-GFP	Abcam	Cat#ab13970; RRID:AB_300798
Chicken polyclonal anti-GFP	Aves Labs	Cat#GFP-1020; RRID:AB_10000240
Rabbit polyclonal anti-RFP, pre-adsorbed	Rockland	Cat#600-401-379; RRID:AB_11182807
Rabbit polyclonal anti-mCherry	Abcam	Cat#ab167453; RRID:AB_2571870
Guinea pig polyclonal anti-RFP	Synaptic Systems	Cat#390004; RRID:AB_2737052
Mouse monoclonal anti-CAMK2	Abcam	Cat#ab22609; RRID:AB_447192
Mouse anti-GAD67	Abcam	Cat#ab26116; RRID:AB_448990
Rabbit polyclonal anti-CHRM3	Thermo Fischer	Cat#AMR-006; RRID:AB_2039997
Guinea pig polyclonal anti-VGAT	SySy	Cat#131 004; RRID:AB_887873
Guinea pig polyclonal anti-DAT	SySy	Cat#284 005; RRID:AB_2620019
Rabbit polyclonal anti-Parvalbumin	Abcam	Cat#ab11427; RRID:AB_298032
Rabbit monoclonal anti-Satb2	Abcam	Cat#ab92446; RRID:AB_10563678
Rabbit polyclonal anti-Olig2	Abcam	Cat#ab109186; RRID:AB_10861310
Rabbit monoclonal anti-Gephyrin	SySy	Cat#147 008; RRID:AB_2619834
Rabbit polyclonal anti-Dopamine D2 Receptor	Millipore	Cat#AB5084P; RRID:AB_2094980
Rabbit polyclonal anti-Dopamine D4 Receptor	Thermo Fischer	Cat#D4R-401AP
Rabbit polyclonal anti-Homer1/2/3	SySy	Cat#160 103; RRID:AB_10694096
Guinea pig polyclonal anti-VGlut1	Millipore	Cat# AB5905; RRID:AB_2301751
Guinea pig polyclonal anti-Synapsin1/2	SySy	Cat#106 004; RRID:AB_1106784
Rabbit polyclonal anti-P2XR7	GeneTex	Cat#GTX104288; RRID:AB_1951086
Rabbit polyclonal anti-cleaved caspase 3	CellSignaling	Cat#9661; RRID:AB_2341188
Goat anti-chicken Alexa488	invitrogen	Cat#1458638 and 2304258; RRID:AB_2534096
Goat anti-rabbit Alexa647	invitrogen	Cat#1981173 and 2299231; RRID:AB_2535813
Goat anti-guinea pig Alexa647	invitrogen	Cat#A-21450; RRID:AB_141882
Goat anti-guinea pig Alexa546	invitrogen	Cat#A11074; RRID:AB_2534118
Goat anti-chicken Alexa647	invitrogen	Cat#A-21449; RRID:AB_2535866
Goat anti-rat Alexa647	invitrogen	Cat#A-21247; RRID:AB_141778
Goat anti-rabbit Alexa568	invitrogen	Cat#A11011; RRID:AB_143157
Goat anti-mouse Alexa647	invitrogen	Cat#A21235; RRID:AB_2535804
Goat anti-mouse Alexa568	invitrogen	Cat#A11011; RRID:AB_144696
Goat anti-chicken Alexa488	invitrogen	Cat#A32931; RRID:AB_2762843
Streptavidin Alexa647 conjugate	Thermo Fischer	Cat#S21374; RRID:AB_2336066
Bacterial and virus strains		
RABV CVS-N2C(deltaG)-EGFP	addgene	#73461; RRID:Addgene_73461
SAD-B19(deltaG)-EGFP	addgene	#32634; RRID:Addgene_32634

(*Continued on next page*)

Continued

REAGENT or RESOURCE	SOURCE	IDENTIFIER
pAAV-mDlx-NLS-mRuby2	addgene	#99130; RRID:Addgene_99130
pAAV-flex-taCasp3-TEVp	addgene	#45580; RRID:Addgene_45580
pSADdG/CreGFP	Charité Viral Vector Core	BR-26
pN2cdG/CreGFP	Charité Viral Vector Core	BR-41a
pAAV.Syn.NES-jRGECO1a.WPRE.SV40	addgene	#100854; RRID:Addgene_100854
pAAV-CaMKIIahChR2(H134R)-mCherry (AAV2)	UNC Vector Core	N/A
pAAV-CaMKIIa-mCherry (AAV2)	addgene	114469- AAV2; RRID:Addgene_114469
pAAV-CamKIIa-ChrimsonR-mScarlet-KV2.1 (AAV 9)	addgene	124651-AAV9; RRID:Addgene_124651
Biological samples		
Patient-derived xenografts (PDX)	This paper	N/A
Chemicals, peptides, and recombinant proteins		
Poly-L-lysine	Sigma	P4707
Neurobasal Medium	Gibco	11570556
Hibernate™-A Medium	Gibco	A1247501
B-27 Supplement for neuronal co-culture	Gibco	17504044
B27 supplement without vitamin A for GB culture	Gibco	12587010
L-glutamine (GlutaMAX™-I (100x))	Gibco	35050038
Antibiotic-Antimycotic (100x)	Gibco	15240062
$MgSO_4$	Sigma-Aldrich	M3409
DMEM/F12 Medium	Gibco	11330032
Insulin solution human	Sigma	I9278
Heparin	Sigma	H4784
EGF	Biotechne	236-EG-200
FGF Recombinant Protein	Life Technologies	PHG0021
FGF Recombinant Protein 1mg	Life Technologies	PHG0023
Accutase Solution	Thermo Fisher Scientific	A1110501
0.05% Trypsin-EDTA (1x)	Gibco	25300-054
2.5% Trypsin (10x)	Gibco	15090-046
NGF	Miltenyi Biotech	130-127-430
mTeSR™ Plus	StemCell Technologies	#100-0276
ReLeaSR	StemCell Technologies	#05872
1% N2 supplement	Gibco	17502048
Minimum Essential Medium from non-essential amino acids	Gibco	11140050
Laminin	Thermo Fisher Scientific	23017015
BDNF	Peprotech	#450-02
NT-3	Peprotech	#450-03
Doxycycline-HCl	Thermo Fisher Scientific	15473189
Cytosine arabinoside	Sigma	#C6645
HyClone FBS	Cytiva	SH30071.03HI
FBS	Anprotec	AC-SM-0041
AcX	invitrogen	A20770
Ammoniumpersulfate	Sigma	A3678
TEMED	Merck	T9281
4-Hydroxy-TEMPO	Merck	176141
Acrylamide	Sigma	A9099
Sodiumacrylate	Sigma	408220
Neurobiotin Tracer	Vector Laboratories	SP-1120

(*Continued on next page*)

Continued

REAGENT or RESOURCE	SOURCE	IDENTIFIER
HEPES	Sigma-Aldrich	7365-45-9
HEPES solution	Sigma-Aldrich	H0887
D-Glucose	Sigma-Aldrich	G8644
N-Methyl-D-Glucamin	Sigma-Aldrich	M2004
ASC acid	Riedel-de-Haën	33034
HI horse serum	ThermoFischer	26050-070
N,N'-Methylenbisacrylamide	Merck	146072
Perampanel	Eisai	N/A
Perampanel	BioCrick	BCC1847; CAS: 380917-97-5
CNQX	MedChemExpress	HY-15066A; CAS: 479347-85-8
NBQX	HelloBio	HB0443; CAS: 479347-86-9
TTX	HelloBio	HB1035; CAS: 18660-81-6
GI254023X	Sigma-Aldrich	SML0789
Gabazine	Tocris	CAS: 104104-50-9
Glutamate	Sigma-Aldrich	G8415
Acetylcholine	Sigma-Aldrich	A6625
5-HT	Sigma-Aldrich	14927
GABA	Sigma-Aldrich	A2129
Adrenaline	Tocris	5169
Dopamine hydrochloride	Sigma-Aldrich	H8502
Glycine	Sigma-Aldrich	G7126
ATP magnesium salt	Sigma-Aldrich	A9187
Alexa Fluor 594 hydrazide sodium salt	invitrogen	A10442
Atropine sodium salt	Sigma-Aldrich	A0132
Dulbecco's Phosphate Buffered Saline	Sigma-Aldrich	D8537
Millicell cell culture inserts 0.4 um	Merck	PICM0RG50
CellTiter-Glo® Luminescent Cell Viability Assay	Promega	G7570
NaCl	Sigma-Aldrich	S7653
KCL	Fluka	60129
NaHCO3	Fluka	71627
NaH2PO4	Fluka	71496
Triton™ X-100	Sigma-Aldrich	T9284
L-glutamine (GlutaMAX™-I (100x))	Gibco	35050-038
Evans Blue	Sigma	E2129
SlowFade™ Gold Antifade Mountant	ThermoFischer	S36936
DAPI	Sigma	D9542
PFA 4%	Roth	P087.3
Sulforhodamine 101 (SR101)	Sigma-Aldrich	S7635
Tetramethylrhodamine isothiocyanate dextran (TRITC)	Sigma-Aldrich	52194
Human WT Probes v2, RHS	10X Genomics	2000657
Human WT Probes v2, LHS	10X Genomics	2000658
Visium CytAssist Spatial Gene Expression for FFPE	10X Genomics	1000520
Dual Index Kit TS Set A, 96 rxns	10X Genomics	PN-1000251
Poly-Prep Slides	Sigma-Aldrich	P0425-72EA
Eosin Y-solution, Alcoholic	Millipore	HT110116
Hematoxylin Solution, Mayer's	Millipore	MHS16
Bluing Reagent, Dako	Agilent	CS70230-2
KAPA SYBR FAST qPCR Master Mix	KAPA Biosystems	KK4600
Qubit 1× dsDNA HS Kit	ThermoFischer	Q33231

(*Continued on next page*)

Continued

REAGENT or RESOURCE	SOURCE	IDENTIFIER
D1000 Reagents	Agilent	5067-5583
D1000 ScreenTape	Agilent	5067-5582
P2 Illumina FlowCell, Reagent Cartridge	Illumina	20046811
Experimental models: Cell lines		
S24	This paper	N/A
BG5	This paper	N/A
BG7	This paper	N/A
P3XX	This paper	N/A
T269	This paper	N/A
GG16	This paper	N/A
U3017MG	Xie et al.[51]	N/A
U3085MG	Xie et al.[51]	N/A
U3047MG	Xie et al.[51]	N/A
U3048MG	Xie et al.[51]	N/A
E2	This paper	N/A
L1	This paper	N/A
NCH644	Cytion	300124
NCH421K	Cytion	300118
Experimental models: Organisms/strains		
NMRI-Foxn1 nu/nu	Charles River and Janvier	BL210203171
WISTAR	Janvier	N/A
C57BL/6	Janvier	N/A
WA01/H1	WiCell	N/A
HD6	Heidelberg University, Heidelberg, Germany	N/A
Recombinant DNA		
Plasmid: pFU-TVA-2A-mCherry-2A-oGlycoprotein	Addgene, This paper	#85225; RRID:Addgene_85225
Plasmid: mGFP	De Paola et al.[91]; Dondzillo et al.[92]	N/A
Plasmid: GCamp7-tdTomato	Dana et al.[93]	N/A
Plasmid: GFP	Osswald et al.[9]	N/A
Plasmid: tdTomato	Osswald et al.[9]	N/A
Plasmid: U6Prom_shCHRM3_SFFVProm_mGFP	Sun et al.[94]	N/A
Plasmid: U6Prom_scrambled_ shCHRM3_SFFVProm_mGFP	Sun et al[94]	N/A
Software and algorithms		
Fiji	Schindelin et al.[95]	https://imagej.nih.gov/ij/
NIS-Elements AR Analysis 5.41.00 64-bit	Nikon	N/A
Arivis Vision4D 3.5.0	arivis AG, Munich, Germany	https://imaging.arivis.com/en/imaging-science/arivis-vision4d
R Studio 1.4	R Core Team[96]	N/A
GraphPad Prism Version 9	GraphPad	RRID:SCR_002798
Adobe Illustrator 28.2 64-bit	Adobe	N/A
ilastik 1.4.0	Berg et al.[97]	https://www.ilastik.org/development.html
AQuA	Wang et al.[98]	N/A
PATCHMASTER Igor Pro 6.21	HEKA	RRID:SCR_000034
DaVinciResolve 18	Blackmagicdesign	https://www.blackmagicdesign.com/de/products/davinciresolve/
TrackMate (version 7.11.1)	Ershov et al.[99]	N/A

(*Continued on next page*)

Continued

REAGENT or RESOURCE	SOURCE	IDENTIFIER
Zen Blue 3.5, 3.7 and 3.9	Zeiss	RRID:SCR_013672
Zen Black 2.3	Zeiss	RRID:SCR_018163
Leica Application Suite X	Leica Microsystems CMS GmbH	https://www.leica-microsystems.com/de/produkte/mikroskop-software/p/leica-las-x-ls/
MATLAB 9.120.1884302	MathWorks	RRID:SCR_001622
Easy Electrophysiology	–	RRID:SCR_021190
pClamp 11	Molecular Devices	RRID_SCR_011323
LABORAS 2.6	Metris b.v.	N/A
AWM	Lafayette Instruments	N/A
Spaceranger v2.1	10X Genomics	https://www.10xgenomics.com/support/software/space-ranger/2.1
SPATA2 v2.04	Kueckelhaus et al.[100]	N/A
Catwalk XT 10.6	Noldus Information technology	RRID:SCR_021262
Single-cell RNA-sequencing datasets		
Human single-cell RNA-sequencing glioblastoma dataset	Neftel et al.[5]	GSE131928
Human single-cell RNA-sequencing glioblastoma dataset	Yu et al.[49,66]	GSE117891
Xenograft single-cell RNA-sequencing glioblastoma datasets	Hai et al.[101]	N/A
Human single-cell RNA-sequencing glioblastoma dataset	Ruiz-Moreno et al.[62]	GSE141946; GSE166418; GSE162631; GSE154795; GSE141383; GSE182109; GSE173278
Deposited data		
Single-cell RNA-seq data of connected^{TUM} neurons from co-culture	This paper	Zenodo: 13958300
Spatial transcriptomics data of rabies-traced human organotypic slice cultures	This paper	Zenodo: 13956432
Other		
Multirad 225 X Ray Irradiation System	Faxitron	BLE1900269
FACSAria Fusion 2 Bernhard Shoor	BD	N/A
FACSAria Fusion Richard Sweet	BD	N/A
FACSymphony S6	BD	N/A

EXPERIMENTAL MODEL AND STUDY PARTICIPANT DETAILS

Human tissues used for organotypic slice cultures were obtained after approval of the local regulatory authorities (ethical codes 23-1233-S1, 23-1234-S1, S-005/2003, and 23-1175-S1). Human patient samples were pseudonymized manually.

Male NMRI nude mice were used for all animal studies involving patient-derived glioblastoma models. All animal procedures were performed in accordance with the institutional laboratory animal research guidelines following approval of the Regierungspräsidium Karlsruhe, Germany. Efforts were made to minimize animal suffering and reduce the number of animals used according to the 3R principles. Mice were routinely checked for clinical endpoint criteria and if they showed marked neurological symptoms or weight loss exceeding 20%, experiments were terminated. No maximum tumor size was defined for the invasive brain tumor models.

METHOD DETAILS

Lentiviral vector and plasmid generation of pFU-TVA-2A-mCherry-2A-oGlycoprotein

To generate lentiviruses expressing, EnvA TVA receptor (TVA), rabies glycoprotein (oG), and mCherry, we sub-cloned TVA-2A-mCherry-2A-oGlycoprotein into a lentiviral vector ('pFU-') using In-Fusion cloning (Takara). TVA-2A-mCherry-2A-oGlycoprotein was amplified from p306 (Zurich virus core), and cloned into a pFU vector using ECORI and BAMHI sites.

Packaging of CVS-N2c$^{\Delta G}$ and SAD-B19$^{\Delta G}$

Rabies viruses used in this study were produced as described previously.[102] Briefly, B7GG cells were transfected by Lipofectamine 3000 (Thermo Fischer) with rabies virus genomic vectors RabV CVS-N2c$^{\Delta G}$-eGFP (Addgene plasmid #73461) or SAD-B19$^{\Delta G}$-eGFP (modified from Addgene plasmid # 32634). Supernatant was collected over several days and the recovered virus was re-transfected in B7GG cells for a final collection step. For pseudotyping, the supernatant containing unpseudotyped viruses and the rabies with the envelope protein EnVA of the Avian Sarcoma and Leukosis virus were applied on BHK-EnVA cells. 3-5 days later, the EnVA-pseudotyped rabies virus was collected, filtered and concentrated using an ultracentrifuge. The virus titer was determined by infection of HEK293T-TVA cells with serially diluted viruses. RabV CVS-N2c$^{\Delta G}$ -EGFP was a gift from Thomas Jessell (Addgene plasmid #73461; http://n2t.net/addgene:73461; RRID: Addgene_73461). pSAD$^{\Delta G}$-F3 was a gift from Edward Callaway (Addgene plasmid #32634; http://n2t.net/addgene:32634; RRID: Addgene_32634).

Patient-derived glioblastoma cultures

Patient-derived glioblastoma spheroid models from resected tumor material were cultivated as previously described[8,9,103] in DMEM/F-12 under serum-free, non-adherent conditions, which includes B27 supplement without Vitamin A, insulin, heparin, epidermal growth factor, and fibroblast growth factor as described before.[104] Glioblastoma models U3085MG, U3048MG, U3047MG, U3017MG were obtained from the Human Glioma Cell Culture (HGCC, www.hgcc.se) biobank resource at Uppsala University, Uppsala, Sweden.[51]

To express the TVA receptor in patient-derived glioblastoma spheroid models, the cells were transduced with lentiviral vectors with a modified TVA-P2A-mCherry-2A-oG construct based on the Addgene plasmid #85225. Membrane-bound GFP expression was achieved with the pLego-T2-mGFP construct,[105] and for calcium imaging the cells were transduced with the pLego-T2-GCaMP7b-tdTomato construct.[93] For direct labeling, TVA-oG-mCherry expressing glioblastoma spheroids were transduced with rabies virus constructs SAD-B19$^{\Delta G}$-eGFP(EnVA) or CVS-N2c$^{\Delta G}$-eGFP(EnVA) prior to further experiments.[33] Transduced cells were sorted regularly by FACS with either FACSAria Fusion 2 Bernhard Shoor or FACSAria Fusion 1 Richard Sweet (BD Biosciences). The following filters were used for the respective fluorophores: 610/20 for mCherry, 530/30 for GFP, 586/15 for tdTomato.

850k methylation array analysis

The Illumina Infinium Methylation EPIC kit was used to obtain the DNA methylation status at >850,000 CpG sites in patient-derived glioblastoma spheroid models, according to the manufacturer's instructions at the Genomics and Proteomics Core Facility of the German Cancer Research Center in Heidelberg, Germany, as described previously.[106] The molecular classification of patient-derived glioblastoma models used in this study can be found in Table S1.

Harvesting cortical tissue from human patients

During surgical interventions, cortical tissue proximal to deeper pathologies was precisely and safely extracted, guided by neuronavigation techniques. To ensure the removal of non-damaged tissue, we applied a refined method recently detailed by Straehle et al.[107] This technique enhances the accurate identification and collection of cortical tissues, aiming to minimize harm. The criteria for selecting human slice cultures are rigorously defined to maintain the material's study relevance and integrity. Specifically, tissue designated for slice culture is required to be more than 10 millimeters away from identified pathologies, like metastases or vascular issues, establishing a safety margin to exclude potentially compromised tissue not evident visually. For glioma tumors, the criteria are stricter, demanding over 20 millimeters of separation from the tumor, acknowledging gliomas' diffuse infiltration potential. While ensuring pathology-free tissue is challenging, we leveraged Scattered Raman Histology and AI-based detection to mitigate the impact of any significant tumors or pathologies on the harvested cortex in selected patients.[108]

Human organotypic slice cultures

Human neocortical slices were prepared following a recently described procedure.[109–112] Immediately after resection, cortical tissue was transported to the laboratory in a carbogen-saturated "Preparation medium" (Gibco Hibernate™ media with 0.5 mM Gibco GlutaMax™, 13 mM Glucose, 30 mM NMDG, 1% Antibiotic-Antimycotic, 1 mM ASC Acid, and HI Horse Serum) on ice. Under a 10x microscope, capillaries and damaged tissue were microdissected, and the arachnoid was microsurgically removed. The collection medium, enriched with GlutaMax and NMDG, ensured optimal tissue recovery. Cortical slices, 300 μm thick, were created using a vibratome (VT1200, Leica Germany) and incubated in the preparation medium for 10 minutes pre-plating to minimize variability from tissue trauma. Typically, tissue blocks (1 cm × 2 cm) allowed for 15 sections, with 1-3 sections per insert being carefully spaced. A polished wide-mouth glass pipette facilitated slice transfer. The slices were then maintained in a growth medium composed of Neurobasal L-Glutamine (Gibco) supplemented with 2% serum-free B-27 (Gibco), 2% Anti-Anti (Gibco), 13 mM d-glucose (Sigma-Aldrich), 1 mM MgSO4 (Sigma-Aldrich), 15 mM HEPES (Sigma-Aldrich), and 2 mM GlutaMAX (Gibco). The medium was refreshed 24 hours after plating and then every 48 hours. For inoculation, target cells were prepared as previously mentioned, undergoing post-trypsinization centrifugation, harvesting, and resuspension in PBS at 10.000-20.000 cells/μl. Cells were inoculated into tissue sections using a 10 μL Hamilton syringe to deliver 1 μL, then incubated at 37°C for four to fourteen days with medium changes every 48-72 hours. Tumor proliferation was assessed using fluorescence imaging with an inverted microscope (Observer D.1; Zeiss). After the designated culture period, sections were fixed for immunostaining.

Spatial Transcriptomics

Tissue processing for FFPE human organotypic slice culture

7 days following the injection of $GB^{Starter}$ cells, human organotypic slice cultures were fixed in 4% PFA for one hour, washed in 1X PBS, and paraffin-embedded. For spatial transcriptomics, the tissue blocks were rehydrated in ice water for 10 minutes, sectioned at 5 μm thickness, and mounted on Poly-Prep slides. The slides were baked at 42°C for 3 hours and stored in a desiccator until further use. Before HE staining, the slides were heated at 60°C for 2 hours, followed by deparaffinization and dehydration through a series of xylene and ethanol washes. Hematoxylin staining was performed for 3 minutes, followed by thorough rinsing and 1-minute incubation with Bluing Buffer treatment. Alcoholic eosin was applied for 2 minutes, with multiple washes to ensure uniform staining. Finally, 85% glycerol was applied, and the slides were coverslipped. Imaging was conducted with settings identical to those used for fresh frozen spatial transcriptomic samples. The most spatially relevant section from each sample, as determined by imaging, was selected for further processing to ensure optimal downstream analysis.

Library Construction

The coverslips were removed by soaking the slides in Milli-Q water until the coverslips detached, followed by washes to eliminate any remaining glycerol. The slides were then dried at 37°C for 3 minutes and placed in a tissue slide cassette. Destaining was performed by adding 0.1N HCl, and incubation on a thermal cycler with slide adapter at 42°C for 15 minutes. For FFPE tissue, this was followed by decrosslinking with diluted decrosslinking buffer at 95°C for 60 minutes and 22°C for 10 minutes. Library construction was performed according to Protocol CG000495 from 10X Genomics. Human WT Probes v2 (PN:2000657, 2000658) for the spatial transcriptomics of human organotypic slice cultures were diluted in hybridization buffer and incubated at 50°C for 18 hours. After hybridization, the sections were washed with prewarmed Post Hybridization Buffer 3 times at 50°C and ligated at 37°C for 1 hour. Following 2 post-ligation washes at 57°C, the slides were removed from the cassettes and stained with 10% eosin for 1 minute. They were then rinsed with 1X PBS, carefully aligned in the Visium CytAssist, and the Probe Release Mix, prepared with Tissue Removal Enzyme, was added to the wells of the Spatial Transcriptomics slide. The slides were incubated at 37°C for 30 minutes in the Visium CytAssist instrument, then washed with 2X SSC and transferred into a new cassette for the subsequent steps. Probe Extension Mix was added to wells A1 and D1 of the Visium Cassette, which was then placed on a thermal cycler at 45°C for 15 minutes. After incubation, the Probe Extension Mix was removed, and 0.08 M KOH was added for 10 minutes to elute the probes. The eluted probes were collected and neutralized with Tris-HCl pH 7.0 before being amplified with Pre-Amplification Mix and cleaned up using SPRIselect magnetic beads. The probes were diluted 1:5 and loaded onto a qPCR cycler to determine the optimal amplification cycle number. Using the determined cycle number, the probes were then amplified and indexed using two distinct wells of the Index Plate TS Set A. After a final SPRIselect cleanup, a TapeStation was used to confirm successful library construction and to calculate the average base pair length. All probes were pooled and normalized to 1.2 nM using the dsDNA HS Assay and a Qubit instrument. Finally, 20 μl of the pooled normalized library was loaded onto an Illumina NextSeq1000/2000 sequencer, and the resulting fastq files were preprocessed using the Spaceranger v2.1 pipeline.

Immunofluorescence staining FFPE sections

Slides were placed on a thermal plate at 60°C for 5 minutes, then sequentially incubated in xylene (10 minutes and 5 minutes) and a graded ethanol series (100%, 95%, 80%, and 70%). Rehydration was performed in 1X PBS. Slides were decrosslinked in 10 mM sodium citrate buffer (pH 6.0) by cooking for 15 minutes, followed by incubation in 1X PBS. Blocking was done with 5% normal goat serum (NGS) in 0.1% PBS-T (PBS with 0.1% Triton) for 1 hour, followed by overnight incubation with the primary antibodies at 4°C in the dark. The next day, slides were washed three times for 15 minutes in 0.1% PBS-T and incubated with secondary antibody solution in 0.1% PBS-T for 1 hour at 4°C in the dark. After washing three times for 15 minutes in 0.1% PBS-T, DAPI (1:1000 v/v in 1x PBS) was applied for 5 minutes, followed by three washes in PBS and coverslipping with FluoroMount. Imaging was performed using a Zeiss Axioscope5 fluorescence microscope.

Segmentation

We processed the images containing GFP and NeuN signals in CellProfiler[113] to identify neurons (NeuN+) as primary objects. To optimize object identification, the following parameters were selected: (1) Object diameter: minimum ~3 μm and maximum ~15 μm (adjusted according to image resolution); (2) Thresholding method: Two-class Otsu with a smoothing scale of 1.33, and threshold bounds set to 0.3 (lower) and 1.0 (upper); and (3) Threshold strategy: "Adaptive" with a window size of 50. After segmenting the primary objects, we quantified the GFP signal by extending the primary objects by 10 pixels. The identified objects and corresponding GFP signals were exported as csv files. Using R,[96] we extracted the x and y coordinates of the segmented neurons and rescaled them to align with the coordinates of the SPATA[100] object. The density distribution of the eGFP signal (mean eGFP) across segmented primary objects was then analyzed to establish a cutoff, distinguishing between connected and non-connected neurons.

Spatial Transcriptomic Analysis

Spatial transcriptomic preprocessing was performed using the SPATA2 (v2.04) package which was described in detail most recently.[100] We used the SPATA2::initiateSpataObject_10X followed by gene expression $\log_{10}$ normalization, quality check and quantification of pixel to metric distance ratios. Shifts between images was performed by the exchangeImage function of SPATA.

Cell Deconvolution

For cell type decomposition, we utilized the extended GBMap atlas, which includes a comprehensive dataset of over one million cells.[61] We developed a pipeline for single-cell deconvolution using Cytospace in conjunction with SPATA objects. The complete details of this workflow are available on GitHub (github.com/heilandd). The R script, "CytoSpace_from_SPATA.R," provides a

step-by-step guide for preparing files compatible with the Cytospace suite, along with a bash script to facilitate the batch processing of SPATA2 objects. The Cytospace analysis is executed in a bash environment, and upon completion, the results can be re-imported into the SPATA2 framework using the CytoSpace2SPATA function. In addition, we incorporated the cell2location model[114] into our analysis to integrate Visium spatial transcriptomics data with the GBMap single-cell glioblastoma dataset. To meet computational requirements, the single-cell dataset was downsampled to 100.000 cells. Signature estimation was performed using the cell2location Negative Binomial regression model, generating the inf_aver_sc.csv file, which served as the basis for the spatial deconvolution process. We identified shared genes between the signature genes and the spatial dataset, which were then used to initiate the cell2location model. The model was trained using recommended hyperparameters and early stopping criteria based on ELBO loss. Upon completion of training, the posterior distribution of cell abundance was quantified and extracted for further analysis. The expected expression for each cell type was calculated, and cell-specific expressions were documented for subsequent analyses.

Spatial Autocorrelation Moran's I

Spatial autocorrelation, assessed using Moran's I statistic, evaluates the degree of spatial dependency among segmented neurons based on their attribute to connected^{TUM} or unconnected^{TUM} neurons. This analysis helps determine whether a particular feature is spatially clustered, evenly distributed, or randomly scattered. A statistically significant Z-score or p-value indicates the presence of spatial autocorrelation. Specifically, a positive Moran's I value suggests a tendency for clustering, while a negative value suggests dispersion. We quantified Moran's I as described before.[109]

Surgical procedures

Prior to *in vivo* two-photon imaging, surgical procedures were performed as described previously.[8,9,16] Cranial window implantation in mice was done in a modification of what we had previously described, including a custom-made teflon ring for painless head fixation during imaging. 1 to 3 weeks after cranial window implantation, 50.000-100.000 glioblastoma cells were stereotactically injected into the mouse cortex at an approximate depth of 500 μm. Alternatively, the stereotactic tumor injection was performed without prior cranial window implantation into the mouse cortex as described above or into the striatum (1 mm A/P and 2 mm M/L to bregma, 2 mm D/V to cranial surface).

For *in vivo* retrograde tracing of the neuronal connectome, tumor injections were done following the direct labeling protocol as described above. Tumor cells were injected either into the cortex or the striatum. For *ex vivo* analyses of tissue, mice were sacrificed via perfusion, time point depending on experimental paradigm.

Intravital microscopy

The tumors were observed from 1 week after tumor implantation in cranial window bearing mice with a Zeiss 7MP or Zeiss LSM980 NLO setup equipped with bandpass filter sets of 500 - 550 nm and 575 - 610 nm, using a 20x (1.0 NA) apochromatic, 1.7 mm working distance, water immersion objective (Zeiss). A pulsed Ti:Sapphire laser (Chameleon Discovery NX; Coherent) was used at 960 nm wavelength.

Isoflurane gas was diluted in 100% O2 for *in vivo* imaging. For the induction of anesthesia, the mice were exposed to 4% isoflurane, which was lowered to 0.5-2% for the rest of the experiment and was monitored throughout the experiment. Eye cream was applied after anesthesia induction. During imaging, the body temperature was monitored and kept at 37°C using a temperature sensor and a heating plate. Anesthesia was regularly evaluated during image acquisition by checking the breathing rate.

Intravital microscopy analysis of dendritic plasticity

Time-lapse imaging of dendritic stretches of connected^{TUM} neurons was performed every two days for six days total with a lateral resolution of 0.10 μm/pixel and an axial resolution of 0.32 μm/pixel. Analysis of time-lapse imaging of dendritic plasticity in connected^{TUM} neurons was performed manually in Fiji.[95] After registration of each stack to minimize drift between acquisition time-points using a custom script, regions of interest of dendritic stretches were cropped for further analysis. For each time-point, the number of dendritic spines from 50 total dendritic stretches was determined.

Airyscan microscopy and analysis of dendrites in *ex vivo* brain slices

Airyscan microscopy[115,116] of dendritic stretches of connected^{TUM} and unconnected^{TUM} neurons was performed using LSM980 Airyscan NIR (Zeiss) or LSM900 Airyscan (Zeiss) with a 63x oil immersion objective (NA 1.4). Images were acquired using calibrated Airyscan detectors with a lateral resolution of 0.043 μm/pixel and an axial resolution of 0.15 μm/pixel. Airyscan processing was performed in the Zen Blue software.

For the analysis of dendritic spine morphologies and density in connected^{TUM} and unconnected^{TUM} neurons, fixed acute brain slices were used (see STAR Methods section "acute brain slice preparation"). To re-identify patched neurons, slices were stained against Neurobiotin with Streptavidin-coupled Alexa 647 at a dilution of 1:1000 as described above. Dendritic spines of basal dendrites were classified into filopodia, thin, stubby, mushroom or branched types as previously described.[117] To quantify the dendritic spine densities of connected^{TUM} and unconnected^{TUM} neurons, crops of approximately 10 μm x 10 μm in the full z-range of the dendritic stretch of interest were generated. The manually counted number of dendritic spines was normalized to the length of the dendritic stretch.

Assessment of mouse behavior

Male nude NMRI mice were maintained at the Interdisciplinary Neurobehavioral Core at Heidelberg University in groups of four per cage, consisting of two control and two tumor-bearing mice. A baseline measurement of the tests was performed prior to tumor implantation. Tumor was striatally implanted as described above, control mice were injected with PBS. The behavioral test battery was performed twice in a time frame of 14 days following tumor implantation during the same time of day as baseline measurements. At 14 days post injection, mice were transcardially perfused and the tissue was used for *ex vivo* analysis. Following tests were performed in the behavioral test battery:

Cat Walk Test

Test was performed using CatWalk XT version 10.6 gait analysis system (Noldus Information Technology, Wageningen, Netherlands).[118] Mice were placed on 1.3 m black corridor walkway on a glass plate and observed a minimum of 4 walks per session. After each trial the walkway was cleaned with 75% ethanol solution wetted tissue paper.

Voluntary Wheel Running Test

Mice were placed in cages containing a running wheel and free access to food and water individually. They were observed for a period of 24 hours each, using the AMW counter (Lafayette Instrument, Louisiana, USA) and an optical sensor to detect revolutions of the wheel.[119]

Cold Plate Test

For the assessment of analgesic response mice were placed on a Hot/Cold Plate (Bioseb, Vitrolles) at 2° C and the latency until the first withdrawal response of the hind paw was recorded. Following response, the mouse was removed immediately and cut-off latencies were set at 30 seconds. The test was repeated three times per mouse per trial and the average was calculated. The plate was wiped with 75% ethanol solution wetted tissue paper between mice exchange.[119]

Von Frey Test

To determine mechanical sensitivity, graded Von Frey filaments were used with bending forces of 0.07, 0.16, 0.4, 0.6, 1 and 1.4 g with increasing forces on the plantar surface of each hind paw. Each filament was tested 5 times while recording the number of withdrawals.[119]

LABORAS Observation

To assess the innate behavior of mice in a home-cage-like environment, mice were weighed before each trial and individually placed in cages on top of a carbon fiber platform used for the LABORAS (Laboratory Animal Behavior Observation Registration and Analysis System, Metris B.V.) system, which is based on behavior-specific vibration patterns. Mice were observed for a period of 24 hours each.[120]

Stereotactic AAV- injection

The surgical procedure was performed as previously described for chronic cranial window implantation.[9,16] After removal of the piece of skull and the underlying dura mater, 1 μl of AAV (AAV2-CaMKIIahChR2(H134R)-mCherry for neuronal channelrhodopsin stimulation and pAAV- CaMKIIa- mCherry or AAV9-CamKIIa-ChrimsonR-mScarlet-KV2.1 for the control) was stereotactically injected into the mouse cortex at a depth of 450 μm using a glass micropipette (Blaubrand IntraMARK 5 μl, #708707, Wertheim) that was pulled before (Sutter Instruments, Novato CA, USA). Next, approximately 100.000 tumor cells were injected into the mouse cortex at a depth of 500 μm in proximity to the viral injection site. The surgical procedure was then finished as previously described for chronic cranial window surgery.

Optogenetic stimulation and consecutive time-lapse imaging

ChR-mCherry-expressing neurons or solely mCherry-expressing neurons as control were exposed to blue laser light (473 nm, Shanghai Laser & Optics Century Co. Ltd, China) through an optical fiber (Laser Components, Item 3016347). 15 stimulations at 20 Hz for 30 seconds with a 90 second pause in between were performed according to previously published protocols.[8,17,81] A custom written MATLAB script[16] and a PulsePal device enabled control of the stimulation and the shutters of the microscope. Directly after the stimulation, *in vivo* two-photon time-lapse imaging was performed, where a stack of 447 μm x 447 μm x 100 μm was repetitively acquired every 4 or 5 minutes over 4 hours.

Analysis of tumor area and density of CHRM3 knockdown mice

Mice were injected with patient-derived glioblastoma cells lentivirally transduced with a mGFP-fluorescent CHRM3 knockdown variant (shCHRM3-mGFP) or a scrambled control variant (scrambled-shCHRM3-mGFP) as described before.[94] Cells were injected into the retrosplenial cortex (-3 mm A/P and 0.5 mm M/L to bregma, 1.5 mm D/V at a 45° angle to the cranial surface). Mice were transcardially perfused 60 days following tumor implantation and brains were post-fixed overnight in 4% (w/v) PFA. 80 μm serial sections were cut using a semiautomatic vibratome (Leica VT1000s). Whole slices containing the largest tumor area per mouse were imaged using a Leica Mica microscope with a 20x (NA 0.75) air objective. Tumor area in the cortex was measured using a machine learning based segmentation of the mGFP signal using ilastik.[97] For tumor cell density, slices were stained for DAPI (1:10000 v/v in 1x PBS) and nestin (see STAR Methods section "sample preparation, immunohistochemistry, and confocal microscopy") and imaged at a Leica LSM710 confocal microscope using a 20x (NA 0.8) air objective. A 1190 μm x 1190 μm x 55 μm tile scan of the injected cortical region was imaged and the cell density was manually determined in 3D using Fiji.[95]

Combined irradiation and perampanel therapy *in vivo*

Mice were injected with S24 mGFP[8] cells after cranial window surgery and the tumor establishment was determined through weekly observation using two-photon microscopy as described above. Mice were categorized into two treatment groups with similar tumor size: only irradiation and combined perampanel and irradiation. Food pellets of mice in the combined therapy group were exchanged by pellets containing 320 mg/kg perampanel and offered *ad libitum* until the end of the experiment. The dose was escalated to 640 mg/kg if mice tolerated the initial dose. Mice in the only irradiation group were offered their normal food *ad libitum*. Two weeks after the start of the perampanel treatment of mice from the combined therapy group, all mice were irradiated on three consecutive days with 7 Gray each. Tile scan images of tumor were acquired on the first day of irradiation and seven days after the first day of irradiation. The two time points were registered using a custom script and a common volume of 600 μm x 600 μm x 102 μm was cropped. The cell density was manually determined in 3D using Fiji[95] for both time points.

For *in vivo* MRI studies, mice were injected with S24 mGFP cells without prior window implantation. Prior to MR imaging, mice were anesthetized with 1,5-2% isoflurane and monitored during imaging using a custom monitoring system (LabVIEW, National Instruments). The body temperature of the mice was kept stable during imaging using a heating pad. Images were acquired on a 9.4T small animal MR scanner (BioSpec 94/20 USR, Bruker BioSpin) with a four-channel phased-array surface coil. Mice were stratified into two treatment groups with similar tumor size based on MRI measurements 70 days after tumor injection: only irradiation and combined perampanel and irradiation. The groups were treated equivalent to the mice used for the two-photon microscopy study as described above.

For analysis, MRI measurements were performed on day 10 after the first day of irradiation of all animals. A 3D T2-weighted rapid acquisition with relaxation enhancement (RARE) sequence was chosen for tumor volume assessment. Sequence parameters were: TE = 72.56 ms, TR = 1800 ms, rare factor = 32, flip angle = 90°, image size: 20 mm × 10 mm x 12 mm, slice thickness = 100 μm, resolution: 100 μm isotropic, number of averages = 1, duration of acquisition: 10 minutes and 48 seconds. Exported DICOM files were visualized and analyzed in Fiji.[95] Analysis was performed by four investigators with a consensus reading of the data who were blinded to the treatment group (E.R., F.T.K., M.O.B. and V.V.; F.T.K. and M.O.B are board-certified neuroradiologists with 11 years and 10 years of experience, respectively). The MRI slice with the largest visible tumor area was chosen for each animal and the whole brain area and tumor area were manually segmented. Tumor area fraction was calculated as tumor area ratio to whole brain slice area.

Radiotherapy of non-tumor-bearing mice prior to tumor implantation

Non-tumor-bearing mice were divided into two groups prior to intervention: control and radiotherapy. Mice in the radiotherapy group were irradiated with 7 Gray on three consecutive days as described above. The control group was anesthetized with the same amount of ketamine/xylazine as the radiotherapy group to discard possible anesthesia-induced effects. 3-7 days after the last day of irradiation, both groups were injected cortically with S24 TVA-oG-mCherry-expressing and CVS-N2c$^{\Delta G}$-eGFP(EnVA) infected GB^{Starter} cells. Mice were perfused 7 days after tumor implantation.

Brain sections with the largest tumor area were imaged with a Leica Mica microscope with a 20x (NA 0.75) air objective and were analyzed for the amount of connected^{TUM} neurons using a machine learning based segmentation of the eGFP signal using ilastik.[97] Further quantification was done as described in the STAR Methods section "determination of input-to-starter ratios".

Sample preparation, immunohistochemistry, and confocal microscopy

For *ex vivo* analyses of PDX models, the mice were anesthetized with either ketamine/xylazine (150mg/kg body weight (BW) and 20mg/kg BW respectively) or pentobarbital (500 mg/kg BW) with an intraperitoneal injection. Mice were perfused transcardially with PBS followed by 4% PFA (w/v) in 1x PBS. After removal of the brain, it was post-fixed in 4% PFA overnight and kept in PBS at 4°C. Serial sections of 80-100 μm were cut with a semiautomatic vibratome (Leica VT1000s). For *in vitro* analyses, coverslips were washed once with 1x PBS and subsequently fixed with 4% PFA (w/v) in 1x PBS for 5-10 minutes. Afterwards, they were washed once with 1x PBS and stored in PBS at 4°C.

Ex vivo mouse brain slices and organotypic slices were first permeabilized with 1% (v/v) Triton X-100 and 5% (v/v) FBS in 1x PBS for 2 hours. In the following, the primary antibodies were solved in in 1% (v/v) FBS and 0.2% (v/v) Triton X-100 in 1x PBS, generally in the recommended dilution of the manufacturer, with the exception of mouse anti-nestin and rabbit anti-iba1 with a dilution of 1:300 and chicken anti-GFP with a dilution of 1:300-1:1000. Afterwards, the slices were washed 3x with 2% (v/v) FBS in 1x PBS for 15 minutes each. The secondary antibodies were solved in the same buffer as the primary antibodies with a general dilution of 1:500. The primary and the secondary antibodies were both incubated for 20-24 hours each. After the incubation time of the secondary antibody, the slices were washed 3x with 1% (v/v) FBS in PBS for 10 minutes each, followed by 3x washing steps with 1x PBS for 10 minutes each. All incubation steps were performed at room temperature on a shaker. Sample mounting was performed with SlowFade Gold solution.

For *in vitro* stainings, the coverslips were permeabilized for 10 minutes with 0.2% (v/v) Triton X-100 in 1x PBS. Afterwards, blocking was performed by incubating the samples in 10% FBS (v/v) in 1x PBS for 10 minutes. In general, the primary antibodies were solved in blocking buffer with a dilution according to the manufacturer, with the exceptions of anti-nestin mouse with a dilution of 1:300-1:2000 and anti-GFP chicken with a dilution of 1:200-1:1000. Subsequently, after 1h of incubation, the coverslips were washed 2x with 1x PBS for 5 minutes each before the respective secondary antibody was applied with a general dilution of 1:500 in the blocking buffer.

After another hour of incubation, the coverslips were washed again 2x with 1x PBS for 5 minutes each. All incubation steps were performed at room temperature, shaking. Finally, the coverslips were mounted with SlowFade Gold solution and DAPI diluted 1:10000 (v/v) in 1x PBS.

Images were acquired using either a 20x air (NA 0.8) or 63x oil immersion objective (NA 1.4) at a confocal laser-scanning microscope (LSM710 ConfoCor3 or LSM980 Airyscan NIR, Zeiss).

Immunohistochemistry of FFPE human sections

First, slides were subjected to a series of solvent incubations under a fume hood to achieve format conversion. The slides were placed in a glass cuvette and sequentially incubated twice with 100% xylene, twice with 99% ethanol, followed by once with 95% ethanol, once with 70% ethanol, once with 50% ethanol, and finally with MilliQ water for 3 minutes each. Subsequent to this, antigen retrieval was conducted by placing the samples in a 20mM sodium citrate buffer (pH 8.0, dissolved in MilliQ water) within the glass cuvette. The samples were then subjected to three to four cycles of heating in a microwave at 360W, allowing the buffer to cool slightly between each cycle. The samples were then incubated in an oven at 60°C for 30 minutes. For blocking, a 5% FBS (v/v) solution in 1x PBS was applied for 30 minutes. A hydrophobic pen was used to delineate the area on the slide for the blocking and subsequent antibody incubations. Primary and secondary antibodies were incubated at 4°C for 20-24 hours. Immunohistochemistry was carried out as described before. A custom 3D-printed slide holder, designed using the UltiMaker Cura 5.6.0 software and fabricated on an UltiMaker 2 printer, was employed to minimize reagent volume and ensure effective washing by removing unbound antibodies. Finally, the samples were mounted using SlowFade Gold solution combined with DAPI (1:10000 v/v in 1x PBS).

Airyscan microscopy of putative cholinergic synapses in *ex vivo* PDX brain slices and FFPE human sections

Putative cholinergic neuron-glioma synapses (NGS) were studied using Airyscan microscopy.[115] *Ex vivo* PDX brain slices and FFPE human tissue sections were stained against VAChT (vesicular acetylcholine transporter, pre-synaptic marker), CHRM3 (post-synaptic marker) and Nestin (tumor cell marker) as described above. Imaging was conducted using a Zeiss LSM900 Airyscan NIR microscope equipped with a 63x oil immersion objective (NA 1.4) and a 40x water immersion objective (NA 1.2). Images were acquired using calibrated Airyscan detectors, achieving a lateral resolution of 0.049 μm/pixel with the 40x objective and 0.042 μm/pixel with the 63x objective. The axial resolution was 0.19 μm/pixel with the 40x objective and 0.15 μm/pixel with the 63x objective. Airyscan processing was performed in the Zen Blue software. Quantification of putative NGS was performed on regions of interest using a custom pipeline with Arivis Vision4D x64. Probability maps for tumor cell, pre- and postsynaptic signals were created using ilastik.[97] To account for the bias that larger cells may have more NGS, we normalized the number of detected NGS by the tumor cell's surface volume, resulting in a quotient expressed as [NGS count/μm^2 GB surface].

Mouse and rat cortical, hippocampal and basal forebrain cultures

Preparation of rat cortical cultures was done as described previously.[16] Briefly, cells from E19 embryos were seeded on 12 mm coverslips in 24-well plates coated with poly-L-lysine at a density of 90,000 cells/cm^2. They were cultured in a medium of Neurobasal (Invitrogen), supplemented with B27 (50x, 2%v/v) and L-glutamine (0.5 mM). The same protocol was used for rat hippocampal cultures, with the exception of 2.5% Trypsin (10x) instead of 0.05% Trypsin-EDTA (1x), as used for cortical cultures.

Mouse cortical cultures were prepared similarly to rat cortical cultures using cells from P1 and P2 mouse pups.

Primary basal forebrain cultures were prepared as previously described from the dissected septum of E19 rat embryos and plated at a density of 100,000 - 200,000 cells per well on 12 mm coverslips in 24-well plates coated with poly-L-lysine.[121] They were cultured in neurobasal medium supplemented with B27 supplement (50x, 2% v/v), L-glutamine (0.5 mM) and neuronal growth factor (50 ng/ml). Culture medium was changed twice a week.

Quantification of VAChT signal in basal forebrain cultures using Airyscan microscopy

Cortical and basal forebrain cultures were stained for VAChT (1:200 dilution) as described above. Samples were imaged at the Zeiss LSM900 Airyscan NIR microscope with a 40x (NA 1.2) water immersion objective with a resolution of 0.057 μm x 0.057 μm x 0.22 μm. Airyscan processing was performed in the Zen Blue software. Maximum intensity projections were trained using the ilastik[97] pixel classification pipeline and probability maps were exported. All further processing steps were performed in Fiji.[95] For quantification of the VAChT density, probability maps were auto-thresholded using the "Threshold" function and the number of punctae were determined using the "Analyze Particles" function with a cut-off by a minimum of 0.015 μm^2 area.

Human iPSC- and ESC-derived neurons

Human embryonic stem cells (hESC) of line WA01/H1 were obtained from WiCell whereas iPSCs were locally derived from a healthy donor (HD6, Heidelberg University, Heidelberg, Germany). Pluripotent cells were feeder-free cultured on Matrigel-coated (Corning #15505739) dishes, using mTeSR Plus medium (StemCell Technologies #100-0276). mTeSR was changed every other day and cells were passaged every 3–5 days using ReLeaSR (StemCell Technologies #05872). All cell cultures were maintained in a humidified incubator with 5% CO_2 at 37°C. All procedures were approved by the Robert Koch Institute.

Induced glutamatergic neurons were differentiated from iPSCs or hESC according to previously described methods.[54] Briefly, for each differentiation 250,000 hESCs were detached with Accutase (Gibco), plated on matrigel-coated wells in mTeSR Plus containing

Rho kinase inhibitor (Y27632, Axon Medchem #1683, or Thiazovivin) and simultaneously transduced with lentiviruses FU-M2rtTA and Tet-O-Ngn2-puromycin. One day later (defined as div0), the media was replaced with N2 media [DMEM/F12 (Gibco #11330032), 1% N2 supplement (Gibco 17502048) 1% non-essential amino acids (Gibco #11140050), laminin (200 ng/ml, Thermo Fisher #23017015), BDNF (10 ng/ml, Peprotech #450-02) and NT-3 (10 ng/ml, Peprotech #450-03) supplemented with Doxycycline (2 μg/ml, Alfa Aesar) to induce expression of NGN2 and the puromycin resistance cassette. On div1, puromycin (1 mg/ml) was added to the medium and after 48h of selection, cells were detached with Accutase (Gibco #A1110501) and re-plated on Matrigel-coated coverslips along with mouse glia (see below, typically at a density of 150,000 iGluts/24-well) in B27 media [Neurobasal-A (Gibco #12349015 supplemented with B27 (Gibco #17504044), GlutaMAX (Gibco #35050061) laminin, BDNF and NT-3]. Near 50% of the medium was replaced every second day for eight days, with cytosine arabinoside (ara-C; Sigma #C6645) added to a working concentration of 2 μM to prevent glia overgrowth. From div10 onward, neuronal growth media [Neurobasal-A supplemented with B27, GlutaMAX and 5% fetal bovine serum (FBS) (Hyclone #SH30071.03HI)] was washed in and used for partial media replacements every 3-4 days until analysis, typically after 4-6 weeks in culture.

Mouse glia cells used for co-cultures with induced glutamatergic neurons, were isolated as described before.[122] Briefly, P3 mouse cortices from wildtype C57BL6 mice were dissected and triturated with fire polished Pasteur pipettes, and passed through a cell strainer. Typically, lysates from two cortices were plated onto a T75 flask pre-coated with poly-L-lysine (5 mg/ml, Sigma #P1274) in DMEM supplemented with 10% FBS (Sigma). Once primary mouse glial cells reached confluence, they were dissociated by trypsinization and re-seeded twice and then used for co-culture with induced glutamatergic neurons.

Cell viability assays

The cell viability assay was used to assess toxicity of rabies virus strains in patient-derived glioblastoma spheroids as well as to compare the growth behavior of S24 with and without M3 receptor knockdown in monoculture. Cells were seeded on to an opaque 96 well plates in either neurobasal medium supplemented with B27 (50x, 2% v/v) and L-glutamine (0.5 mM) or in DMEM/F12, at a density of 5000 cells/well. Per patient-derived glioblastoma model, we seeded wells with glioblastoma cells transduced only with the TVA-oG-mCherry construct, directly labeled TVA-oG-mCherry expressing and CVS-N2c$^{\Delta G}$-eGFP(EnVA) infected glioblastoma cells, and directly labeled TVA-oG-mCherry expressing and SAD-B19$^{\Delta G}$-eGFP(EnVA) infected glioblastoma cells to assess toxicity of rabies virus. To investigate the growth behavior with and without M3 knockdown, we seeded wells with GB model S24 transduced with either the shCHRM3-mGFP or the scrambled-shCHRM3-mGFP construct. The assay was performed according to the manufacturers protocol (Promega, Madison, WI) on 3 consecutive days. Luminescence was measured 10 minutes after incubation at room temperature for signal stabilization. Values were normalized to the respective first measurement.

Evaluation of rabies-induced toxicity

Co-cultures of TVA-oG-mCherry expressing glioblastoma cells and rat cortical neurons were infected with either CVS-N2c$^{\Delta G}$-eGFP(EnVA) or SAD-B19$^{\Delta G}$-eGFP(EnVA) as described above or kept without. Coverslips were fixed eight days post seeding and infection. Coverslips were stained for nestin, GFP and cleaved caspase 3 as previously described. The cleaved caspase 3 signal was trained using ilastik[97] and quantified as described in STAR Methods section "determination of input-to-starter ratios".

Single-cell apoptosis-related genes expression analysis

Using the AddModuleScore function from Seurat, a score was calculated using a subset of genes associated with the positive regulation of the execution phase of apoptosis downloaded from https://amigo.geneontology.org/amigo/.[64,65] Genes included can be found in Table S1.

Direct and sequential labeling of glioblastoma cells for retrograde tracing

Experiments were performed following either the direct or the sequential labeling approach. For the direct approach, patient-derived glioblastoma spheroids were transduced with both the TVA-oG-mCherry construct and either SAD-B19$^{\Delta G}$-eGFP(EnVA) ($5x10^4$ vg/ml) or CVS-N2C$^{\Delta G}$-eGFP(EnVA) (10^6 vg/ml) used in this study before conducting further experiments. They were cultured as described above under spheroid primary culture conditions. For the sequential approach, TVA-oG-mCherry expressing glioblastoma cells were seeded, followed by a sequential rabies infection on the co-cultures at a titer as described in the respective methods sections.

Sparse and dense sequential retrograde labeling

For tracing of the neuronal connectome of singular tumor cells, SAD-B19$^{\Delta G}$-eGFP(EnVA) or CVS-N2C$^{\Delta G}$-eGFP(EnVA) were added to co-cultures of TVA-oG-mCherry expressing tumor cells and div07 rat cortical neurons at a titer of $10\text{-}10^2$ vg/ml depending on patient-derived model used, 2 hours after seeding. A circular area of 400 μm diameter was analyzed to determine the local connectome of singular tumor cells. For dense labeling of glioblastoma cells, SAD-B19$^{\Delta G}$-eGFP(EnVA) or CVS-N2C$^{\Delta G}$-eGFP(EnVA) were applied at a titer of 10^5 vg/ml.

In vitro live-cell time-lapse imaging of retrograde labeling

For rabies virus based retrograde live-cell imaging, TVA-oG-mCherry expressing patient-derived glioblastoma spheroids were seeded onto div7 rat cortical cultures at a density of 1000 cells per well in 24 well plates. SAD-B19$^{\Delta G}$-eGFP(EnVA) or

CVS-N2C$^{\Delta G}$-eGFP(EnVA) (both 10^3 vg/ml) virus was added 1 hour after seeding. For experiments at later infection time points, rabies viruses were added 5 or 11 days after seeding glioblastoma cells.

Imaging was performed 2 hours after seeding of glioblastoma cells for a time period of 3-5 days at 37 degrees Celsius with 5% CO_2. Images were acquired using a Zeiss LSM780, a Zeiss LSM710, a Zeiss Celldiscoverer7 confocal or a Nikon Ti-HCS widefield microscope with a 10x (NA 0.3)/20x (NA 0.95) objective and a pixel size of 770 nm – 1.38 μm. Coverslips were imaged every 20-45 minutes.

In vitro live-cell time-lapse imaging of neuron-tumor co-cultures

For live-cell experiments, tdTomato or GFP transduced patient-derived glioblastoma cells were seeded onto div7 rat cortical cultures at 1000 cells per well. For glioblastoma monocultures, 1000 cells per well were seeded in 24 well plates containing the same medium as co-cultures, namely Neurobasal (Invitrogen) supplemented with B27 (50x, 2% v/v) and L-glutamine (0.5 mM). Co- and monocultures were imaged at the same div, 4-13 days after seeding. Patient-derived glioblastoma cells were imaged for a period of 12-18 hours at 37 degrees Celsius with 5% CO_2. Images were acquired using a Zeiss LSM780 or a Zeiss CellDiscoverer7 confocal microscope with a fully open pinhole, with a 10x (NA 0.3) (LSM780) or a 20x (NA 0.7) (CD7) air objective or a Nikon Ti-HCS widefield microscope with a 10x air objective (NA 0.3). Acquisition took place every 10 minutes with a pixel size ranging from 346 nm – 794 nm. For proliferation analysis, fields of view were analyzed manually and proliferation rate in percent was determined as cell divisions per hour.

Somatokinetic speed analysis with TrackMate

Fields of view of *in vitro* live-cell imaging data were analyzed with the TrackMate plugin in Fiji (version 7.11.1).[95,99] Cell segmentation was achieved using the deep neural network Cellpose,[123–125] which is integrated into the TrackMate Cellpose[123–125] detector. We trained Cellpose[123–125] models on *in vitro* images analogous to those we intended to segment, utilizing optimal segmentation masks generated via ilastik[97] and further refined through manual corrections.

After training and validating of segmentation models, we employed a custom TrackMate Fiji script.[95,99] We used the integrated Kalman tracker for tracking cell movements. Key parameters were carefully adjusted for each dataset to ensure optimal tracking performance, with the most commonly used settings being an average cell diameter of 30 μm, an initial search radius of 50 μm, a search radius of 30 μm, and a maximum frame gap of 10 frames.

The outputs of this pipeline included information on cell movement within the processed fields of view, as well as overlay stacks for visualizing cell segmentations and tracks over time, and segmentation mask stacks. To effectively filter out tracking errors, we applied a threshold of 10.000 seconds based on track duration, as errors typically resulted in shorter tracks.

Infection lag time analysis

For determination of approximate infection lag time, images from live-cell time-lapse imaging of tumor cells infected at div0 were used. The time point of GB^{Starter} cell infection was manually determined when a TVA-oG-mCherry expressing tumor cell became visually eGFP-positive after rabies virus infection with SAD-B19$^{\Delta G}$-eGFP(EnvA) or CVS-N2c$^{\Delta G}$-eGFP(EnvA). Earliest connected^{TUM} neuron infection was calculated by subtracting time point of visible infection of first connected^{TUM} neuron in vicinity of infected GB^{Starter} from the time point of GB^{Starter} infection. The manually performed analysis was validated with an unbiased machine learning approach using the ilastik auto-context pipeline.[97,126,127] Probability maps of the GFP channel were exported. A cell was rendered positive when the mean gray value in the tumor cell or neuron soma crossed the determined threshold of 10.000.

Drug treatment and radiotherapy in co-cultures

For drug treatment experiments, coverslips were treated with an end concentration of 40μM perampanel 2 hours post glioblastoma cell seeding. Controls were treated with respective amount of DMSO. Coverslips were imaged on the same day of seeding and then 3, 5 and 7 days after seeding using a Zeiss LSM780 microscope with a 10x air (NA 0.3) objective at 37 degrees Celsius with 5% CO_2.

For irradiation experiments, glioblastoma cells were seeded on to div7 rat cortical neurons in 24-well plates (1000 cells/well). For combined perampanel treatment and radiotherapy, coverslips were treated with 40 μM perampanel 2 hours after seeding. 5 days after seeding tumor cells, coverslips were irradiated at 4 Gray. For radiotherapy in combination with retrograde labeling of patient-derived glioblastoma cells, irradiated and control coverslips were infected with CVS-N2c$^{\Delta G}$-eGFP(EnVA) virus (10^3 vg/ml) 6 hours after irradiation. Coverslips were fixed 3 days later and analyzed for input-to-starter ratios (see STAR Methods section "determination of input-to-starter ratios"). For analysis of neuronal subtype distribution of connected^{TUM} neurons of irradiated versus non-irradiated samples, coverslips were stained for CAMK2 or GAD67 in combination with nestin and GFP as described above. Crops were selected randomly and analyzed manually for only GFP positive and GFP and either CAMK2 or GAD67 double positive cells.

Rabies virus-based genetic ablation of connected^{TUM} neurons

Div04 rat cortical neurons were infected with AAV5 virus based on the AAV-flex-taCasp3-TEVp plasmid (Addgene #45580)[80] at a titer of >$7x10^8$ vg/ml. AAV-flex-taCasp3-TEVp was a gift from Nirao Shah & Jim Wells (Addgene plasmid #45580; http://n2t.net/addgene:45580; RRID: Addgene_45580). Five days later, all wells were washed 3x with pre-warmed culture medium (Neurobasal with B27 (50x, 2% v/v) and L-glutamine (0.5mM) before seeding 1000 TVA-oG-mCherry expressing glioblastoma cells per well. 2 hours after seeding, SAD-B19$^{\Delta G}$-Cre-GFP(EnVA) (based on Addgene plasmid #32634) or CVS-N2c$^{\Delta G}$-Cre-GFP(EnVA) was added at a titer of

10^4 vg/ml.[128] Control wells were treated with the same concentration of SAD-B19$^{\Delta G}$-Cre-GFP(EnVA) or CVS-N2c$^{\Delta G}$-Cre-GFP(EnVA) but without prior infection of neuronal cultures with AAV-Flex-TACasp3-TEVP. In conditions with additional drug treatment, wells were treated with either a combination of CNQX (20μM) and TTX (1μM) or Adam10 inhibitor GI254023X (2μM),[82] controls were treated with respective amount of DMSO. 10 days after seeding of tumor cells, infection and drug treatment coverslips were fixed and stained with human-specific anti-nestin to label glioblastoma cells as previously described.[8,16] Quantification was done as described in STAR Methods section "determination of input-to-starter ratios". Different neuronal cohorts were normalized to the mean of the respective control group to account for inter-cohort variability.

Single-cell RNA sequencing

For single-cell RNA sequencing of rabies virus-transduced cultures and their controls, co-cultures of rat cortical cultures and human glioblastoma cells were processed on div6. First, cells were dissociated from coverslips by incubating with Trypsin for 5 minutes. Then, cells were collected in falcon tubes and centrifuged before resuspending in FACS buffer (10% FBS in PBS). DAPI was used at a final concentration of 1 μg/ml as a cell viability marker. Sorting was performed with FACSymphony S6 (BD Biosciences). GB^{Starter} were identified by simultaneous GFP and mCherry fluorescence. Connected^{TUM} neurons were identified by the GFP signal and cells without fluorescence signal were categorized as unconnected^{TUM} microenvironmental cells. The following filters were used: 450/20 for DAPI, 530/30 for GFP and 610/20 for mCherry. Lasers with wavelengths of 405 nm, 488 nm and 561 nm were used for this purpose.

Sequencing pre-processing and analysis

The analysis of the single-cell RNA sequencing data was performed using the R package Seurat (version 5.0.1)[129] unless indicated otherwise. The sequencing data was preprocessed and high-quality rat cells matching the following criteria were analyzed: unique number of transcripts (5.000-11.250), number of reads (100.000-2.000.000), fraction of mitochondrial reads less than 4%. The number of highly variable features was set to 4.000 and data integration was performed using the Seurat method "CCAIntegration". The connected^{TUM} neurons were identified based on the eGFP expression level as measured by FACS.

Identification of cell types

Previously published gene sets were used to identify different cell types and states (annotation level 3).[62] To this end, the expression of a gene set across the clusters was assessed using the Seurat module score function. Astrocytes and oligodendrocytes were identified by a mean module score > 0.1 in the respective gene set, which was in line with the expression of known marker genes. The subanalysis of neurons was performed after excluding astrocytes and oligodendrocytes from the dataset. The identities of cell types present in used co-cultures were also confirmed using immunohistochemistry.

Neuronal subtype classification

For subtype classification of sequenced neurons, genes known for certain neuronal populations were selected based on their expression in our dataset. We observed that glutamatergic and GABAergic neurons were the most prominent subtypes in these cortical cultures and confirmed this finding using immunohistochemistry. Using the AddModuleScore function from Seurat, separate scores were calculated for glutamatergic and GABAergic genes and the cells were annotated based on the dominant module score.

Invasivity module score for single-cell RNA sequencing analyses

Invasivity scores for the different patient-derived glioblastoma models were calculated as described before.[8] Briefly, pseudotime was estimated, with initial cells being designated as SR101-negative invasive cells. Genes exhibiting either positive or negative correlation to pseudotime across cell lines were identified. Following this, the invasivity score was determined by subtracting the Module score of genes negatively correlated from that of positively correlated genes.

Synaptogenic module score for single-cell RNA sequencing analyses

The "Synapse assembly" GO term was downloaded from https://amigo.geneontology.org/amigo/.[64,65] Synaptogenic score was calculated from the list of 117 genes using the AddModuleScore function from Seurat. Score correlations were calculated in R.

DNA methylation profiling of a clinical patient cohort

For analysis, surgically resected tissue of a clinical cohort of 363 patients with IDH-wildtype glioblastoma was analyzed. Informed written consent was obtained from all patients. Experiments were approved by the medical ethics committee of the Hamburg chamber of physicians (PV4904). DNA methylation data was obtained, processed and analyzed as described in detail previously.[61]

Survival analysis

The DNA methylation data was filtered to include only samples present in the metadata. Additional data related to invasivity sites were filtered based on their intersection with the DNA methylation data. The data was then scaled by calculating the mean and standard deviation, followed by grouping the scaled data by genes for invasivity sites to calculate the mean for each group. For the survival analysis, a Cox Proportional Hazards model[130] was fitted using the lifelines library (v0.27.8). The model included the computed scores for invasivity genes, along with relevant metadata columns. The hazard ratios were plotted, and partial effects of the invasivity score on the outcome were visualized.

Single-cell neurotransmitter genes expression analysis

Using the AddModuleScore function from Seurat, a score was calculated for each neurotransmitter group of interest. Genes included for each group can be found in Table S1.

Analysis of publicly available singe-cell RNA sequencing data

Publicly available single-cell RNA sequencing data from various publications were used for analysis.[5,62,66]

TCGA multi-omic data analysis

We merged methylation data (.idat) and gene expression data from the TCGA database[131] which resulted in 100 high quality integrated DNA methylation and gene expression datasets. The invasivity score was computed as described above and correlated with the neuronal score. The neuronal score was computed as described in Drexler et al.[61].

Determination of input-to-starter ratios

Patient-derived glioblastoma spheroids were seeded onto div7 rat cortical neurons following either the direct or the sequential labeling protocol as described above. 8 days later, coverslips were fixed and stained for nestin and GFP as described above.

For input-to-starter ratio analysis of highly invasive as compared to less invasive regions, coverslips were infected with CVS-N2c$^{\Delta G}$-eGFP(EnvA) (10^3 vg/ml) at div5 (highly invasive) or div11 (less invasive) and fixed 3 days after virus application. Coverslips were imaged at a Zeiss AxioScanZ1 microscope with a 20x (NA 0.8) objective and a pixel size of 325 nm.

Cell somata were trained using the ilastik[97] pixel classification pipeline. Probability maps were exported. All further processing steps were performed in Fiji.[95] For quantification of the number of tumor cells per coverslip, probability maps of nestin and DAPI signals were multiplied. Afterwards, the resulting image was auto-thresholded using the "Threshold" function and the number of cells were then determined using the "Analyze Particles" function with a cut-off by a minimum of 20 μm diameter. Auto-thresholding and particle analysis was also performed for the probability map of the eGFP channel. To extract the number of GB^{Starter} cells, thresholded images were multiplied and resulting particles were counted. The number of input cells (connected^{TUM} neurons) were calculated by subtracting the number of GB^{Starter} cells from the number of all eGFP-positive cells.

Ex vivo input-to-starter ratio analysis

For *ex vivo* analysis, brain slices obtained from mice sacrificed 14 days after tumor injection with TVA-oG-mCherry expressing, CVS-N2c$^{\Delta G}$-eGFP(EnvA) infected GB^{Starter} cells from patient-derived glioblastoma models S24 and P3XX. The slices were stained for nestin and GFP as described above. Subsequently, the tumor region for each slice was imaged at a Nikon A1R confocal microscope using a 20x (NA 0.75) objective by creating a z-stack (z-step size: 650 nm) covering the mass of the tumor. Additionally, an overview of each slice was imaged using a Leica Mica microscope with a 10x (NA 0.32) objective by creating a z-stack (z-step size: 4 μm).

Quantification of cells in the tumor region was done by three-dimensional segmentation of the DAPI signal using a custom trained model in Cellpose.[123–125] Further, nestin and GFP signals were isolated by creating probability maps with ilastik.[97] GB^{Starter} cells were determined by overlapping both nestin and GFP signals with the DAPI Cellpose segmentation, whereas input cells were identified by overlapping only the GFP signal with the DAPI Cellpose segmentation and subtracting the nestin signal.

Further, GB^{Starter} and input cells outside the tumor region were manually determined using a maximum intensity projection of the whole slice image.

Cell type analysis of connected^{TUM} neurons

For *ex vivo* analysis, brain slices obtained from mice sacrificed 14-30 days after tumor injection with TVA-oG-mCherry expressing, SAD-B19$^{\Delta G}$-eGFP(EnvA) or CVS-N2c$^{\Delta G}$-eGFP(EnvA)-infected cells from patient-derived glioblastoma spheroids were stained for nestin or mCherry, GFP and a marker of interest from the above listed. Slices were imaged at a Leica DM6000 microscope with a 10x (NA 0.4) objective. Crops were manually analyzed for number of GFP-positive cells, number of marker of interest positive cells and double positive cells.

For *in vitro* quantification, TVA-oG-mCherry expressing, SAD-B19$^{\Delta G}$-eGFP(EnvA) or CVS-N2c$^{\Delta G}$-eGFP(EnvA)-infected cells from patient-derived glioblastoma spheroids were seeded onto div7 rat cortical neurons. 8 days later, coverslips were fixed and stained for nestin, GFP and a marker of interest (used in our study were: NeuN, S100B, MBP, Iba1, CAMK2, GAD67, Parvalbumin, Olig2). Coverslips were imaged at a Zeiss AxioScanZ1 microscope with a 20x (NA 0.8) air objective and a pixel size of 325 nm.

For quantification of DLX-infected connected^{TUM} neurons, div6 rat cortical neurons were treated with AAV-mDlx-NLS-mRuby (Addgene #99130) at a titer of >1x10^9 vg/ml.[132] AAV-mDlx-NLS-mRuby2 was a gift from Viviana Gradinaru (Addgene plasmid #99130; http://n2t.net/addgene:99130; RRID: Addgene_99130). One day later, glioblastoma cells infected with the direct labeling approach were seeded at 1000 cells per well. Coverslips were fixed at tumor cell div8 and quantified as described above.

To rule out unspecific leakage or labeling of rabies virus we performed different control experiments. First, we exchanged medium of wells with TVA-oG-mCherry expressing and SAD-B19$^{\Delta G}$-eGFP(EnvA) or CVS-N2c$^{\Delta G}$-eGFP(EnvA)-infected tumor cell co-cultures of both strains onto wells of only rat cortical neurons and fixed these 8 days after medium exchange. Furthermore, we seeded lysed TVA-oG-mCherry expressing, rabies-infected glioblastoma cells onto div7 rat cortical neurons. Cells were lysed by first exposing them to sterile water and subsequently mechanically lysing them by pipetting them through a 25-gauge needle for 60 seconds.

Cell lysis was confirmed by Trypan-blue staining when counting cells. To perform this control experiment *in vivo*, we injected lysed TVA-oG-mCherry expressing, rabies-infected glioblastoma cells into the cortex. Cells were lysed as described for the co-culture system. Lysed cells were resuspended in the same amount of PBS as the non-lysed $GB^{Starter}$ cells (100.000 cells/μl), which were injected in the same session in separate mice as control.

We could observe in single experiments that the take rate of tumor was low. Similarly, in co-cultures with low-quality neuronal preparation a large portion of $GB^{Starter}$ cells died. In few experiments correlated with the death of $GB^{Starter}$ cells, we observed labeling of cells that fit the morphology of glial cells. These experiments were not included in any analysis in this manuscript.

Expansion microscopy

4x expansion microscopy was performed as described before.[133] Briefly, mouse cortical and iPSC co-cultures with human glioblastoma cells were cultured as described above. Immunohistochemistry was performed as described to stain against GFP and nestin, since endogenous fluorescence is expected to be quenched after expansion. Following immunohistochemistry, coverslips were anchored in 0.1 mg/ml Acryloyl-X SE (AcX) solution in 1x PBS overnight at room temperature. AcX stock solution was 10 mg/ml AcX solved in DMSO. Coverslips were then incubated for 2 hours at 37° C in custom chambers in 100 μl of the gelation solution consisting of 470 μl monomer stock solution for 4xM (0.08 % (v/v) sodium-acrylate (33% wt stock), 2.5% (v/v) acrylamide (50% wt stock), 0.02% (v/v) cross-linker (1% wt stock), 1.9M NaCl (5M stock), 1 ml of 10x PBS, 18.8% (v/v) water) mixed with 10 μl each of 0.5 wt% 4-HT, 10 wt% TEMED and 10 wt% APS. All stock solutions were prepared with water. Incubation chambers were prepared using microscope slides and spacers made from No. 0 coverslips. After incubation, gels were recovered and digested in 8 U/ml Protein-K buffer overnight at room temperature. The gels were then stained with DAPI (1 μg/ml in 1x PBS) for 30 min and washed afterwards for 30 min with 1x PBS. The gels were expanded by washing with MilliQ water 3x 10 min followed by 1x 30 min at room temperature. Expanded gels were mounted on and imaged in poly-L-lysin coated glass bottom dishes.

The scale bars in expansion microscopy images shown in figures were placed after accounting for the expansion factor of 4.

Tissue clearing

Whole brain immunolabeling was performed according to the iDISCO+ protocol.[134] Briefly, samples were dehydrated with a methanol/PBS series (catalog # 8388.2; Carl Roth, Karlsruhe, Germany): 20 vol%, 40 vol%, 60 vol%, 80 vol%, 100 vol% (twice) for one hour each, followed by overnight incubation in 66 vol% Dichloromethane (DCM) (KK47.1, Carl Roth) and 33 vol% methanol. Samples were then washed twice in 100 vol% methanol followed by a bleaching step with 5% H_2O_2 (catalog # LC-4458, Labochem, Sant'Agata li Battiati, Italy) overnight at 4 °C. Rehydration was performed with a methanol/PBS series containing 80 vol%, 60 vol%, 40 vol %, 20 vol%, PBS for 1h each. Lastly samples were washed in 0,2 vol% TritonX-100 (x100, Sigma) in PBS (PTx.2) twice for 1h.

Immunolabeling was performed by incubating pretreated samples in permeabilization solution (400 ml PTx.2, 11.5 g Glycine (catalog # G7126, Sigma), 100 ml DMSO (catalog # A994, Carl Roth) for 2 days at 37° C. Brains were then blocked in blocking solution (42 ml PTx.2, 3 ml Donkey serum, 5 ml DMSO) for 2 days at 37° C. For immunolabeling primary antibodies against GFP (Aves Labs) and against RFP (Rockland) or nestin (Abcam) were applied in PBS, 0,2% Tween-20 (P2287, Sigma) (PTw), 5% DMSO, 3% goat serum for 7 days at 37° C on a rocking platform. Then samples were washed in PTw for 5 times until the next day and incubated with secondary antibodies (goat anti-chicken 488, catalog # A32931, Thermo Fischer and goat anti-rabbit 568, catalog # A11011, Thermo Fischer) in PTw and 3% goat serum for 7 days at 37° C. Samples were wrapped in aluminum foil to prevent photobleaching. Samples were washed in PTw for 5 times until the next day.

Clearing was performed by dehydrating the samples in a methanol/PBS series: 20 vol%, 40 vol%, 60 vol%, 80 vol%, 100 vol% (twice) for one hour each. Followed by 3h incubation in 66 vol% DCM and 33 vol% Methanol, samples were incubated twice in 100 vol% DCM for 15 minutes. Lastly samples were incubated in 33 vol% benzyl alcohol (catalog # 24122, Sigma) and 67 vol% benzyl benzoate (vol/vol; catalog # W213802, Sigma) without shaking.

Unless otherwise stated all steps were performed at room temperature, while shaking. Clearing agents were freshly prepared for each step of the protocol.

Light-sheet microscopy

Cleared samples were imaged with a light-sheet microscope (Ultramicroscope II, Miltenyi Biotec, Heidelberg, Germany) using a 4x objective (MI Plan objective lens 4x, NA 0.35) and combined lasers (excitation wavelength at 470 nm and 560 nm). The in-plane resolution was 1.63 x 1.63 μm with a step size of 5 μm. Images were stitched with a custom-made macro in Fiji.[135]

Calcium imaging of connected^{TUM} and unconnected^{TUM} neurons

6 days after seeding of rat cortical neurons, cultures were infected with AAV.Syn.NES-jRGECO1a.WPRE.SV40 (Addgene #100854).[136] AAV.Syn.NES-jRGECO1a.WPRE.SV40 was a gift from Douglas Kim & GENIE Project (Addgene plasmid #100854; http://n2t.net/addgene:100854; RRID: Addgene_100854). The following day, TVA-oG-mCherry expressing, CVS-N2c$^{\Delta G}$-eGFP(EnvA)-infected glioblastoma cells were seeded at a density of 1000 cells/well. 12 days after seeding, cultures were imaged on a Zeiss LSM980 confocal microscope with a 20x air objective (NA 0.8) with a pixel size of 345.26 nm and a frame interval of 0.52 sec.

Calcium analysis of connected^{TUM} and unconnected^{TUM} neurons

For the analysis of calcium transients, somata of connected^{TUM} and unconnected^{TUM} neurons were marked with circular regions of interest. Mean gray value and center of mass were measured in Fiji[95] for all imaging time points. The exported measurements were further quantified using a custom-written MATLAB script.[8]

Functional neurotransmitter receptor screening

Calcium imaging occurred with triggered neurotransmitter puffing onto the glioblastoma cells. The puffing pipettes were placed approximately 30 μm above the targeted region of interest (ROI). For these recordings, the Patchmaster software (HEKA) was used, with a puff applied every 45 seconds. Puffing stimulations were generated at 10-15 PSI using a Picospritzer. Each recording lasted 225 seconds. Images were acquired with a pixel size of 0.7-1.5 μm at a Leica TCS SP5 microscope using a 20x (NA 0.5) water objective. The recording frequency was 1.56 Hz in a bidirectional acquisition mode.

Puffing pipettes were fabricated from borosilicate capillaries (World Precision Instruments) with a resistance of 2-7 MΩ. All neurotransmitter stocks were prepared with calcium-free artificial cerebrospinal fluid (aCSF). Puffing pipettes were filled with 200 μl of neurotransmitter stock and 0.4 μl of Alexa 594 coloring agent (Invitrogen) to visualize the neurotransmitter puff as control for successful neurotransmitter application during calcium imaging.

Functional neurotransmitter receptor screening occurred by sequentially puffing 8 different neurotransmitters onto a region of interest to determine which trigger a response in glioblastoma cells. A baseline recording with aCSF puffing was used first to exclude regions with a non-neurotransmitter specific response. Next, glutamate puffing (1mM)[137] was performed for 225 seconds and 5 puff stimulations. Further, acetylcholine (1 mM),[138] GABA (gamma-aminobutyric acid, 100 mM),[139] ATP (1 mM),[140] serotonin (5HT, 1.5 mM),[141] adrenaline (1 mM), glycine (2 mM)[142] and dopamine (10 mM)[143] puffing followed under the same conditions.

Pharmacology-related experiments used two baseline recordings with neurotransmitter- and control puffing which were performed as described previously. Next, atropine (50 nM) was washed in for 450 seconds. After the wash-in, a third recording took place with acetylcholine puffing under altered conditions. Atropine was then washed out with aCSF for 450 seconds. Finally, one last calcium imaging time-lapse recording was performed to assess whether the initial response of the cell could be recovered after washing out atropine. Experiments for nicotinic receptor antagonists were performed equivalently, using curare at a concentration of 25 nM.

Calcium imaging analysis

AQuA script in MatLab was used to quantify the event frequency, area, duration, ΔF/F and total calcium entering the cell (Area Under Curve) for each calcium event.[98] Raw images were acquired with two channels, one for the Alexa 594-colored puff, and the other for the calcium event signal. For the semi-automatic AQuA data analysis, the channels were split using a custom Fiji[95] macro and the calcium event channel was analyzed further. Single cells from each region of interest were defined in a user interface and all cells were batch processed using the same detection settings for all files.

Acute brain slice preparation

Acute brain slices for whole-cell electrophysiology were prepared from 8- to 11-week-old NMRI nude 10-14 days after tumor injection with one of the following glioblastoma patient-derived models: S24, T269, BG5 or U3085 expressing TVA-oG-mCherry and either one of the rabies strains CVS-N2c$^{\Delta G}$-eGFP(EnvA) or SAD-B19$^{\Delta G}$-eGFP(EnvA). Mice were perfused transcardially under anesthesia with ice-cold cutting aCSF (composition in mM: 135 NMDG, 20 Choline Bicarbonate, 1 KCl, 1.2 KH_2PO_4, 0.5 $CaCl_2$ x $6H_2O$, 1.5 $MgCl_2$ x $2H_2O$, 12.95 glucose) saturated with 95% O_2, 5% CO_2, at pH 7.4, osmolarity 310 mOsm/L. After decapitation, brains were removed quickly, submerged into ice-cold cutting aCSF and dissected. 300 μm thick coronal sections containing the retrosplenial cortex were obtained using a vibratome (VT1200, Leica Microsystems). After slicing, brain slices were recovered in recording aCSF at 37°C for 45 min and afterwards stored at room temperature in recording aCSF. After usage for electrophysiological recordings, the slices were fixed overnight in 4% (w/v) PFA for further analyses.

Whole-cell patch-clamp electrophysiology

Whole-cell patch-clamp recordings were made from coverslips (recording time points: for co-culture experiments tumor cell div5-12, for neuronal monoculture div14-17, for all irradiation experiments 3-5 days post irradiation) secured under a platinum ring in the recording chamber (OAC-1; Science Products) and submerged in continuously flowing (3 mL/min) aCSF (in mM: NaCl, 125; KCl, 3.5; $CaCl_2$, 2.4; $MgCl_2$, 1.3; NaH2PO_4, 1.2; glucose, 25; $NaHCO_3$, 26; gassed with 96% O_2 and 4% CO_2) maintained at 32–34 °C with an in-line perfusion heater (TC324B; Warner Instruments). Patch electrodes (3-6 MΩ) were pulled from 1.5 mm borosilicate glass. For paired recordings, action potential recordings and postsynaptic current recordings, the following internal solution was used (in mM): KMethylsulphate, 135; EGTA, 0.2; HEPES, 10; KCl, 12; NaCl, 8; Mg-ATP, 2; Na_3-GTP, 0.3. Methylsulphate was used instead of gluconate as the principle intracellular anion to avoid a rundown of both sAHP amplitude and AP accommodation. Data were not corrected for the liquid junction potential of 10.1 mV calculated with JPCalc (RRID:SCR_025044). Recordings were made with two different amplifier systems: A Multiclamp 700B amplifier, digitized through a Digidata 1550B A/D converter and acquired using pClamp 11 software (Molecular Devices) or a HEKA EPC 10 USB amplifier acquired by the Patchmaster software (Heka). Recordings commenced only after passive properties had stabilized and these values were used for analysis. Cells with an access resistance

above 25 MΩ were excluded from analysis. Voltage clamp recordings were sampled at 20 kHz with a low pass filter of 2 kHz. Current clamp recordings were sampled at 250 kHz with a low pass filter of 10 kHz. Pipette, but not whole cell capacitance, was compensated in all recordings. For biotin filling, 0.3% Neurobiotin Tracer from Vector Laboratories was used.

Patch-clamp analysis

Action potential and postsynaptic current analysis was performed in Easy Electrophysiology (RRID:SCR_021190): Rheobase current (the minimal required current injection step needed to evoke an AP), AP threshold, AP amplitude, half width, afterhyperpolarization (AHP) potential amplitude and AHP delay to peak were assessed from the first AP evoked by 1 s depolarizing current injection steps applied in 10 pA increments from a potential of -70 mV maintained by constant current injection. Spontaneous APs or any AP coinciding with current injection onset were excluded from analysis. AP threshold was defined as the point where the first derivative of the voltage trace reached 20 mV/ms during the rising AP phase. AP and AHP amplitudes kinetics were calculated relative to this threshold and rise and decay times represent 10 to 90% of the threshold to peak interval. Input/output functions represent the frequency of APs generated over a depolarizing current injection step of 1 s versus the current injection amplitude (in pA). Mean neuronal excitability was compared by quantifying the integral of the frequency-current curve for each patched neuron independently from the neuronal rheobase.

Miniature postsynaptic currents (mPSCs) were recorded at -70 mV in the presence of TTX (0.5 μM), while spontaneous postsynaptic currents (sPSCs) were recorded at -70 mV without the application of any blocker. Due to the more positive chloride reversal potential (-49 mV), both GABAA receptor-mediated inhibitory mPSCs (mIPSCs) and AMPA receptor-mediated excitatory mPSCs (mEPSCs) were recorded as inward currents distinguishable by their decay times: Events with a decay time (defined as time between the peak and the point at which the event decayed to 37% (1/e)) up to 10 ms and a rise time from 0.5 to 5 ms were defined as mEPSCs, while events with a decay time longer than 12 ms and a rise time from 0.5 to 15 ms were defined as mIPSCs. Thresholds for decay times were established from recordings in the presence of the GABAA receptor antagonist gabazine (5 μM), or the AMPA-receptor blocker 2,3-dihydroxy-6-nitro-7-sulfamoyl-benzo[f]quinoxaline (NBQX, Hello Bio, 5 μM) (n = 4 cells each). Events were detected via template matching after filtering with a 2000 Hz Bessel low-pass filter while a minimum amplitude threshold of 5 pA was used to exclude noise (RMS noise was < 5 pA). All events were fit with a biexponential function and visually verified. Decay kinetics were fit with a single exponential function with the formula:

$$I_{membrane} = A_0 + A_1\left(e^{-\frac{t}{\tau}}\right)$$

where $I_{membrane}$, represents the membrane current, A_0 and A_1 represent the mean baseline current and slope parameter and τ the decay time constant.

Spontaneous network activity was evaluated from 3-5 min long current-clamp recordings without any holding current. EPSP bursts (>500 ms and >5 mV with multiple synaptic events) and APs were counted manually. Burst depolarization per second was calculated from the mathematical integral of the difference between the baseline membrane potential outside burst events (Savitzky-Golay smoothed) and the lower envelope of the EPSP burst after smoothing (500 point) to remove any APs. SIC and AP burst envelope decay kinetics were analyzed in cells with large and clean single peak responses and expressed as weighted tau values from biexponential fits using the following formula:

$$I_{membrane} = A_0 + A_1\left(e^{-\frac{t}{\tau_1}}\right) + A_2\left(e^{-\frac{t}{\tau_2}}\right)$$

$$\tau_{weighted} = \tau_1\left(\frac{A1}{A1+A2}\right) + \tau_2\left(\frac{A2}{A1+A2}\right)$$

To investigate how physiological characteristics of connected^{TUM} neurons differ to those of unconnected^{TUM} neurons or neurons without the proximity of tumor cells we performed whole-cell patch-clamp electrophysiology of tumor-bearing and non-tumor-bearing mice using acute brain slices as described above. We used four PDX models (S24, T269, BG5, U3085) 10-14 days after tumor implantation to also evaluate potential patient-dependent differences. First, we investigated basic membrane properties between these groups and saw no apparent differences in resting membrane potential or input resistance between connected^{TUM} and unconnected^{TUM} neurons, also between the different PDX models. When compared to control non-tumor-bearing mice, we observed the input resistance was significantly higher in neurons from tumor-bearing mice, which potentially indicates overall differences of the tumor microenvironment on neurons, as we could not see these differences between connected^{TUM} and unconnected^{TUM} neurons.

The frequency of action potentials induced by current injections above the rheobase in connected^{TUM} neurons was comparable to that of unconnected^{TUM} neurons. Neurons from PDX mice showed a lower frequency of induced action potentials compared to control neurons. This reduction in action potential frequency, indicating a relative hypoexcitability of neurons in PDX models, could be due to the presence of glioblastoma in its early stages. This might be a phenomenon that potentially precedes neuronal hyperexcitability in later stages and will need further investigation.

When investigating the synaptic connectivity measured in the form of spontaneous excitatory and inhibitory synaptic currents, we did not find significant difference across all groups, apart from an increased amplitude in sEPSC between connected^{TUM} and unconnected^{TUM} neurons, yet both did not differ to control neurons of non-tumor-bearing mice.

Electrophysiological characterization with high-density microelectrode arrays

Recordings were performed on multi-well high-density microelectrode arrays (HD-MEAs) available from MaxWell Biosystems (MaxTwo system, Zurich, Switzerland).[144] Before plating, HD-MEAs underwent sterilization using 70% ethanol for 30 minutes, followed by three successive rinses using distilled water. For enhanced tissue attachment, the arrays were treated with a coating of 0.05% poly(ethyleneimine) (Sigma-Aldrich), prepared in borate buffer at a pH of 8.5 (Thermo Fisher Scientific, Waltham, USA). This coating process was carried out for 30 minutes at room temperature. Subsequently, the arrays were rinsed again with distilled water and then allowed to air dry.

Embryonic day (E) 18 rat primary cortical neurons were prepared as described previously.[144] Neurons were seeded at a density of 20-30.000 cells per chip in plating medium, which contained 450 mL Neurobasal (Invitrogen, Carlsbad, CA, United States), 50 mL horse serum (HyClone, Thermo Fisher Scientific), 1.25 mL Glutamax (Invitrogen), and 10 mL B-27 (Invitrogen). Primary cultures were housed in culture incubators at 37C/5% CO_2. After two days, the plating medium was gradually changed to maintenance medium, which contained BrainPhys and SM1 (STEMCELL Technologies, Vancouver, #05792); half of the media was exchanged every 2–3 days.

On div7, an activity scan was performed to screen for active electrodes on the HD-MEA and to select a suitable recording configuration for the tracking experiment. Up to 1024 read-out channels were selected based on the action potential amplitude values estimated during the activity scan. Next, tumor cells were dissociated and seeded onto the primary culture for co-culture. Starting from div7 onwards, co-cultures were recorded every 1–2 days until div12 with the same network recording configuration (recording duration: 30-60 minutes). No media changes were performed during this period.

Results were obtained from a total of 4 controls and 8 neuron/tumor co-cultures, using multi-unit activity. The firing rate was estimated for all active channels (minimum firing rate: 0.05 Hz), and averaged over the full array. The bursts were detected on binned spike train activity (1 second bins), using an adaptive threshold based on the activity of each well (peaks above the mean + 1.5 standard deviation of the binned population activity).

Cluster analysis of connected^{TUM} neurons over time

First, GFP and nestin signals were segmented using ilastik.[97] Starter cells were calculated by overlapping the segmented GFP and nestin signals. Input cells were identified by subtracting starter cells from the total GFP signal. We extracted the coordinates of the input and starter cells. In further analysis, we utilized MATLAB to conduct clustering using the Density-Based Spatial Clustering of Applications with Noise (DBScan) algorithm.[145] Distances between starter cells, input cells, and the resulting clusters were calculated. Cluster boundaries were represented by convex hulls for enhanced delineation. Within each cluster, we evaluated the input-to-starter ratio to assess the distribution and composition of input cells relative to starter cells.

Whole brain atlas mapping of tumor cells and connected^{TUM} neurons

To register and analyze brain sections, we used the QUINT workflow consisting of three steps.[146] First, the sections were registered to Allen Mouse Brain Common Coordinate Framework (CCF).[147] Sections were then preprocessed and segmented for quantification.

Data Acquisition and Preparation

Brain sections from experimental mice were acquired using a Zeiss AxioScanZ1 microscope with a 20x (NA 0.8) objective or Leica Mica with a 20x (NA 0.75) objective. Sections were stained with DAPI (1:10000 v/v in 1x PBS) prior to acquisition. The endogenous mCherry was used to identify glioblastoma cells and connected^{TUM} neurons were identified by their GFP expression without mCherry expression.

Image Registration and Processing

The aligned image series was registered to the atlas using QuickNII and VisuAlign tools[148] to ensure accurate alignment across different brain sections. QuickMASK tool was utilized for generating masks corresponding to left-right hemisphere delineations.

Tumor and Connected^{TUM} Neuron Analysis

The main tumor was manually defined. These ROIs were cleared from the GFP signal. DAPI and GFP signals were separately trained in ilastik[97] to segment nuclei and connected^{TUM} neurons, respectively. To calculate the number of connected^{TUM} neurons, nuclei of connected^{TUM} neurons were calculated by multiplying the segmented GFP and DAPI channels. Subsequently, the centroids of these nuclei were extracted.

Quantification and Visualization

The Nutil tool was used to quantify GFP-positive nuclei across different brain regions.[149] Main tumor site and GFP-positive, connected^{TUM} neurons were visualized in 3D using MeshView,[148] providing insights into their spatial distribution and connectivity patterns.

Distance Determination and Plotting

Using the coordinates of each centroid of GFP-positive nuclei, the distances of connected^{TUM} neurons to the tumor mass were determined separating ipsilateral and contralateral hemispheres. Distances to tumor, differences across hemispheres, and cell distribution were quantified and visualized for each experimental group.

Stochastic neurotransmitter and cell class determination of connected^{TUM} neurons

To identify specific neurotransmitters and neuron classes connected to the tumor, we used the MERFISH spatial transcriptomics dataset of a single adult mouse brain (Zhuang-ABCA-1) containing 4.2 million cells.[150] First, we used the metadata dataset of the MERFISH analysis (cell_metadata_with_cluster_annotation.csv) which contains specific information about each cell such as neurotransmitter and class. We linked these metadata to a second dataset (ccf_coordinates.csv) which contains spatial information of each cell. Because our connected^{TUM} neurons were registered to Allen-CCF-2017 and the MERFISH dataset was registered to Allen-CCF-2020, we had to convert the parcellation indices of Allen-CCF-2020 to the parcellation indices of Allen-CCF-2017. We excluded all cells from the MERFISH dataset that did not contain any information on neurotransmitters to select only neurons. Next, we stochastically assigned within each parcellation index specific information of the MERFISH dataset such as neurotransmitter and class to each cell of our spatial characterization of connected^{TUM} neurons.

To pair the datasets of day 14 and day 30 mice, we stochastically reduced both datasets to a number of 1000. We first paired every neurotransmitter or class to the same neurotransmitter or class if possible. When this was no longer possible, the rest was paired by chance. For clarity, we excluded classes and neurotransmitters that were below 0.1%.

Ex vivo magnet resonance imaging

MR scans were conducted using a 9.4 Tesla horizontal bore small animal MRI scanner (BioSpec 94/20 USR, Bruker BioSpin GmbH, Ettlingen, Germany) equipped with a gradient strength of 675 mT/m and a receive-only 4-channel surface array coil. T2-weighted images of *ex vivo* brain samples were acquired using a 3D TurboRARE sequence (TE: 78.9 ms, TR: 1800 ms, spatial resolution: 0.1 x 0.1 x 0.1 mm^3, Field of view: 15 x 20 x 10 mm^3, matrix: 150 x 200 x 100, averages: 1, flip angle: 180°, RARE factor: 25, duration of acquisition: 12min 0s).

General image processing and visualization

Image processing was primarily performed in Fiji (e.g. to reduce and remove unspecific background by subtraction of different channels, filtering with a median filter or the 'Remove Outliers' function).[95]

Arivis Vision 4D and Fiji[95] were used for 3D and 4D image visualization. Probability maps were created for further analysis and visualization using ilastik.[97] For all 3D renderings in Arivis Vision 4D, probability maps were used. Confocal laser scanning microscopy (CLSM) images and *in vivo* imaging data were denoised using the denoise.ai pretrained model in the Nikon NIS-Elements AR software v5.30.01 (Nikon GmbH Germany/Laboratory Imaging) when indicated. Videos were produced in DaVinci Resolve 17.

QUANTIFICATION AND STATISTICAL ANALYSIS

Quantification results were analyzed in GraphPad Prism (GraphPad Software) or R to test statistical significance with the respective tests. Data were first analyzed for normality using D'Agostino and Pearson normality. For normally distributed data, statistical significance was determined by using the two-sided Students' t-test. In the case of non-normality, Mann-Whitney test was used. For more than 2 groups, normally distributed data were analyzed using one-way ANOVA and non-normally distributed data were analyzed with a Kruskal-Wallis (unpaired) or Friedman (paired) test and corrected for multiple testing. For two or more groups observed over consecutive time points, a two-way ANOVA test was performed. If the p value was below 0.05, results were considered statistically significant. Manual quantifications were performed by at least two independent investigators. Animal group sizes were kept as low as possible. No statistical methods were used for predetermining sample size. Quantifications were depicted with mean and standard error of means. All p values of graphs with multiple comparisons missing for clarity reasons can be found in Table S1.

CellPress
OPEN ACCESS

Supplemental figures

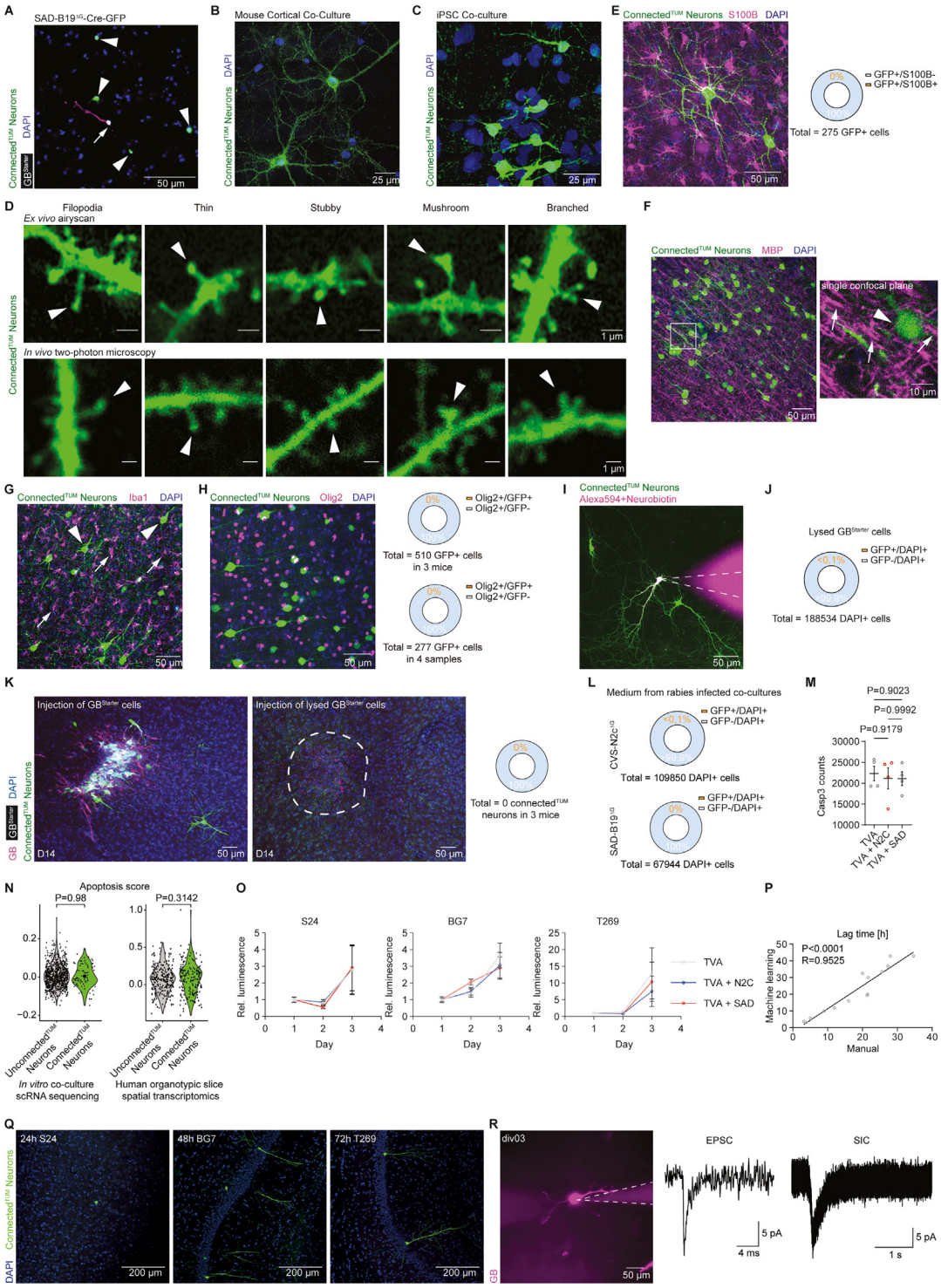

(legend on next page)

Figure S1. Specific labeling of connected^{TUM} neurons with rabies-based tracing and early integration of glioma cells, related to Figure 1

(A) PM of SAD-B19$^{\Delta G}$-Cre-GFP and TVA-oG-mCherry-positive S24 GB^{Starter} cell (arrow) with SAD-B19$^{\Delta G}$-Cre-GFP-infected connected^{TUM} neurons (arrowheads) in co-culture.

(B) Expansion microscopy of mouse cortical co-culture showing connected^{TUM} neurons in green (CVS-N2c$^{\Delta G}$-eGFP(EnvA), patient-derived model S24).

(C) Expansion microscopy PM of iPSC neuron co-culture showing connected^{TUM} neurons in green (CVS-N2c$^{\Delta G}$-eGFP(EnvA), patient-derived model S24).

(D) Dendritic spine classes can be distinguished in connected^{TUM} neurons (green) in PDX model S24 as shown with *ex vivo* Airyscan imaging (SAD-B19$^{\Delta G}$-eGFP(EnvA), top) and IV2PM (CVS-N2c$^{\Delta G}$-eGFP(EnvA), bottom). Arrowheads point to dendritic spines matching the respective class.

(E) *Ex vivo* maximum intensity projection of confocal microscopy from connected^{TUM} neurons (SAD-B19$^{\Delta G}$-eGFP(EnvA), green) and non-infected, S100B-positive astrocytes (magenta) in PDX model S24. No connected^{TUM} cells showed positive S100B signal (n = 275 cells in co-cultures of n = 9 patient-derived models).

(F) *Ex vivo* confocal maximum intensity projection showing connected^{TUM} neurons (CVS-N2c$^{\Delta G}$-eGFP(EnvA), green) and non-infected, MBP-positive oligodendrocytes (magenta) in PDX model S24 (left). Zoom-in on a single confocal plane showing no overlap between connected^{TUM} neurons (arrowhead) and MBP (arrows, right).

(G) *Ex vivo* maximum intensity projection of confocal microscopy showing connected^{TUM} neurons (CVS-N2c$^{\Delta G}$-eGFP(EnvA), green, arrowheads) and non-infected, Iba1-positive microglia (magenta, arrows) in PDX model S24.

(H) Representative *ex vivo* maximum intensity projection of confocal microscopy showing no overlap between Olig2, a marker for cells of the oligodendroglial lineage, and connected^{TUM} neurons (left). Quantification of GFP-positive and mCherry-negative connected^{TUM} neurons for Olig2 positivity *ex vivo* (n = 510 cells from 3 mice, right, top). Quantification of GFP-positive and mCherry-negative connected^{TUM} neurons for Olig2 positivity *in vitro* (n = 277 cells from 4 samples, right, bottom).

(I) Representative image of whole-cell patch-clamp of connected^{TUM} neuron (CVS-N2c$^{\Delta G}$-eGFP(EnvA)), patch pipette (dashed line) filled with Alexa 594 and neurobiotin (patient-derived model S24).

(J) Control experiment of lysed S24 GB^{Starter} cells on cortical cultures. Less than 0.1% of cells in co-culture are infected (n = 18 of 188,534 cells total).

(K) Representative *ex vivo* maximum intensity projection of confocal microscopy images showing GB^{Starter} cells and their connected^{TUM} neurons following GB^{Starter} injection (left) compared with injection of lysed GB^{Starter} cells (right). Dashed circle indicates the injection site. No connected^{TUM} neurons were observed in n = 3 mice.

(L) Culture medium from rabies-infected co-cultures on neuronal cultures. Quantifications show less than 0.1% of cells in culture are rabies-infected for both cultures infected with the CVS-N2c$^{\Delta G}$-eGFP(EnvA) (top) and the SAD-B19$^{\Delta G}$-eGFP(EnvA) (bottom) strains (n = 2 of 109,850 cells total for CVS-N2c$^{\Delta G}$, n = 0 of 67,944 cells total for SAD-B19$^{\Delta G}$ in patient-derived model S24).

(M) Quantification of cleaved caspase 3 signal in cortical co-cultures containing GB cells with no rabies virus compared with the CVS-N2c$^{\Delta G}$-eGFP(EnvA) or the SAD-B19$^{\Delta G}$-eGFP(EnvA) strains (n = 4 samples each, one-way ANOVA).

(N) Expression of apoptosis-related genes in connected^{TUM} versus unconnected^{TUM} neurons in a single-cell RNA sequencing dataset of co-cultures (left) and in a spatial transcriptomics dataset of human organotypic slices (right, n = 811 unconnected^{TUM} versus 97 connected^{TUM} neurons for co-culture and n = 254 unconnected^{TUM} versus 177 connected^{TUM} neurons for human organotypic slices, Wilcoxon test for both plots).

(O) CellTiter-Glo assay of patient-derived GB models S24 (left), T269 (middle), and BG7 (right) comparing the relative luminescence of only TVA-oG-mCherry-expressing cells (gray), SAD-B19$^{\Delta G}$-eGFP(EnvA) rabies-infected and TVA-oG-mCherry-expressing cells (red), and CVS-N2c$^{\Delta G}$-eGFP(EnvA) rabies-infected and TVA-oG-mCherry-expressing cells (blue) (n = 7 replicates for each condition in S24, n = 5 replicates for each condition in BG5, n = 7 replicates for only TVA-oG-mCherry and TVA-oG-mCherry with CVS-N2c$^{\Delta G}$-eGFP(EnvA) conditions in T269 and n = 5 replicates for TVA-oG-mCherry with SAD-B19$^{\Delta G}$-eGFP(EnvA)).

(P) Correlation plot of lag time between GB^{Starter}-connected^{TUM} neuron pairs as analyzed via manual annotation and interactive machine learning (n = 14 GB^{Starter}-connected^{TUM} neuron pairs).

(Q) *Ex vivo* maximum intensity projections of confocal microscopy 24 (left), 48 (middle), and 72 h (right) after GB^{Starter} cell injection in PDX models S24, BG7, and T269 showing connected^{TUM} neurons.

(R) Image of S24 GB cell in whole-cell patch-clamp recording 3 days after seeding onto neuronal cultures (left) and exemplary EPSC and SIC traces. Post processed using denoise.ai.

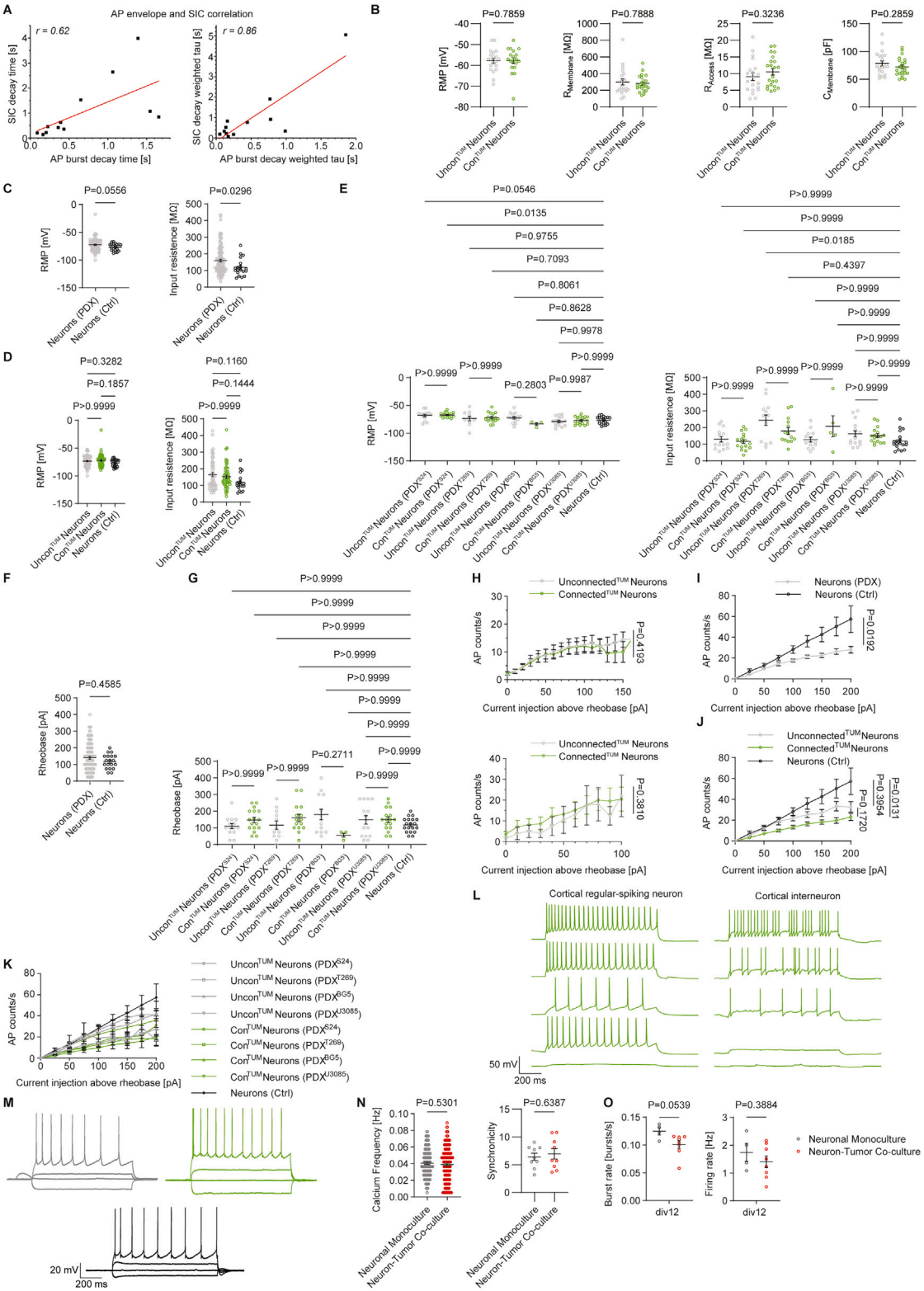

Figure S2. Electrophysiological properties of connected^{TUM} and unconnected^{TUM} neurons, related to Figure 2

(A) Connected^{TUM} AP envelope and GB^{Starter} SIC current correlation, showing correlation between decay times (left, Pearson's r = 0.62, ANOVA F (df) = 6.4 (11), p = 0.0301) and decay weighted tau (right, Pearson's r = 0.86, ANOVA F (df) = 29.6 (11), p = 0.00029) (n = 12 pairs).

(legend continued on next page)

(B) Passive membrane properties in currents in unconnected^{TUM} (n = 20) and connected^{TUM} (n = 22) cortical co-culture neurons: resting membrane potential (RMP, Mann-Whitney test), membrane resistance ($R_{Membrane}$, unpaired t test), access resistance (R_{Access}, unpaired t test), and membrane capacitance ($C_{Membrane}$, unpaired t test).

(C) Quantification of resting membrane potential (n = 111 PDX, n = 19 control, Kruskal-Wallis test) and input resistance (n = 109 PDX, n = 19 control, Kruskal-Wallis test) in patched PDX and control neurons.

(D) Quantification of resting membrane potential and input resistance in neurons from PDX and control mice (n = 56 unconnected^{TUM} neurons, n = 55 connected^{TUM} neurons, n = 19 control neurons, Kruskal-Wallis test).

(E) Quantification of resting membrane potential (n = 14 $PDX^{S24,\ unconnected}$, n = 17 $PDX^{S24,\ connected}$, n = 10 $PDX^{T269,\ unconnected}$, n = 16 $PDX^{T269,\ connected}$, n = 15 $PDX^{BG5,\ unconnected}$, n = 4 $PDX^{BG5,\ connected}$, n = 16 $PDX^{U3085,\ unconnected}$, n = 18 $PDX^{U3085,\ connected}$, n = 19 control neurons, one-way ANOVA) in neurons from PDX and control mice (left). Quantification of input resistance (n = 14 $PDX^{S24,\ unconnected}$, n = 17 $PDX^{S24,\ connected}$, n = 13 $PDX^{T269,\ unconnected}$, n = 14 $PDX^{T269,\ connected}$, n = 13 $PDX^{BG5,\ unconnected}$, n = 5 $PDX^{BG5,\ connected}$, n = 16 $PDX^{U3085,\ unconnected}$, n = 17 $PDX^{U3085,\ connected}$, n = 19 control neurons, Kruskal-Wallis test) in neurons from PDX and control mice (right). All p values can be found in Table S1.

(F) Neuronal rheobase in patched neurons from PDX and control mice (n = 108 PDX, n = 19 control, Mann-Whitney test).

(G) Neuronal rheobase in connected^{TUM} compared with unconnected^{TUM} neurons from different PDX lines (n = 14 $PDX^{S24,\ unconnected}$, n = 17 $PDX^{S24,\ connected}$, n = 12 $PDX^{T269,\ unconnected}$, n = 15 $PDX^{T269,\ connected}$, n = 13 $PDX^{BG5,\ unconnected}$, n = 4 $PDX^{BG5,\ connected}$, n = 16 $PDX^{U3085,\ unconnected}$, n = 17 $PDX^{U3085,\ connected}$, n = 19 control neurons, Kruskal-Wallis test). All p values can be found in Table S1.

(H) Input-output relationship between the current injected (relative to the rheobase current) and the number of action potentials generated over 1 s in connected^{TUM} (n = 10) and unconnected^{TUM} (n = 9) regular-spiking neurons in cortical co-cultures (top, unpaired t test). Input-output relationship between the current injected (relative to the rheobase current) and the number of action potentials generated over 1 s in connected^{TUM} and unconnected^{TUM} intermittent-spiking neurons (n = 8 each) in cortical co-cultures (bottom, Mann-Whitney test). Quantification was done by the area under the curve (STAR Methods).

(I) Induced action potential frequency in dependence of the neuronal rheobase in neurons from PDX and control mice, quantified by the area under the curve (STAR Methods) (n = 113 PDX, n = 18 control, Mann-Whitney test).

(J) Induced action potential frequency in dependence of the neuronal rheobase in unconnected^{TUM}, connected^{TUM} neurons, and control neurons quantified by a comparison of the area under the curve (STAR Methods) (n = 61 unconnectedTUM, n = 52 connected^{TUM}, n = 18 control neurons, Kruskal-Wallis test).

(K) Induced action potential frequency in dependence of the neuronal rheobase in neurons from unconnected^{TUM} and connected^{TUM} neurons split between different PDX models, quantified by a comparison of the area under the curve (STAR Methods) (n = 14 PDX^{S24}, unconnected, n = 17 PDX^{S24}, connected, n = 12 PDX^{T269}, unconnected, n = 14 PDX^{T269}, connected, n = 14 PDX^{BG5}, unconnected, n = 4 PDX^{BG5}, connected, n = 16 PDX^{U3085}, unconnected, n = 17 PDX^{U3085}, connected, n = 18 control neurons, Kruskal-Wallis test, p values can be found in Table S1).

(L) Representative whole-cell current-clamp recordings of action potential firing in connected^{TUM} cortical regular- and intermittent-spiking neurons after 10, 50, 100, 150, and 200 pA current step injection.

(M) Representative voltage changes and action potential firing after −100, 0, 50, and 100 pA injection over a duration of 1,000 ms in an *ex vivo* cortical control (black), unconnected^{TUM} (gray), and connected^{TUM} (green) neuron.

(N) Calcium transient frequency (left) and synchronicity (right) of neuronal monoculture and cultures with seeded GB cells (n = 157 for monoculture and 160 for co-culture cells in 9 regions of interest, Mann-Whitney test [frequency] and unpaired t test [synchronicity]).

(O) Burst rate in bursts/s (left) and firing rate in Hz (right) of cultures without tumor cells and cultures with GB (n = 4 monocultures and 8 co-cultures, unpaired t test).

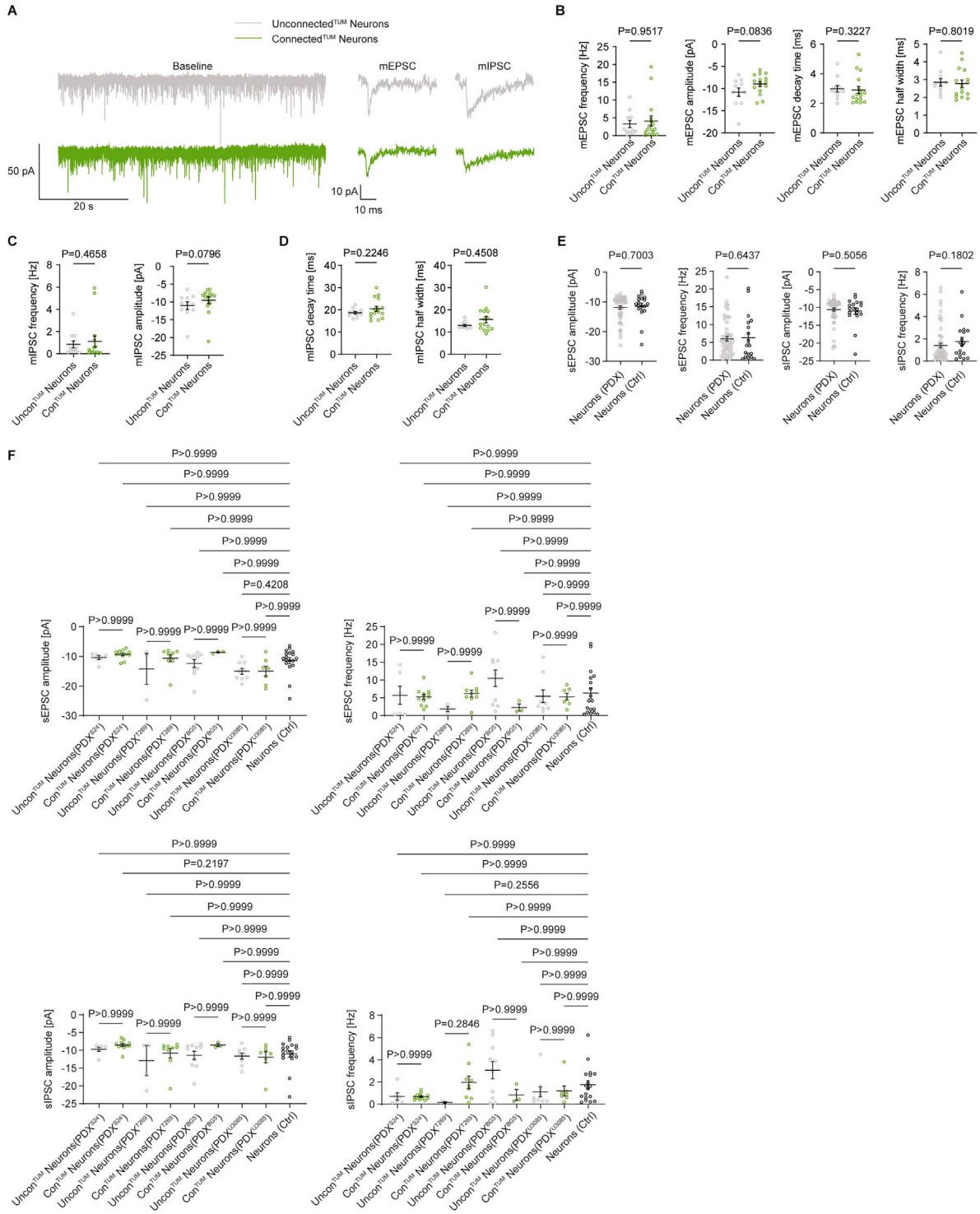

Figure S3. Synaptic connectivity of connected^{TUM}, unconnected^{TUM}, and control neurons, related to Figure 2

(A) Representative whole-cell voltage-clamp recordings of miniature postsynaptic currents in unconnected^{TUM} and connected^{TUM} cortical co-culture neurons with representative single mEPSC and mIPSC examples.

(B) Postsynaptic mEPSC properties in unconnected^{TUM} (n = 11) and connected^{TUM} (n = 16) cortical co-culture neurons: mEPSC frequency (Mann-Whitney test), amplitude (unpaired t test), decay time (Mann-Whitney test), and half width (unpaired t test).

(C) Postsynaptic mIPSC frequency (Mann-Whitney test) and amplitude (unpaired t test) in unconnected^{TUM} (n = 11) and connected^{TUM} (n = 16) cortical co-culture neurons.

(legend continued on next page)

(D) Postsynaptic mIPSC decay time (unpaired t test) and half width (Mann-Whitney test) in unconnected^{TUM} (n = 11) and connected^{TUM} (n = 16) cortical co-culture neurons.

(E) Quantification of sEPSC amplitude, sEPSC frequency, sIPSC amplitude, and sIPSC frequency in neurons from PDX and control mice (n = 59 PDX neurons, n = 18 control neurons, Mann-Whitney test for every parameter).

(F) Quantification of sEPSC amplitude, sEPSC frequency, sIPSC amplitude, and sIPSC frequency in neurons from control mice and different PDX mice (n = 6 PDX$^{S24,\ unconnected}$, n = 12 PDX$^{S24,\ connected}$, n = 3 PDX$^{T269,\ unconnected}$, n = 9 PDX$^{T269,\ connected}$, n = 10 PDX$^{BG5,\ unconnected}$, n = 3 PDX$^{BG5,\ connected}$, n = 9 PDX$^{U3085,\ unconnected}$, n = 7 PDX$^{U3085,\ connected}$, n = 18 control neurons, Kruskal-Wallis test). All p values can be found in Table S1.

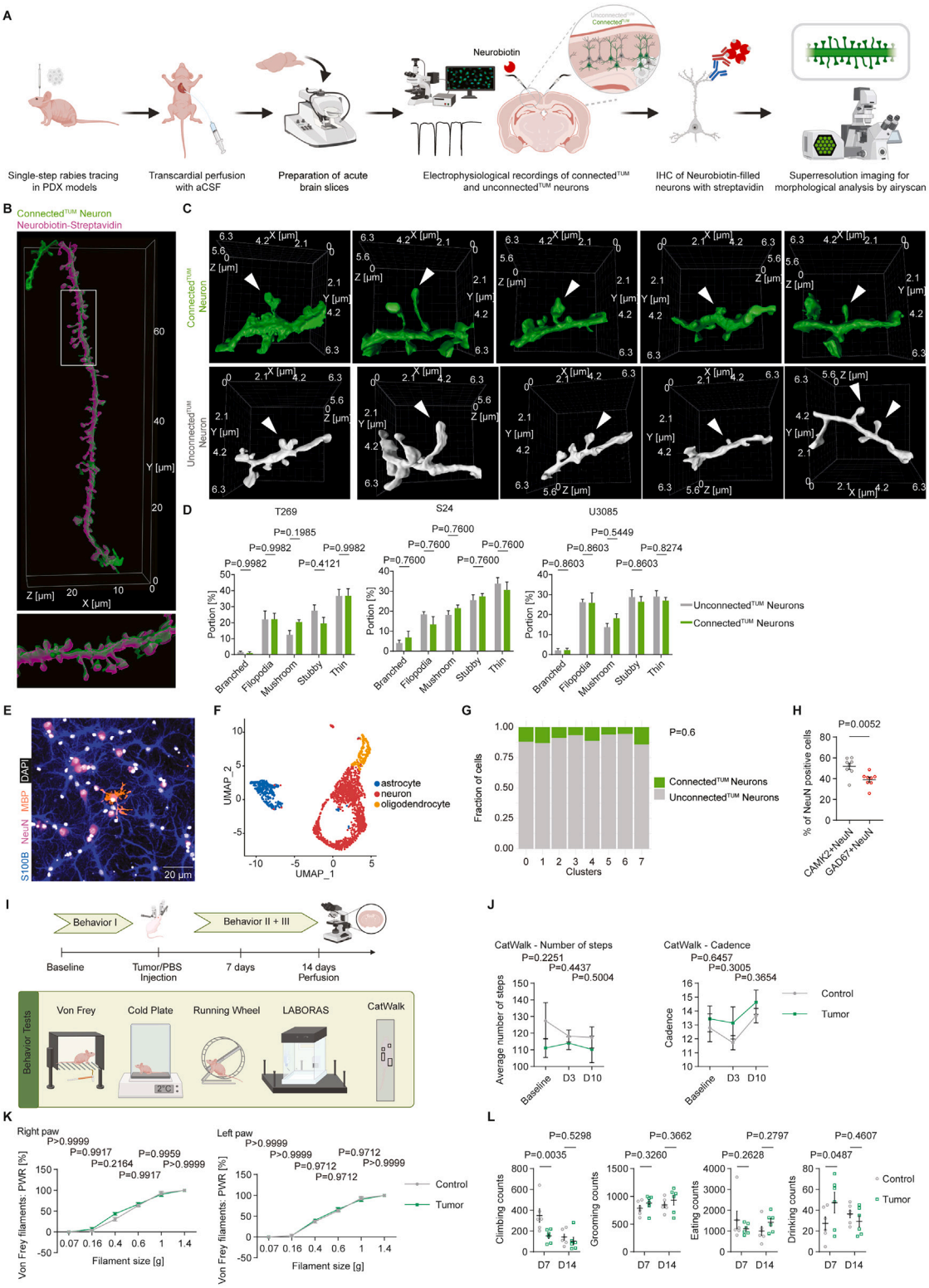

Figure S4. Dendritic plasticity, molecular characteristics, and behavioral consequences of unconnected^{TUM} and connected^{TUM} neurons, related to Figure 3

(A) Schematic workflow of whole-cell patch-clamp electrophysiology combined with neurobiotin filling of recorded cells. Patched cells were stained with streptavidin 647 and subsequently imaged using confocal Airyscan microscopy.

(legend continued on next page)

(B) 3D rendering of a neurobiotin-filled and stained connected^{TUM} basal dendrite.
(C) 3D rendering of different spine types: branched, filopodia, mushroom, stubby, and thin, respectively, in connected^{TUM} and unconnected^{TUM} neurons in the PDX model T269. Arrowheads showing respective spine type.
(D) Grouped bar plots of normalized classified spines per dendritic stretch in PDX models T269, S24, and U3085 (n = 6 dendritic stretches from 3 unconnected^{TUM} neurons and 5 dendritic stretches from 4 connected^{TUM} neurons [T269], n = 8 dendritic stretches from 6 unconnected^{TUM} neurons and 2 dendritic stretches from 1 connected^{TUM} neuron [S24], n = 8 dendritic stretches from 5 unconnected^{TUM} neurons and 6 connected^{TUM} dendritic stretches from 4 connected^{TUM} neurons [U3085], multiple unpaired t tests for T269 and S24, multiple Mann-Whitney tests for U3085).
(E) Representative image showing the cell types present in co-culture. The main portion of the cells found are S100B-positive astrocytes (blue), NeuN-positive neurons (magenta), and MBP-positive oligodendrocytes (orange).
(F) Uniform manifold approximation and projection (UMAP) of the sequenced co-cultures after quality control showing the cell-type annotation of the different microenvironmental cell types in co-culture (n = 1,958 cells).
(G) Distribution of connected^{TUM} and unconnected^{TUM} neurons across clusters showing no significant differences (n = 97 connected^{TUM} neurons and 811 unconnected^{TUM} neurons, Fischer test (10^5 simulations]).
(H) Quantification of the neuronal subtypes in co-culture based on IHC using GAD67 and CAMK2 staining paired with NeuN (n = 8 samples for each group, unpaired t test).
(I) Schematic of performed experiments evaluating motor and sensory capacity as well as general behavior of tumor-bearing versus non-tumor-bearing mice.
(J) Number of steps and cadence (from left to right) of tumor versus control mice (n = 6 mice for each group, two-way ANOVA with post hoc Tukey test for both).
(K) Paw withdrawal rate of the right hind paw (left) and left hind paw (right) with a variety of different filament sizes in control versus tumor mice (n = 6 for each group, two-way ANOVA with Sidak's test).
(L) Counts for climbing, grooming, eating, and drinking as observed in a LABORAS observation cage over a period of 24 h in control versus tumor mice (n = 6 mice for each group, two-way ANOVA with Fisher's LSD for all).

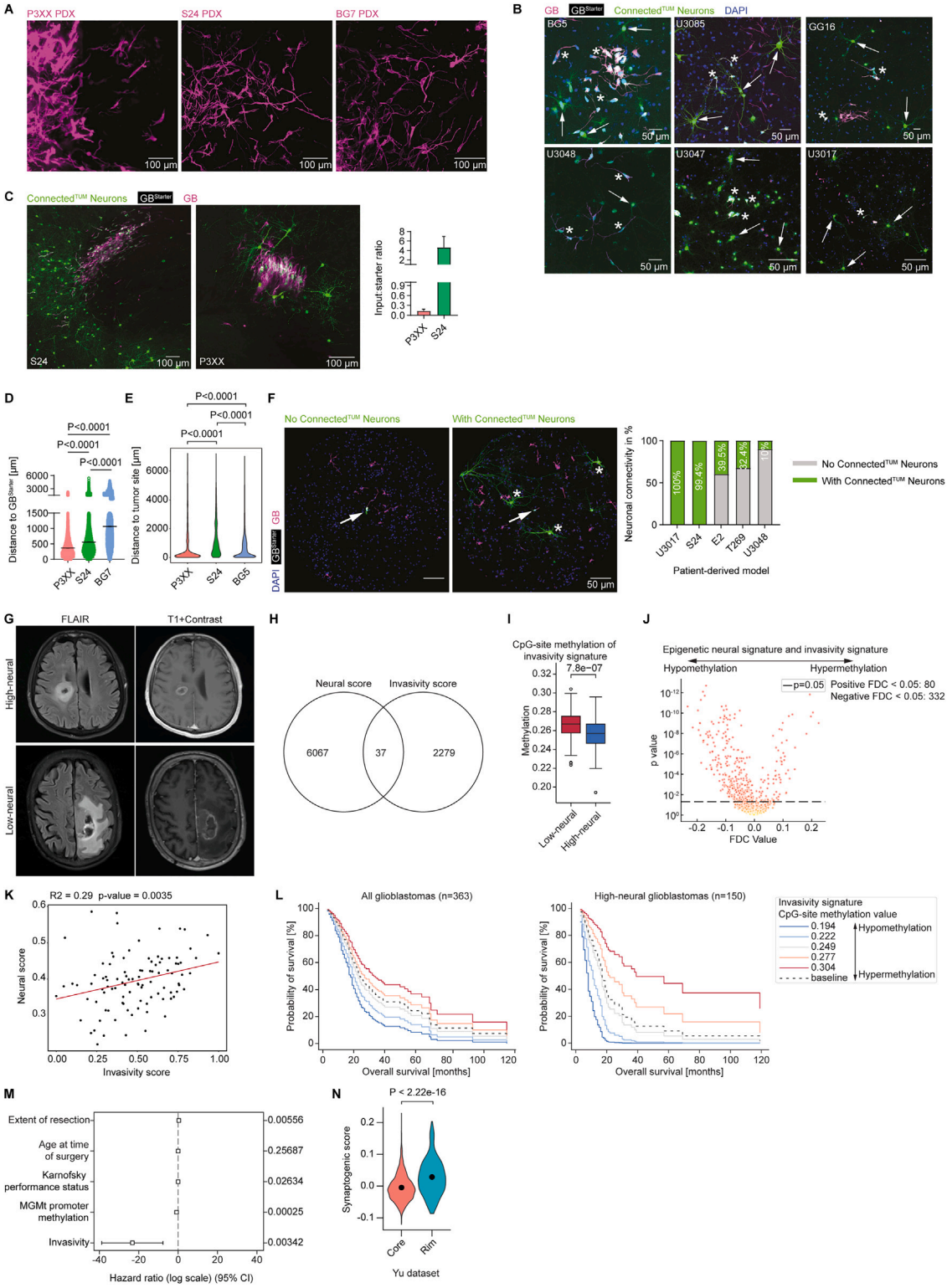

Figure S5. Patient-specific neuronal connectivity, related to Figure 4

(A) IV2PM of 3 different PDX models: P3XX (left), S24 (middle), and BG7 (right). Post processed with denoise.ai.

(B) Neuronal connectome of different patient-derived glioblastoma models in co-culture. Representative images showing $GB^{Starter}$ cells (white, asterisks) and their $connected^{TUM}$ neurons (green, arrows) (CVS-N2c$^{\Delta G}$-eGFP(EnvA) for BG5, GG16, U3048MG; SAD-B19$^{\Delta G}$-eGFP(EnvA) for U3085, U3047, U3017 [green]).

(legend continued on next page)

(C) Representative *ex vivo* confocal microscopy of $GB^{Starter}$ cells (white) and $connected^{TUM}$ neurons (CVS-N2c$^{\Delta G}$-eGFP(EnvA), green) in PDX models S24 (left) and P3XX (middle). Comparison of input-to-starter ratios of the two models in $n = 3$ mice each (right).
(D) Comparison of distance between $connected^{TUM}$ neurons to $GB^{Starter}$ cells in three patient-derived models in co-culture ($n = 30,219$ [S24], $n = 17,726$ [P3XX], $n = 10,877$ [BG7] cells in 3 biological replicates, one-way ANOVA).
(E) Distance of $connected^{TUM}$ neurons to main tumor site in three PDX models *in vivo* ($n = 17,726$ [P3XX], 30,219 [S24], and 10,877 [BG7] cells, one-way ANOVA).
(F) Representative images of $GB^{Starter}$ cell (arrows) with no adjacent $connected^{TUM}$ neurons and $GB^{Starter}$ cell with $connected^{TUM}$ neurons (asterisks). Distribution of percentage of $GB^{Starter}$ cells with adjacent $connected^{TUM}$ neurons compared with $GB^{Starter}$ cells without adjacent $connected^{TUM}$ neurons, split by patient-derived model ($n = 26$ [U3017], 175 [S24], 177 [E2], 37 [T269], and 20 [U3048] cells).
(G) Exemplary MRI images from patients classified as high neural compared with low neural.
(H) Venn diagram illustrating the overlap of CpG sites ($n = 37$) between the neural score[61] and the invasivity score (total CpG sites $n = 8,383$).
(I) Comparative analysis of the mean methylation levels associated with invasivity score between the low-neural and high-neural groups indicates a significantly lower mean methylation in the high-neural group ($p = 7.8e{-}7$, $n = 363$).
(J) Volcano plot highlighting differentially methylated CpG sites related to genes within the invasivity score in high-neural glioblastomas.
(K) Correlation analysis of the invasivity score and the neural score from The Cancer Genome Atlas Program (TCGA) multi-omic bulk data.[131]
(L) Cox proportional hazards regression model illustrating the association between survival and increasing mean methylation scores of the invasivity score in all glioblastoma (left, $n = 363$) and in high-neural glioblastomas (right, $n = 150$).
(M) Forest plots illustrating multivariate survival analysis of glioblastoma patients from the whole cohort. Hazard ratios are shown by closed circles and whiskers representing the 95% confidence interval.
(N) Synaptogenic score in rim compared with core GB regions in the Yu dataset[66] ($n = 2,795$ cells, Mann-Whitney test).

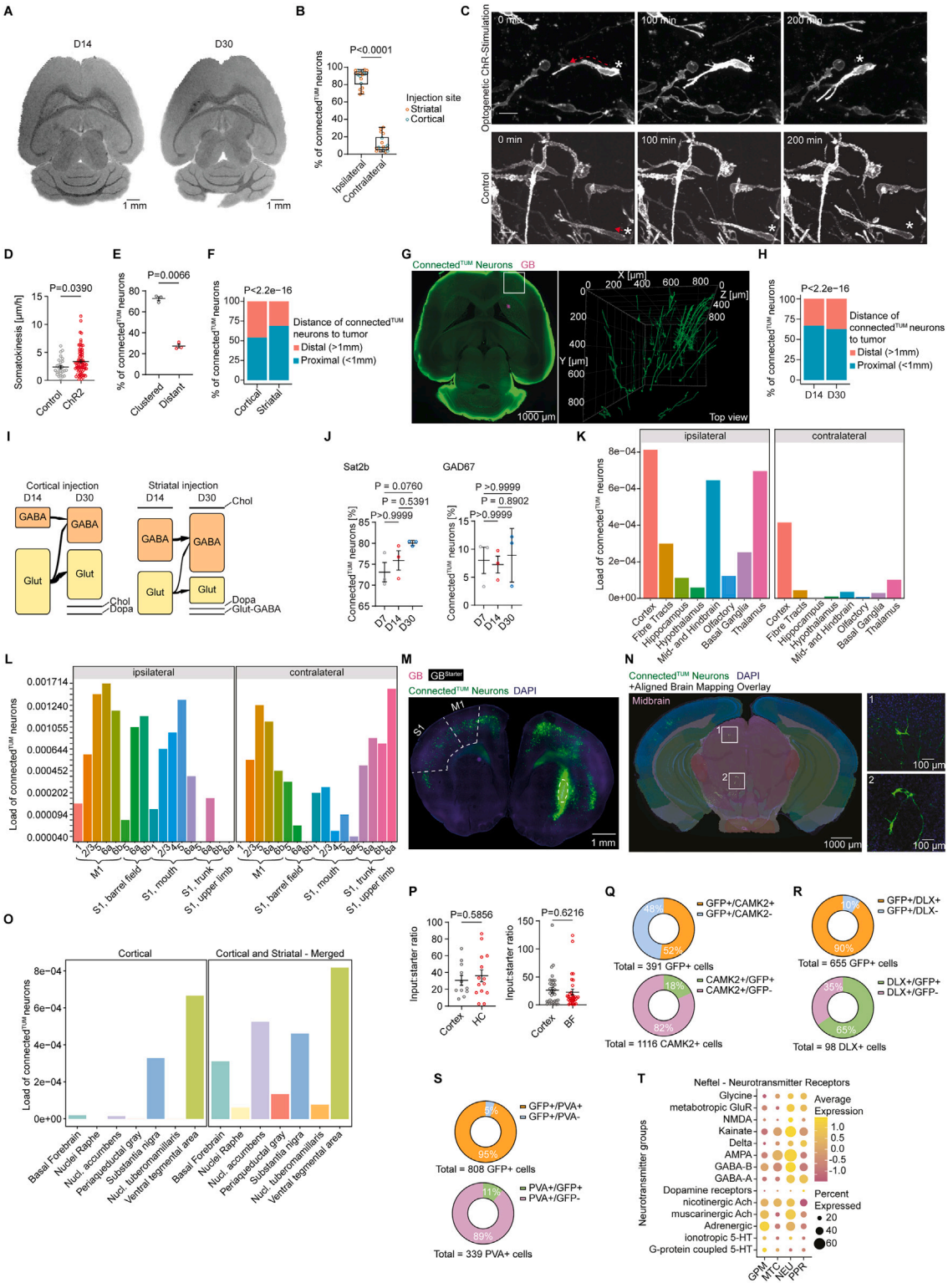

Figure S6. Brain atlas mapping of connected^{TUM} neurons, related to Figure 5

(A) MRI imaging of early-stage tumors (days 14 and 30) showing no T2-signal (PDX model BG5).

(B) Comparison of the portion of connected^{TUM} neurons in the ipsilateral and contralateral hemispheres in relation to the tumor site in cortical and striatal tumors (n = 7 cortical and 11 striatal tumors from three PDX models [S24, BG5, and P3XX], Mann-Whitney test).

(legend continued on next page)

(C) Exemplary images of GB cell dynamics *in vivo* following optogenetic stimulation (top) compared with control conditions (bottom). Scale bar: 20 μm.
(D) Comparison of somatokinesis in GB cells after optogenetic stimulation of channelrhodopsin-expressing neurons versus control (n = 76 invasive GB cells after channelrhodopsin stimulation versus 27 invasive GB cells under control conditions in n = 5 versus 3 mice in the PDX model S24, Mann-Whitney test).
(E) Proportion of connected^{TUM} neurons in clusters compared with distant connected^{TUM} neurons in co-culture (n = 3 samples from patient-derived models S24 and BG7). Clusters were determined with DBScan[145] clustering.
(F) Comparison of the portion of proximal- and distal-connected^{TUM} neurons in cortical compared with striatal tumors (n = 8,839 connected^{TUM} neurons in 7 cortical tumors, n = 30,528 connected^{TUM} neurons in 11 striatal tumors in 3 PDX models [S24, BG5, and P3XX], Wilcoxon test).
(G) Light-sheet microscopy of retrograde tracing of an early-stage glioblastoma (PDX model BG5, day 30 post-tumor injection). Single-plane image showing tumor (magenta) and connected^{TUM} neurons (CVS-N2c$^{\Delta G}$-eGFP(EnvA), green, left) from a representative mouse. 3D rendering showing zoom-in onto the connected^{TUM} neurons in the marked region on the left (n = 4 BG5 PDX mice).
(H) Comparison of the portion of proximal- and distal-connected^{TUM} neurons 14 versus 30 days after tumor implantation (n = 26,419 connected^{TUM} neurons in 11 day 14 tumors, n = 12,948 connected^{TUM} neurons in 7 day 30 tumors in 3 PDX models [S24, BG5, and P3XX], Wilcoxon test).
(I) Transition plots showing change in proportions of mapped neurotransmitters between days 14 and 30 following cortical and striatal injections.
(J) Percentage of connected^{TUM} neurons that are glutamatergic (Satb2-positive, left) and GABAergic (GAD67-positive, right) in the S24 PDX model at each investigated time point (n = 3 mice for each time point, Kruskal-Wallis test for both).
(K) Bar plot showing the load of connected^{TUM} neurons in various brain regions on the ipsilateral tumor-injected hemisphere compared with the contralateral hemisphere, analyzed in multiple sections of one representative mouse brain.
(L) Bar plot comparing the load of connected^{TUM} neurons in sublayers of the primary motor and primary somatosensory cortex on the ipsilateral tumor-injected hemisphere compared with the contralateral hemisphere as analyzed in multiple sections of one representative mouse brain.
(M) Representative fluorescence image of a PDX mouse brain slice showing ipsilateral and contralateral connected^{TUM} neurons. Dashed circle marks the main tumor site. Contralateral primary somatosensory and motor cortices are indicated with white dashed lines.
(N) Overlay of fluorescence microscopy and brain atlas mapping around the midbrain region (PDX model S24, left). Zoom-in on connected^{TUM} neurons in the brainstem (SAD-B19$^{\Delta G}$-eGFP(EnvA), right).
(O) Bar plot showing the load of connected^{TUM} neurons in various neuromodulatory circuits in cortical tumors (left) and in all analyzed samples (right) (n = 8,839 connected^{TUM} neurons in 7 cortical tumors, n = 39,367 connected^{TUM} neurons in 18 mice total from 3 PDX models [S24, BG5, and P3XX]).
(P) Input-to-starter ratio in hippocampal (HC, left) compared with cortical co-culture model (n = 11 samples for cortical, n = 14 samples for HC co-cultures, unpaired t test) and BF (right) compared with cortical co-culture (n = 36 samples for cortical, n = 31 samples for BF co-cultures, Mann-Whitney test) in patient-derived model S24.
(Q) Analysis illustrating the portion of CAMK2-positive connected^{TUM} neurons compared with all connected^{TUM} neurons (top, n = 391 connected^{TUM} neurons in 3 biological replicates). Analysis showing the portion of connected^{TUM} neurons compared with all CAMK2-positive neurons (bottom, n = 1,116 CAMK2-positive cells in 3 biological replicates).
(R) Analysis illustrating the portion of DLX-positive connected^{TUM} neurons compared with all connected^{TUM} neurons (top, n = 655 connected^{TUM} neurons in n = 6 samples). Analysis showing the portion of connected^{TUM} neurons compared with all DLX-positive neurons (bottom, n = 98 DLX-positive cells in n = 6 samples).
(S) Analysis illustrating the portion of parvalbumin-positive connected^{TUM} neurons compared with all connected^{TUM} neurons (top, n = 808 connected^{TUM} neurons in n = 4 biological replicates). Analysis showing the portion of connected^{TUM} neurons compared with all parvalbumin-positive neurons (bottom, n = 339 parvalbumin-positive cells in n = 4 biological replicates).
(T) Dot plot showing the gene expression module scores of various neurotransmitter receptor groups of different glioblastoma pathway-based cell states in the Neftel dataset[5] (n = 7,929 cells).

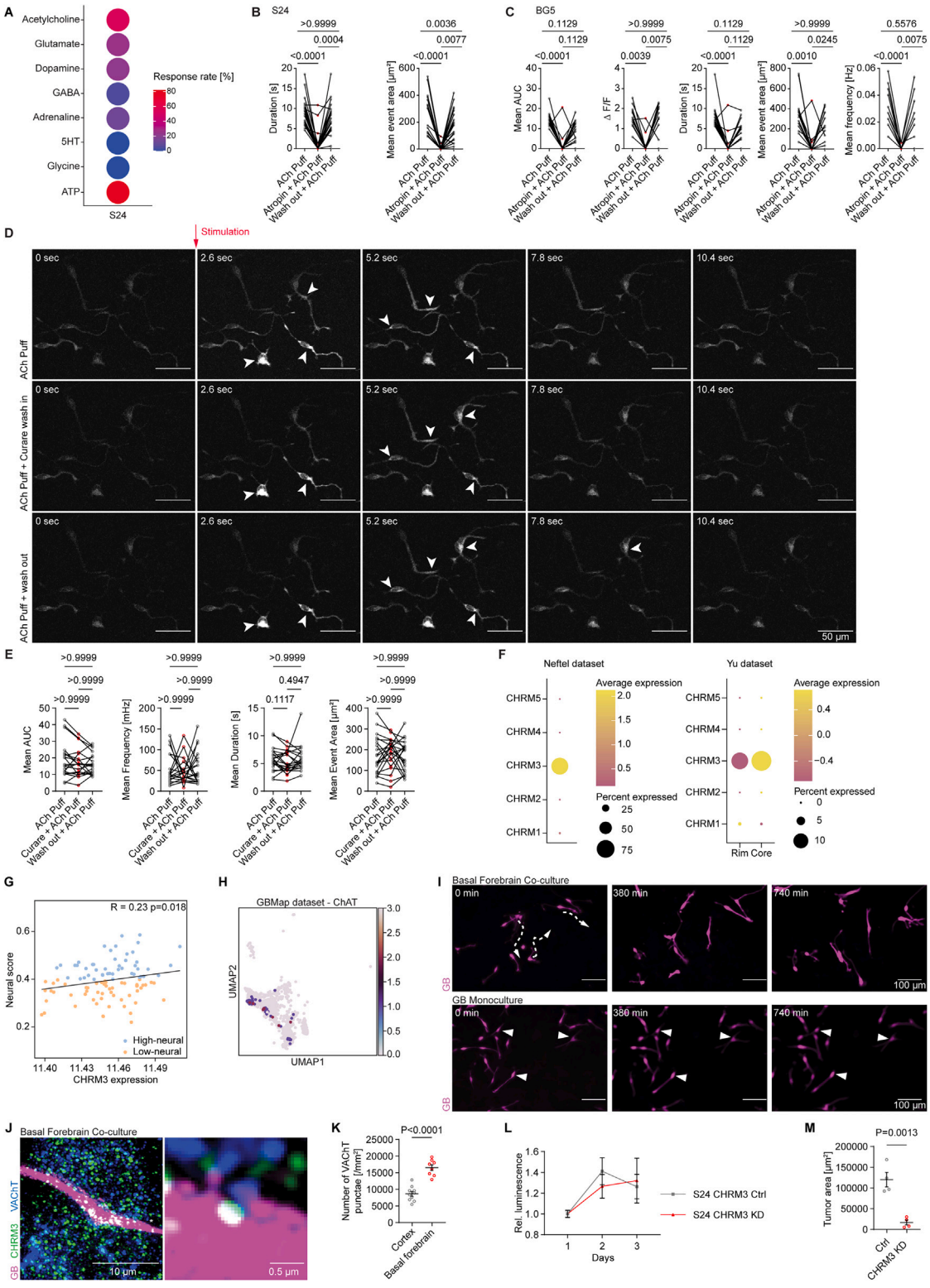

Figure S7. Relevance of muscarinic acetylcholine receptors in GB and functional role of CHRM3, related to Figure 6

(A) Dot plot indicating the calcium transient response rate to stimulation with different neurotransmitters in patient-derived model S24 (n = 56 cells).

(B) Duration (left) and mean event area (right) of calcium transients in response to acetylcholine puffing, inhibition of transients by atropine, and wash-out in S24 GB cells (n = 22 cells, Friedman test).

(legend continued on next page)

(C) Mean area under the curve, ΔF over F, duration, event area und frequency (from left to right) of calcium transients in BG5 GB cells responding to acetylcholine puffing, inhibition of transients by atropine, and wash-out (n = 14 cells, Friedman test).
(D) Time-lapse images of raw acetylcholine puff stimulation recordings (top), after curare (25 nM wash-in (middle), and after wash-out (bottom) of S24 GB cells illustrated by GCaMP7b[93] signal. Arrowheads indicate calcium transients; arrow marks time point of puff.
(E) Quantification of mean area under the curve, event frequency, duration, and event area of acetylcholine stimulation versus curare (25 nM) wash-in compared with wash-out (n = 21 cells, Friedman test).
(F) Dot plot showing the expression of muscarinic acetylcholine receptors in GB cells in the Neftel dataset[5] (n = 7,929 cells, left). Dot plot showing the gene expression of muscarinic acetylcholine receptor subunits in GB cells split by rim versus core in Yu dataset[66] (n = 2,795 cells, right).
(G) Correlation analysis of the CHRM3 gene expression and the neural score from TCGA multi-omic bulk data.[131]
(H) UMAP of the neuronal cell subpopulation in the GBMap dataset[62] showing choline acetyltransferase (ChAT) expression (n = 6,309 neurons).
(I) *In vitro* live-cell time-lapse images of GB cells in a co-culture of tumor cells and basal forebrain neurons (top) compared with a monoculture of only GB cells (bottom). Arrows with dashed lines indicating movement of invasive cells, arrows pointing to stable cells. Post processed with denoise.ai.
(J) Representative Airyscan imaging of a putative cholinergic NGS between a cholinergic neuron in a basal forebrain culture and a S24 GB cell.
(K) Number of VAChT punctae normalized to area in cortical versus basal forebrain neuronal co-cultures (n = 10 fields of view for cortical and 8 fields of view for basal forebrain co-culture, unpaired t test).
(L) CellTiter-Glo assay of S24 scramble control (gray, n = 23 replicates) and S24 CHRM3 knockdown (red, n = 23 replicates) models.
(M) Quantification of cortical tumor areas in the ipsilateral retrosplenial cortex in control compared with CHRM3 knockdown mice (n = 4 mice each, unpaired t test).

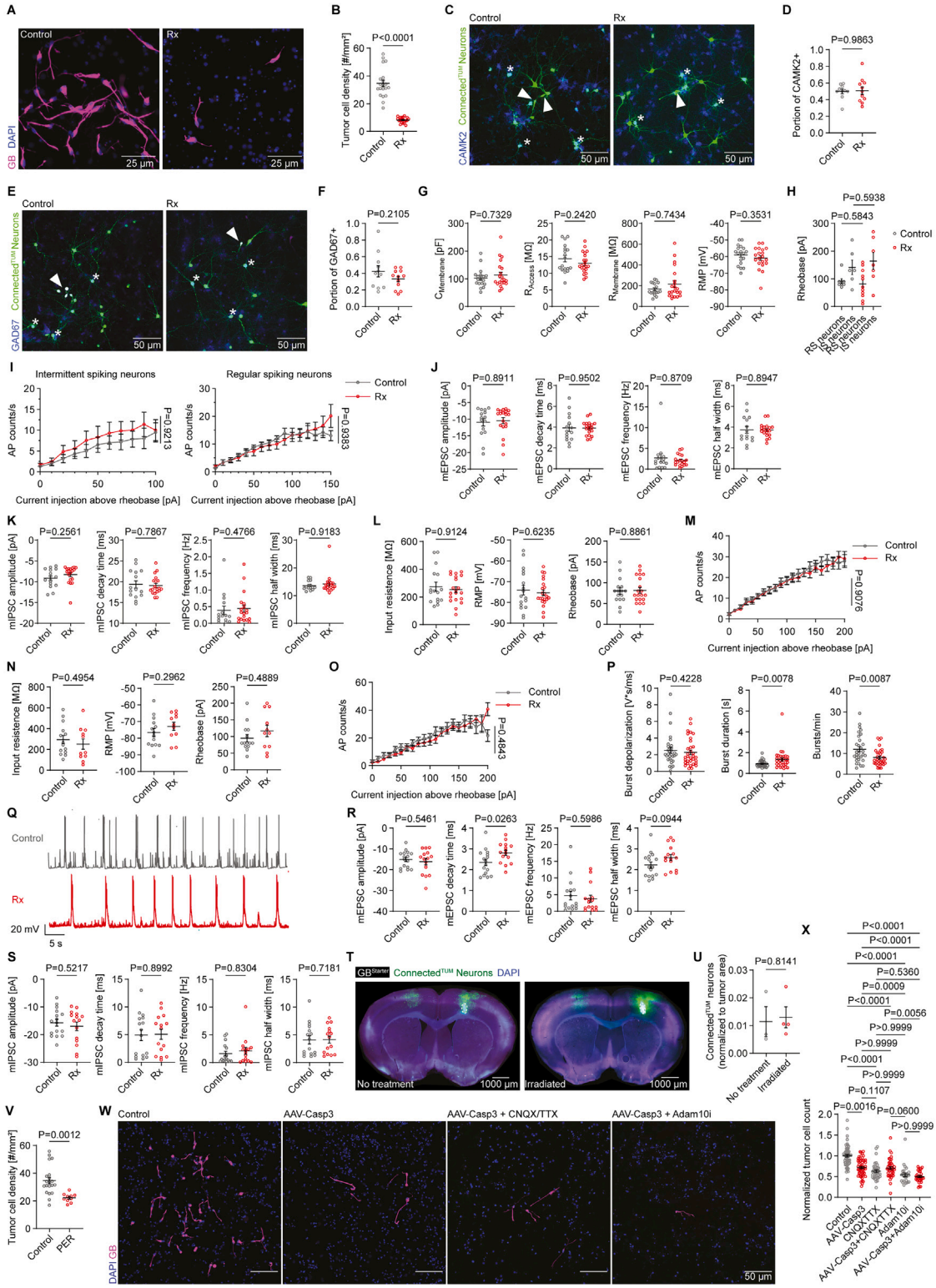

Figure S8. Radiotherapy-induced effects on glioblastoma cells and connected^{TUM} neurons, related to Figure 7

(A) Representative images of tumor regions in control (left) compared with radiotherapy-treated (right) conditions.

(B) Tumor cell density in cell count per mm^2 under control conditions versus after irradiation (n = 20 control versus 20 irradiated samples, unpaired t test)

(legend continued on next page)

(C) Exemplary images of CAMK2-positive connected^{TUM} neurons in control versus irradiated samples. Asterisks indicate marker-positive connected^{TUM} neurons, arrowheads point to GB^{Starter} cells.
(D) Quantification of the portion of glutamatergic (CAMK2-positive) neurons of all connected^{TUM} neurons (n = 10 control and 11 irradiated samples, Mann-Whitney test).
(E) Representative images of GABAergic (GAD67)-positive irradiated versus control samples. Asterisks indicate marker-positive connected^{TUM} neurons, arrowheads point to GB^{Starter} cells.
(F) Quantification of the portion of GABAergic neurons of all connected^{TUM} neurons (n = 11 control and 12 irradiated samples, unpaired t test).
(G) Passive membrane properties of connected^{TUM} cortical neurons under control condition and after radiotherapy: membrane capacitance ($C_{Membrane}$), access resistance (R_{Access}), membrane resistance ($R_{Membrane}$), and RMP (n = 18 control and 20 neurons after radiotherapy, Mann-Whitney test for $C_{Membrane}$ and $R_{Membrane}$, unpaired t test for RMP and R_{Access}).
(H) Neuronal rheobase of connected^{TUM} cortical neurons under control condition and after radiotherapy split by neuronal firing type (n = 8 regular-spiking control neurons, n = 11 regular-spiking neurons after radiotherapy, Mann-Whitney test, n = 6 intermittent-spiking control neurons, n = 7 intermittent-spiking neurons after radiotherapy, unpaired t test).
(I) Input-output relationship between the current injected relative to the rheobase current and the number of action potentials generated over 1 s in connected^{TUM} intermittent-spiking (left, n = 4 control, 9 irradiated cells) and regular-spiking neurons (n = 8 control, 11 irradiated cells) under control condition versus after irradiation, quantified by the area under the curve (STAR Methods).
(J) Postsynaptic mEPSC properties of connected^{TUM} neurons under control conditions and after radiotherapy (n = 15 control and 19 neurons after irradiation, Mann-Whitney test for mEPSC amplitude and frequency; unpaired t test for mEPSC half width and decay time).
(K) Postsynaptic mIPSC properties of connected^{TUM} neurons under control conditions and after radiotherapy (n = 15 control and 19 neurons after irradiation, Mann-Whitney test for mIPSC amplitude, frequency, and half width; unpaired t test for mIPSC decay time).
(L) Quantification of input resistance (Mann-Whitney test), resting membrane potential (unpaired t test), and neuronal rheobase (unpaired t test) in regular-spiking control and irradiated neuronal monocultures (n = 16 regular-spiking control neurons, n = 20 regular-spiking neurons after radiotherapy).
(M) Induced action potential frequency in dependence of the neuronal rheobase in regular-spiking control and neurons after radiotherapy quantified by the area under the curve (STAR Methods) (n = 16 regular-spiking control neurons, n = 20 regular-spiking neurons after radiotherapy, unpaired t test).
(N) Quantification of input resistance (unpaired t test), resting membrane potential (unpaired t test) and neuronal rheobase (Mann-Whitney test) in intermittent-spiking control and irradiated neuronal monocultures (n = 14 intermittent-spiking control neurons, n = 11 intermittent-spiking neurons after radiotherapy).
(O) Induced action potential frequency in dependence of the neuronal rheobase in intermittent-spiking control and irradiated neurons quantified by the area under the curve (STAR Methods) (n = 14 intermittent-spiking control neurons, n = 11 intermittent-spiking neurons after radiotherapy, unpaired t test).
(P) Quantification of normalized burst depolarization envelope, burst duration, and burst frequency in neuronal monocultures (n = 31 control neurons, n = 33 neurons after radiotherapy, Mann-Whitney test).
(Q) Representative recording of spontaneous excitatory postsynaptic potential (EPSP) bursting activity in rat neuronal monocultures under control conditions (top) and after radiotherapy treatment (bottom).
(R) Quantification of mEPSC properties: amplitude (unpaired t test), decay time (unpaired t test), frequency (Mann-Whitney test), and half width (unpaired t test) in neuronal monocultures (n = 16 control, n = 15 irradiated neurons).
(S) Quantification of mIPSC properties: amplitude (unpaired t test), decay time (Mann-Whitney test), frequency (Mann-Whitney test), half width (Mann-Whitney test) in neuronal monocultures (n = 16 control, n = 15 irradiated neurons).
(T) Representative images of untreated mice compared with irradiated mice prior to tumor injection. Dashed white circles indicate the tumor localization.
(U) Quantification of connected^{TUM} neurons normalized to tumor area in untreated versus irradiated mice (n = 3 mice for untreated and 4 mice for irradiated conditions, unpaired t test).
(V) Tumor cell density in cell count per mm^2 under control conditions compared with after perampanel treatment (n = 20 control versus 10 perampanel-treated samples, unpaired t test).
(W) Exemplary images of S24 GB cells in control conditions (left), with Cre-inducible caspase 3 AAV virus (second to left), with Cre-inducible caspase 3 AAV virus in combination with CNQX (20 μM) and TTX (1 μM) (second to right), and with Cre-inducible caspase 3 AAV virus in combination with Adam10 inhibition (2 μM).
(X) Quantification of S24 GB cell counts in combination of caspase 3 AAV and different drugs (n = 56 (Ctrl), 54 (AAV-Casp3), 35 (CNQX/TTX), 38 (AAV-Casp3+CNQX/TTX), 25 (Adam10i), 29 (AAV-Casp3+Adam10i, Kruskal-Wallis test).